Master Thesis in Geosciences

Chemical Characteristics of Deep Groundwater in the Gardermoen Aquifer

Controlling processes and residence times.

Anja Sundal

UNIVERSITY OF OSLO

FACULTY OF MATHEMATICS AND NATURAL SCIENCES

Chemical Characteristics of Deep Groundwater in the Gardermoen Aquifer

Controlling processes and residence times.

Anja Sundal

Master Thesis in Geosciences

Discipline: Environmental Geology and Geohazards

Department of Geosciences

Faculty of Mathematics and Natural Sciences

UNIVERSITY OF OSLO

July 2006

Advisers: Professor Per Aagaard (UiO) and Bente Wejden (OSL)

This work is published digitally through DUO – Digitale Utgivelser ved UiO

http://www.duo.uio.no

It is also catalogued in BIBSYS (http://www.bibsys.no/english)

Cover Photo: OSL

Acknowledgements

First and most of all I would like to thank my supervisor, Professor *Per Aagaard*, for his guidance. Like so many students before me I admire his enormous stock of knowledge, and I am grateful for his positive spirit and confidence in this project. *Bente Wejden* has served as my co-supervisor and "insider" at OSL. I am deeply thankful for all her help and support.

I have gotten to know so many interesting people at the Department of Geosciences who keep their office doors open and are eager to help. I truly appreciate all the time spent by *Dag Karlsen* and *Christian Backer Owe* in the last few weeks, providing me with speed courses in organic geochemistry and lab work. I have really learned a lot, thank you both. A special thanks to *Gijs Breedveld* for discussions on the organic part, and for being such an inspiring lecturer in hydrogeology courses. Furthermore, I greatly appreciate the cooperation with *Matthias Brennwald* at Eawag, and although we did not manage to finish the isotope analyses before the submittal of this thesis, I look forward to the continuation of the project.

Many thanks to *Mufak Naoroz* for good laughs and words of lab-wisdom while helping me out with the chemical analyses. *Berit Løken Berg* and *Turid Winje* have both made life in the chemistry lab easier by supplying me with advice and equipment. Thanks! The librarians *Marit Sørlie* and Kristin *Rangnes* can and will find everything you look for. Thanks!

I would like to thank *Per Færøvig* at the Department of Biology for letting me use his limnology lab whenever I wanted. Thanks also to *Jarl Øvstedal* and the *OSL technicians* for cooperation and for providing access to wells and equipment.

I was lucky to have a strong and humorous field assistant, while dragging equipment through the snow on freezing days. Thank you, *Michael*! I also thank *Temesgen*, for the times he stepped in. Many thanks to my *fellow student friends*, and all my other *great friends*, for all the fun we have had during the last few years of student life! Special thanks to Raymond for help and support. Finally I'd like to thank my family for taking such interest in what I do, and especially *dad* for reviewing the manuscript.

Anja Sundal, July 2006

Table of Contents

1. Introduction

The field of study is situated in Northern Romerike, at Gardermoen. In this area extensive hydrogeological research has been performed, both during the International Hydrogeological Decade from 1965 – 1974 and later within the Gardermoen project; "Faneprosjekt Gardermoen", from 1992 – 1995. The building of, and operations on, the Gardermoen International Airport has also generated further knowledge on the aquifer system. There is, however, limited knowledge on deeper parts of the groundwater reservoir at Gardermoen.

1.1 Objectives

This thesis is part of a Norsk Forskningsråd (NFR) project for dating and characterising deep groundwater at Gardermoen. Some of the work has been carried out in cooperation with Oslo Lufthavn AS (OSL), providing access to wells within the airport area and a 3D groundwater flow model.

The project aim is to analyse groundwater samples in order to determine if there are regional and/or depth-related chemical differences in the groundwater chemistry. Deep groundwaters are normally characterized by long residence times in the aquifer and by being well evolved geochemically. A groundwater sample carries with it information about the accumulative results of all processes affecting waters from the point of infiltration to its present state. Estimated average groundwater residence time at Gardermoen is in the range of 20-30 years. Thus, one may assume that these groundwaters also constitute an archive of groundwater quality before present anthropogenic input caused by airport activity in the area.

The characterisation will be based mainly on a set of new groundwater samples collected and analysed for major and minor components during winter and spring 2006. The results of the chemical analyses shall be related to the main geochemical processes influencing the groundwater chemistry in the Gardermoen aquifer, and compared to previous work, with emphasis on the studies performed by Jørgensen *et al.* (1991). Further, inverse geochemical modelling with PHREEQC will be used as a tool for quantifying the natural contribution to groundwater chemistry from the main weathering processes.

The general distribution of the organic fraction in the groundwater at Gardermoen, has not previously been studied. In this study it will be tested to what extent extracted organic

material from groundwater samples may be analysed by means of the instruments available at the department of geoscience; TLC-FID, GC-FID and GC-MS. Further, it will be looked into whether there are traces to be found of any known or unknown anthropogenic input.

Dating of deep groundwater is a useful tool for determining groundwater turnover times and flow dynamics. Within this master thesis only part of the NFR project for dating deep groundwater by means of the ^{3}H-^{3}He method will be carried out, collecting samples and sending them for analysis, as the time frame is too short to conclude the project. The final work on this subject will be carried out after the submittal of this thesis. An existing set of dated water samples from Gardermoen, from which results has not been published will be presented here along with the preliminary results generated in this study. The previously calculated water ages will be compared to the simulations of residence times in a 3D groundwater flow model which is currently in development at OSL.

2. Study Area

2.1 Geographic Location

The studied area is located in the south-eastern part of Norway, at Gardermoen in the Romerike region, within the municipalities of Ullensaker and Nannestad (figure 2.1, appendices A1 and A2). Norway's largest self-feeding groundwater reservoir is situated here. It is also the location of the Gardermoen international airport.

2.1.1 Sampled Wells

The data material presented in this thesis is mainly based on new water samples from 18 different well points, some of which are multilevel. All together 29 well screens were sampled. The samples were collected within the time interval of December 2005 to May 2006. The wells are distributed within and around the airport area (figure 2.1) in quaternary deltaic deposits. An equivalent of the map below (figure 2.1) including well names and a table of well data such as coordinates, depth and height above sea level, are given in appendices A1 and B1, respectively. A detailed map of wells situated at Trandum is given in appendix A3.

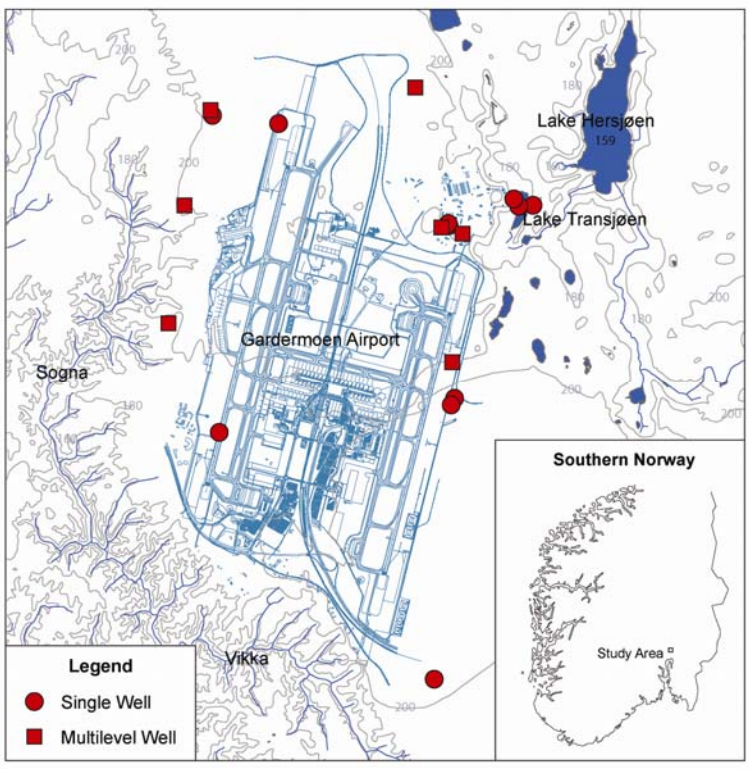

Figure 2.1: Distribution of sampled wells within the study area, at Gardermoen.

2.2 Geological Setting

Glacifluvial material deposited during the melting period following Scandinavias last ice age makes up important aquifers (Jørgensen & Østmo, 1990). In the Romerike region, which extends approximately 50 km north-south, five Holocene ice-contact deltas have been deposited directly on top of Precambrian basement (Tuttle & Aagaard, 1996). Mesozoic and Cenozoic (up until Quaternary) sequences are missing in this region.

2.2.1 Bedrock Geology

The Romerike bedrock is part of the Eastern Norwegian Precambrian basement, bordering in the west towards the Permian eruptives of the Oslo area (Oftedahl, 1981). It contains more than 95% gneisses with additional granites and pegmatites. The most characteristic gneissic rock in the studied area is the grey Romerike gneiss that was formed during a period of metamorphosis 1650-1600 m.y.a. (Oftedahl, 1981). It may be subdivided into a biotite-enriched tonalitic gneiss and a hornblende-enriched tonalitic gneiss (Gvein *et al*., 1973).

2.2.2 Quaternary Geologic Development

The Quaternary time period may be divided into a period of glaciations: Pleistocene, and subsequently a post glacial period, Holocene (0 – 10 000 BP). Following the interglacial chrono-zone Eem (75 000 – 100 000 BP), recognised by deposits in western Norway, the Weichselian glaciation lasted up until 10 000 BP. It may be subdivided into Weichselian I and Weichselian II, as there was a milder interstitial period in between. Denominated ‘the last ice age’, Weichselian II reached its maximum at around 20 000 BP (Oftedahl, 1981). During the following period of melting the climate displayed large fluctuations despite the general trend of warming. In warmer periods the ice front was quickly retreating, while in colder periods the ice front was at a standstill or slowly advancing. Successive stages of the retreating ice are recognised by the characteristic marginal deposits left, such as on-shore end moraines or coarse grained delta deposits. Mapping and dating of glacial deposits form the basis for constructing maps of the extent of paleo-ice-sheets.

The most marked Norwegian terminal deposit; the Ra-stage (11 000 – 10 650 BP) (Sørensen, 1979), defines the transition from Pleistocene to Holocene. It also marks the onset of more rapid ice retreat, which may be traced northwards through successive end-moraine deposits (*e.g.* Ås, Ski and Aker). During the Preboreal chrono-zone (10 000 – 9000 BP) the glacial retreat was in the order of 120-150 m/year (Oftedahl, 1981). Within this period The Romerike Substages (figure 2.2), five ice-contact deltas including the Gardermoen Delta Complex, were deposited during short breaks in the ice-retreat, within a time interval of 400 years (9800 - 9400 BP) (Holtedahl, 1924, 1974; Sørensen, 1979). The Gardermoen Delta Complex is described more thoroughly in section 2.2.3.

The retreat of the Scandinavian ice cap caused regional isostatic uplift due to the release of downward pressure induced by overlying masses if ice. The effect was greatest in the central and thickest part of the ice sheet. With the land rising, there was an overall regression (Holtedahl, 1924). By mapping the migrating marine limit, using characteristic shoreline deposits, the uplift relative to present conditions may be quantified. There are, however, a number of factors complicating the calculations of the total uplift from maximum load and subsequently the uplift rates. These difficulties are connected to the eustatic sea level rise caused by the addition of melt water, and that different parts of Norway became ice free at different times, causing a skewed rising of the land (Oftedahl, 1981).

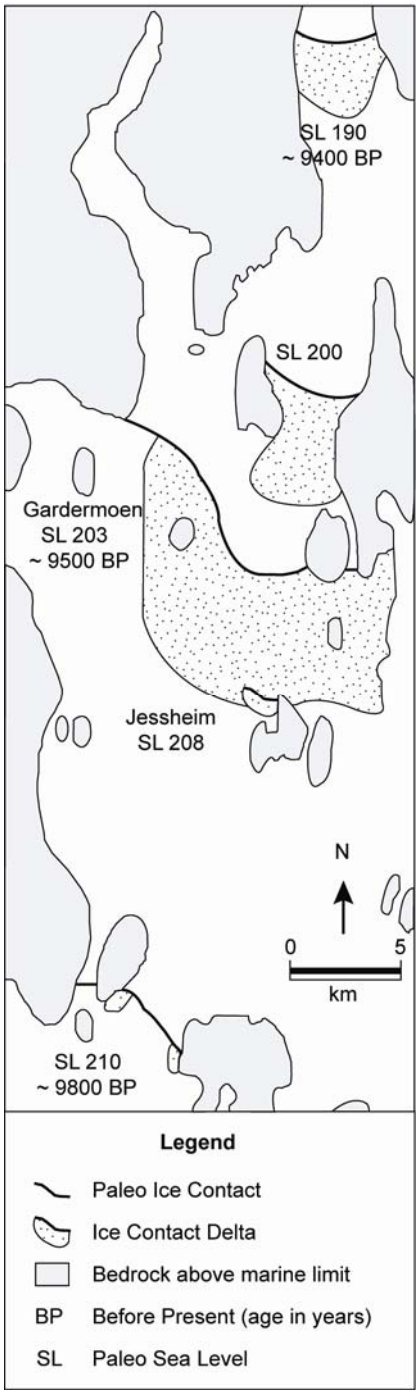

Figure 2.2: The location of the Romerike Substages during the Preboreal chronozone (modified from Longva & Thoresen, 1989).

2.3 The Gardermoen Delta Complex

The Gardermoen Delta, previously known as the Hauerseter Delta (Holtedahl, 1924), is a complex of two sub-deltas; the Trandum Delta and the Li Delta, the latter being the largest. The entire complex has a total surface area of 79 km^2; the Li Delta comprises 58 km^2 out of this (Østmo, 1975b). It was deposited in early Holocene, 9500 years BP, as determined by ^{14}C dating and pollen analysis (Sørensen, 1979; 1983; Longva & Thoresen, 1989), during a quite short time interval; probably in the course of 70 years (Tuttle, 1990).

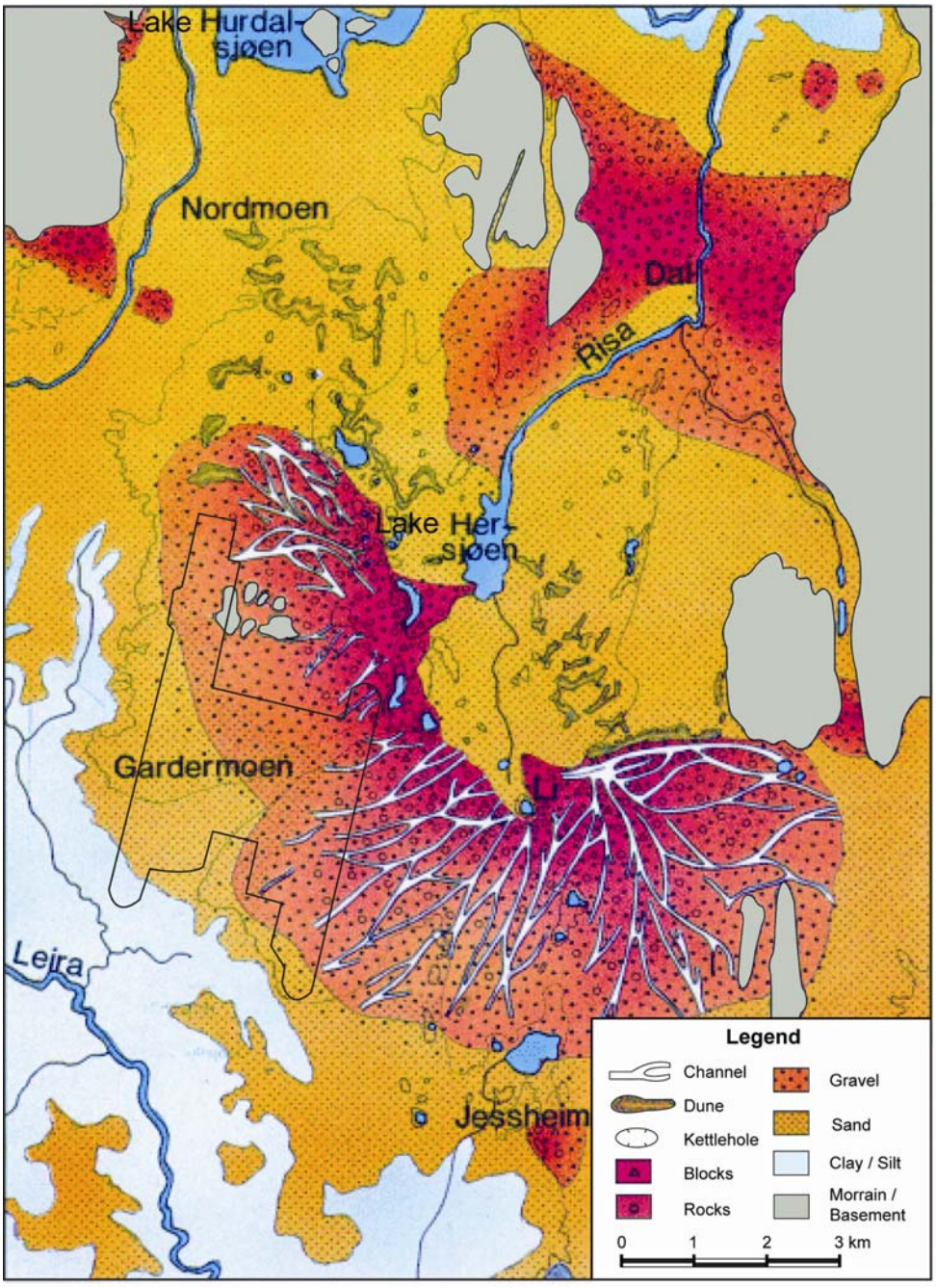

Figure 2.3: Map of Pleistocene deposits at Northern Romerike. The Gardermoen Airport is inserted (modified from Jørgensen & Østmo, 1990).

The delta complex developed in a marine, mud-dominated fjordal basin; the Romerike fjord (Tuttle & Aagaard, 1996), at depths in the range of 60 to 150 m (Tuttle, 1990). The coarse sand and gravel deposits, transported by highly energetic glacial rivers, were deposited in front of the glacier at sea level, which at that time was 203 meters higher than present (Tuttle, 1997). The distribution of these deposits is displayed in figure 2.3. During the deposition there was a net shoreline drop of 7m caused by marine regression (Sørensen, 1982; Tuttle, 1997). In the Oslo area the regression (c.f. section 2.2.2) was occurring at rates of around 10 m per 100 years (Hafsten, 1979; Sørensen, 1979, 1983), with the glacial isostatic uplift counteracting and exceeding the global eustatic rise at the time.

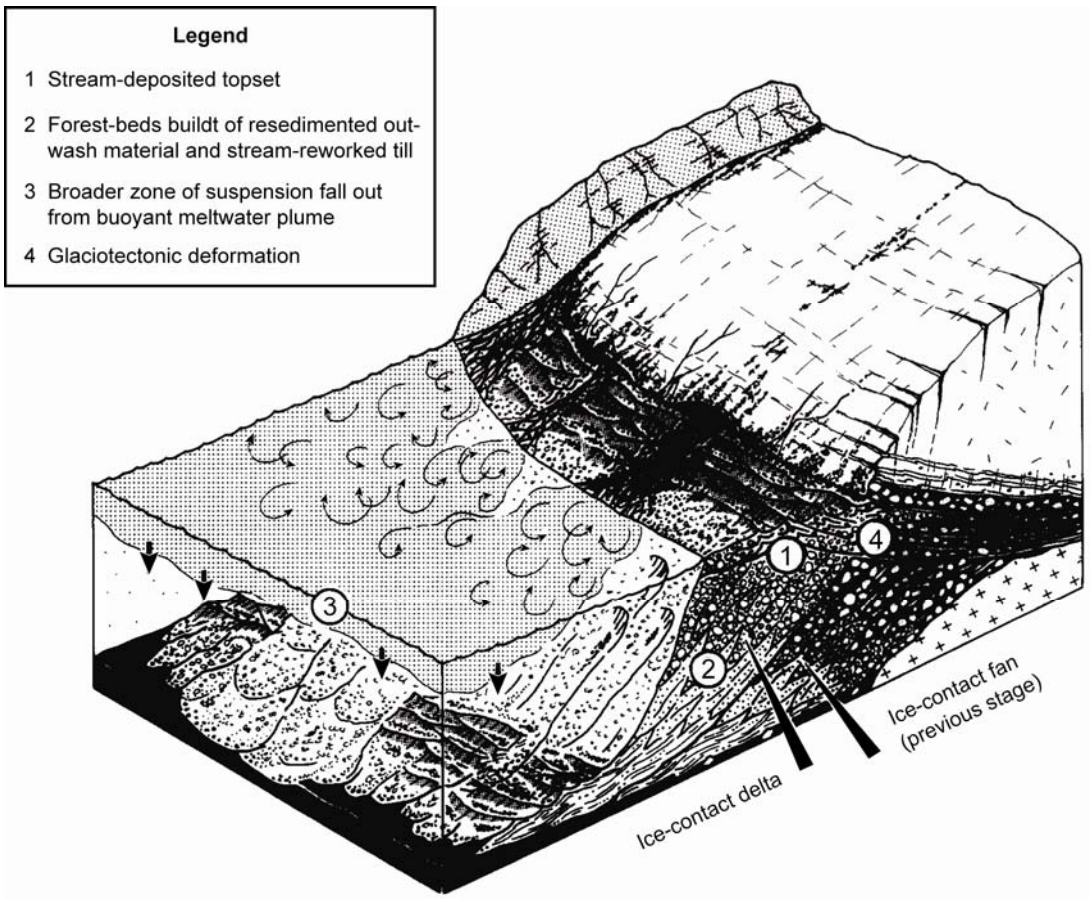

Figure 2.4 : Depositional characteristics of an ice-contact delta (modified from Lønne, 1995).

As opposed to the ice contact submarine fans deposited south of the Romerike substages, the Gardermoen Delta Complex evolved further into an ice contact delta (figure 2.5). Due to increased melt water discharge and sediment supply from the retreating glacier (Østmo, 1975a; Sørensen, 1983) and the decrease in fjord-water depth, the outwash fans aggraded to

sea level before forming the prograding, coalescing delta lobes building the ice-contact delta (Tuttle, 1997).

2.3.1 Stratigraphy

The sedimentary architecture of the Gardermoen Delta complex is characterized by its tripartite delta units; topset, foreset and bottomset, and has been classified as a Gilbert type ice-contact delta-complex (Tuttle, 1997).

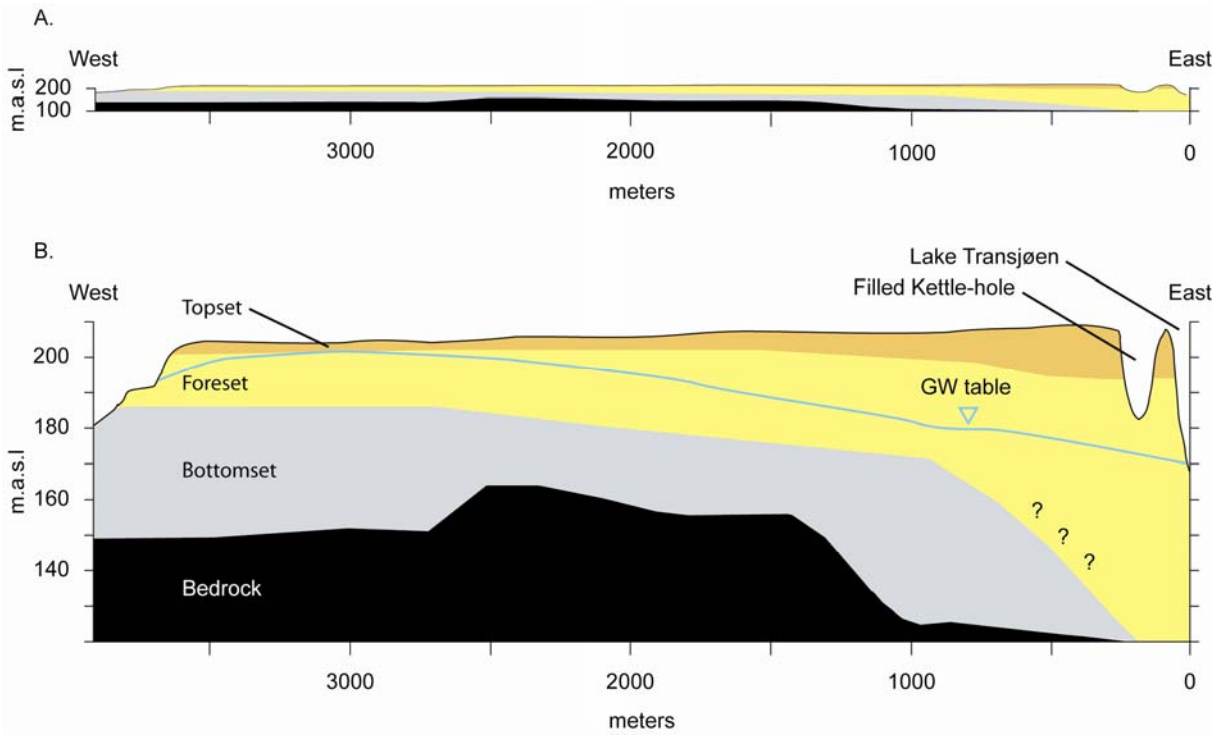

Figure 2.5: Stratigraphic models of a crossection through the Trandum Delta, extending from Lake Transjøen to the river Sogna., based on soil core samples and well logs. Consult appendix A1 for location of the cross section (profile 1). a) Cross section with actual horizontal/vertical proportions; 1 : 1. b) Cross section with vertical exaggeration; 1 : ~15 (modified from Tuttle, 1997).

In the topset unit (figure 2.5) the dominating sedimentary process was deposition of coarse gravel and sand from subaerial braided rivers (Tuttle, 1997). The layering is horizontal and the thickness of the unit decreases with distance from the melt water portals as the river energy declined. The deposits also become finer and better stratified in distal parts (Jørgensen *et al*., 1995). Paleo-meltwater discharges exceeded 3000 m^3/s (Tuttle, 1997). During flooding periods rivers eroded channels (figure 2.3) into the delta surface which all stop at 203 m.a.s.l., corresponding to the paleo sea level. The proximal part of the delta aggraded to a maximum altitude of 223 m.a.s.l. (20 m above the paleo sea level), while the delta front was situated at 203-205 m.a.s.l. (Holtedahl, 1924; Østmo, 1975a; Longva, 1987; Tuttle, 1997).

The tilted foreset beds (figure 2.5) are mainly sandy submarine deposits from river mouths and suspension fallout. There is a decrease in grain size from proximal towards distal parts of the delta, but the variation is less than in the topset unit. The geometry of the unit might be influenced locally by bedrock geometry, ice blocks left by the retreating glacier (c.f. kettle-holes) or meltwater channels (Tuttle, 1997).

The bottomset unit (figure 2.5) consists of fine grained sediments in horizontal layers from suspension fallout, with random lenses of coarser grained material from gravity-driven mass transport (Tuttle, 1997). Its geometry is, to a greater extent, influenced by the bedrock topography, compared to the foreset unit.

2.3.2 Surface Depositional Features

When the ice retreated northwards, blocks of ice were left in the terrain. These became partly or entirely covered by sediment, and when the ice melted, depressions or so called kettle-holes (figure 2.3) were formed. Some of these are now filled with water and denominated kettle-hole lakes.

Another characteristic depositional feature is the fine grained eolean sand dunes (figure 2.3) formed by catabastic winds in front of the ice, where the ground was bare with loose deposits before vegetation settled (Østmo, 1975a).

A network of eroded melt water channels (cf. section 2.3.2 and figure 2.3) radiates from the delta portals at Li and Trandum, which are indicated by subglacial eskers (Tuttle, 1997).

During the next period of ice retreat stagnation, with the ice front situated 7 km north of the Gardermoen Delta complex, an ice-dammed lake was formed in between them. In this basin glaciolacustrine sands and silts and glaciofluvial sands and gravels were deposited (Holtedahl, 1924; Østmo, 1976; Follestad & Østmo, 1977; Longva & Østmo, 1987; Longva, 1987), causing the Li Delta feeding esker to be completely covered (Tuttle, 1997). Simultaneously marine silts and clays were deposited on the Gardermoen delta front and on the distal parts of the submerged braidplain (Tuttle, 1997; Sønsterudbråten, 1994). With the rapid regression rates (c.f. section 2.2.2) the time interval with fine deposition was relatively short (Tuttle, 1997).

2.3.3 Mass Volume of Sediments

The mass volume of the delta sediments has been calculated by Tuttle (1997) using a terrain model to integrate the digitized area of the delta plain surface and the bedrock topography. The result was an estimated volume of approximately $44 \cdot 10^9$ m^3 and a sedimentation rate of circa $6.3 \cdot 10^7$ m^3/y. Tuttle (1997) suggests that maximum ablation controlled drainage may correspond to such high rates of sedimentation. The values for specific sediment yield are one order of magnitude larger than for Norwegian present day glaciers (Østrem, 1975; Bogen, 1989) and for Late Weichselian glaciers on Svalbard, where the bedrock is softer (Elverhøi *et al*., 1995). It has therefore been inferred by Tuttle (1997) that the large sediment yield was caused by adding the effects of glacial erosion, englacial and supraglacial supply and the reworking of subglacial, unconsolidated sediments.

2.3.4 Sources of Sediment

In summary, the deposits are made up of glacifluvial sand and gravel, with underlying silty marine sediments. There are two main sources of sediment in glacimarine systems such as the Gardermoen delta; unsorted subglacial basal till, and outwash material from meltwater flow (sub-, supra-, en- and pro-glacial) (Lønne, 1995; Tuttle, 1997). In the north-western part of the deposit; the Trandum Delta, the sediments are dominated by Permian rocks from the Hurdalen-area. The Li Delta, in the east, comprises predominantly sediments derived from Precambrian and Sparagmittic rocks in the Mjøsa and Gudbrandsdalen region. The two deltas were deposited from glacial rivers in front of two different ice lobes, transporting material from the northwest and northeast, respectively (Jørgensen *et al*., 1995).

2.3.5 Mineralogy

Silicate minerals are by far dominant in the deposits at Gardermoen. In table 2.1 the average weight distribution of silicates from three sediment cores in the Trandum delta at Gardermoen are displayed.

Location	Depth	Amphibole	Mica	Chlorite	K-feldspar	Plagioclase	Quartz
	m	w. %	w. %	w. %	w. %	w. %	w. %
Lake Hersjøen	1 - 50	2	15	7	18	8	50
Moreppen I	1 - 14	1	3	3	15	31	43
Moreppen II	1 - 8	1	2	6	8	18	65

Table 2.1: Weight distribution (%) among silicate minerals in sediments at different locations at Gardermoen; Lake Hersjøen (Jørgensen *et al*., 1991), Moreppen I (Skarstad, 1996) and Moreppen II (Dagestad, 1998).

Quartz is the major component in all samples. There is some variation in the mineralogy among the three localities. Jørgensen *et al*. (1991) reported that the distribution among silicate minerals was fairly uniform with depth, although the higher content of mica at Hersjøen (deepest) compared to the Moreppen localities might indicate that deep fine grained sediments increases the relative content of mica (Dagestad, 1998). Moreppen I stands out with a higher content of plagioclase. The major amphibole is hornblende (Jørgensen *et al*., 1991; Skarstad, 1996). The upper 50 cm has a slightly different composition due to leaching (Teveldal *et al*., 1990; Jørgensen *et al*., 1991).

Among additional non-silicate minerals present; calcite and pyrite are especially important in relation to groundwater chemistry. Calcite is present mainly within shale fragments and at depths greater than approximately 10m, where the calcite dissolution front is situated (Jørgensen *et al*., 1991; Basberg, 1999). The average content of calcite in deep samples at Nordmoen is 2.4 ± 0.2 weight %. The $MgCO_3$ content in these samples was 2.5 mole % (Jørgensen *et al*., 1991). Also Pyrite is found in shale fragments at Gardermoen. At Nordmoen the average pyrite content of deep samples (19 – 58 m depth) is approximately 0.5 weight %, while at Moreppen II (10 – 14 m depth) the average is 1 – 1.5 weight % (Jørgensen *et al*., 1991; Dagestad, 1998). The unsaturated and upper saturated zones are depleted of pyrite (Dagestad, 1998; Basberg, 1999). Based on figure 2.6 below it seems clear that the calcite and pyrite content is increasing with depth at both localities. Secondary minerals, present in much smaller amounts are: vermiculite, imogolite, various oxides and oxyhydroxides (Basberg, 1999).

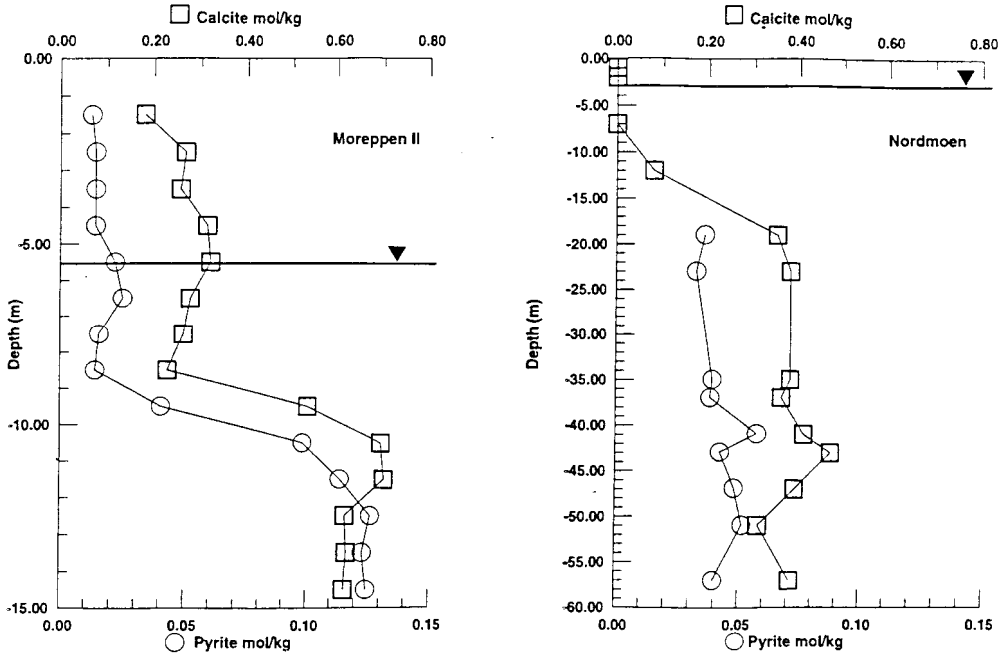

Figure 2.6: Observed sediment concentrations. Plots from Basberg (1999), data from Moreppen II after Dagestad (1998) and from Nordmoen after Jørgensen *et al*. (1991).

2.4 Hydrogeology

The Northern Romerike Aquifer covers an area of approximately 105 km^2, including the Gardermoen Delta Complex and the glaciofluvial, glaciolacustrine and silty glaciomarine sediments north of it (Tuttle, 1997). In the south and west it is bordered by marine clays, which form no-flow boundaries. The aquifer is in major parts unconfined and solely recharged by precipitation.

The groundwater table is situated at depths in the range of 0 to 30 m below the surface. The groundwater divide forms a semicirclular shape (figure 2.7). The groundwater table is convex concurrent with the delta ridge. The groundwater level varies throughout the year, in relation to the amount of precipitation, with the highest levels during the snow melting period (c.f. section 2.4.2). The maximum level does not, however, occur simultaneously over the entire area, since the extent of the unsaturated zone is varying (*i.e.* increasing in thickness away from the groundwater divide) (Østmo, 1976).

The pattern of drainage may be divided into three sections with an area of circa 18 km^2 draining to Lake Hurdalssjøen in the north, circa 32 km^2 to the river Leira in the southwest

and approximately 55 km^2 to the river Risa and Lake Hersjøen in the east (Tuttle, 1990) (figure 2.6). Of the total amount of water, around 80% drains towards the north-east into the river Risa and the lake Hersjøen (Jørgensen & Østmo, 1990), through the coarse-grained glacial-contact delta deposits. The remainder flows out through the fine-grained distal delta deposits in the south-west, where characteristic erosional features, *i.e.* ravines, have been formed. The outflow distribution determines the position of the groundwater divide, and the skewed partitioning places the divide closer to the area with least outflow; south-westwards (figure 2.7).

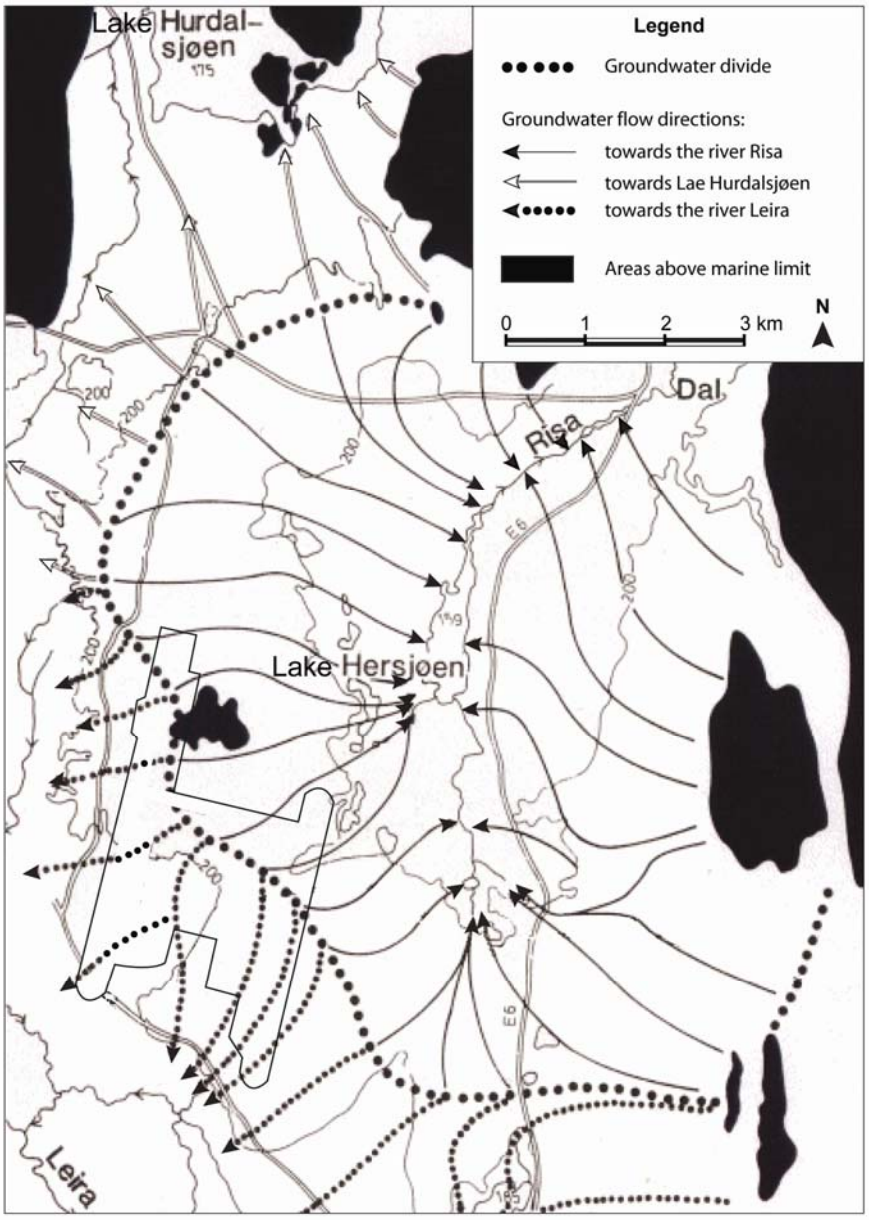

Figure 2.7: General groundwater flow pattern in the study area (map was made before building Gardermoen airport, which has been inserted here, *i.e.* section 2.4.3). Modified from Jørgensen & Østmo, 1990.

2.4.1 Hydrostratigraphy

The hydrostratigraphy of the Gardermoen Delta Complex does not fully correspond to the lithostratigraphy (*i.e.* topset, foreset, bottomset). Based on grain size analyses from sediment cores and flushed well-screen sediment; four hydrostratigraphic units (figure 2.8) have been defined by Tuttle (1997). Below the coarser topset unit (1), the upper foreset unit (2) comprises the upper sandy part, while the lower foreset unit (3) is the silty-sandy part which becomes increasingly silt- and clay rich with depth and spans the foreset-bottomset transition. In the upper part of the bottomsets there are individual sand beds of circa 1m thickness. The foreset/bottomset unit consists of the lower foreset and upper bottomset units, as these display similar hydraulic conductivities (Tuttle, 1997). The lower bottomset unit (4) consists of silt and clay.

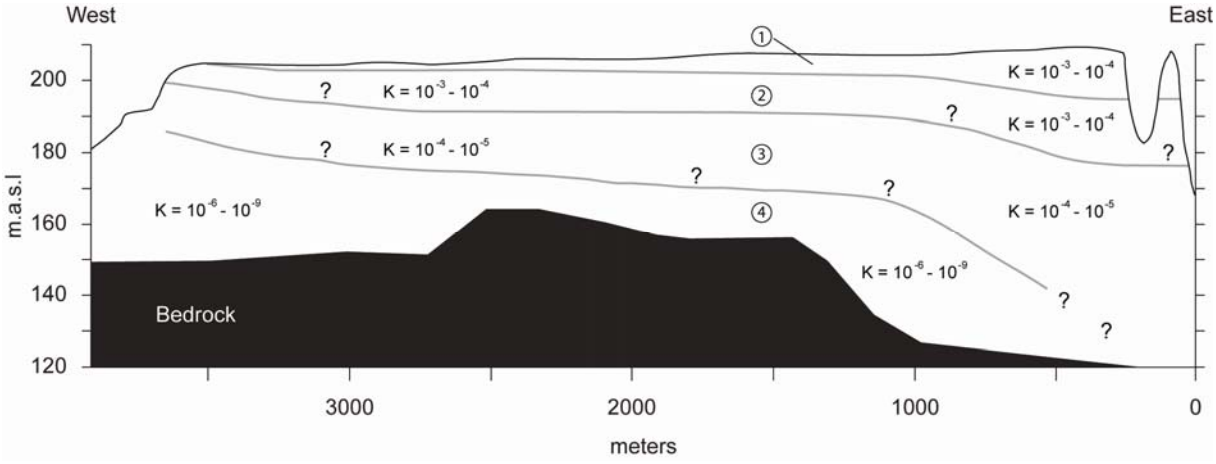

Figure 2.8: Hydrostratigraphic units within the Trandum Delta. K = hydraulic conductivity. 1: topset unit, 2: upper foreset unit, 3: lower foreset unit and 4: lower bottomset unit (modified from Tuttle, 1997).

The groundwater table is mainly situated within the tilted foreset layers, with the saturated zone comprising parts of the upper foreset unit, the lower foreset/bottomset unit and the silty bottomset unit. The various conductivities are given in figure 2.8. In general K decreases as the units become successively more fine-grained with depth. Within each unit K decreases towards distal parts, as the sediments become finer. Local variations might occur due to depositional features such as sand lenses (*e.g.* turbidites) in finer material

2.4.2 Waterbudget

The waterbudget equation may be expressed as follows (Jørgensen & Østmo, 1990);

$$P = E + Q + D + \Delta S \qquad \textit{Eq. 2.1}$$

where P = precipitation, E = evapotranspiration, Q = flow out of the catchment, D = subsurface drainage and ΔS = change in storage.

As the Gardermoen aquifer is made up of relatively coarse unconsolidated deltaic sediments, the infiltration capacity in the sandy surface layers is large, with the surface runoff being generally low (Jørgensen & Østmo, 1990).

The total yearly precipitation, comprising both rain and snow, is in the order of 80 cm (P in equation 2.1), as measured at four stations during the years 1966 – 1974 in the international hydrological decade (Otnes, 1973; 1975; Jørgensen & Østmo, 1990). Approximately half of the yearly precipitation is lost through evapotranspiration ($E \approx 40$ cm in equation 2.1) (Jørgensen & Østmo, 1990), which is the sum of sublimation and the amount consumed by and stored in vegetation. The other half constitutes the potential infiltration.

During winter the groundwater table is lowered when most precipitation is in the form of snow and infiltration is prevented due to frozen ground, while flow out of the catchment and drainage is continuous throughout the year. Flow out of the catchment (Q in equation 2.1) corresponds to approximately 49 cm/y (Jørgensen & Østmo, 1990). The amount of subsurface drainage cannot be measured, but is assumed to be much smaller than the flow out of the catchment (assuming $D \approx 0$ in equation 2.1). Most of the groundwater recharge happens during 3 to 5 weeks in spring, during the snow melting period (Jørgensen & Østmo, 1990). Rainfall during autumn makes up the other important source of renewal. The rise of the groundwater table is delayed approximately by one month relative to infiltration, and reflects the retention time in the unsaturated zone.

During the snow melting period the water saturation is approximately 20%, and water flow through unsaturated zone has a velocity of 0.2 m/d (Jørgensen & Østmo, 1990). In summer the water saturation, and correspondingly the hydraulic conductivity, is lower, with

percolation velocities in the order of 0.1 m/d (Jørgensen & Østmo, 1990). In summer the infiltration might also be negative due to root suction. In the saturated zone the groundwater flows with velocities of 0.1-0.2 m/d, and has a mean residence time of 30 years (Jørgensen & Østmo, 1990).

2.4.3 The Gardermoen Airport

When the building of Gardermoen Airport was approved in 1992, it was on the condition that the groundwater quality would not be deteriorated and that ravines and kettlehole lakes would be preserved.

At the airport large amounts of deicing chemicals are being used every year. These are mainly glycol on aircrafts and acetate and/or formeate on runways. In low concentrations, and spread diffusely across large areas, these chemicals are degraded in the unsaturated zone. There are, however, uncertainties connected to the properties of the additives in the chemicals. Point spill of jet fuel is another source of contamination at the airport. Waste water with high deicing-concentrations is collected and treated either at a municipal treatment plant (where carbon is used to reduce nitrate) or infiltrated through soil having ideal properties (hydraulic and biologic), within basins at the airport, for the breakdown of contaminants.

Covering a large surface area with asphalt changes the infiltration properties and potentially the water balance. Infiltration through the ground is prevented and less precipitation is consumed by vegetation, which together cause an infiltration surplus (Helberg, 2000). The total infiltration is, however, restricted to smaller areas than before. The railway connected to the airport lies in an artificial ditch/tunnel below the groundwater table, under which water is pumped out continuously. In order to fulfil the requirements to maintain the water balance, a complex system of pumping, drainage and injections of groundwater are operated at the airport. The shape of the groundwater table is changed below and around the airport, but normal recharge through the ravines to the rivers Sogna and Vikka and the kettlehole lakes in the northeast must be ensured.

2.4.4 Main Geochemical Processes

The river Risa is mainly fed by groundwater. It has a stable discharge and a nearly constant chemical composition throughout the year (Jørgensen *et al*., 1991). The composition of the system input, resulting from wet and dry deposition, is different from the output concentrations, exemplified in the river Risa. Jørgensen *et al*. (1991) suggest that the following processes are the most important geochemical processes taking place along the aquifer flow path, affecting groundwater chemistry and causing the deviation between inflow and outflow.

Calcite Dissolution

There are high output values of Ca^{2+}, Mg^{2+} and HCO_3^-, which are mainly due to carbonate weathering. The dissolved carbon dioxide pressure has been measured in the field to be approximately ten times the atmospheric pressure, with seasonal fluctuations (Basberg, 1999). The CO_2 pressure stabilizes with depth. 50% of the bicarbonate in the aquifer results from calcite dissolution and carbon dioxide (Jørgensen *et al*., 1991; Basberg, 1999). Jørgensen *et al*. (1991) suggest that the thickness of the decalcified zone at Moreppen is 10m. Pyrite oxidation may also contribute to calcite dissolution. Released protons may associate with the carbonate ion and increase calcite solubility (Basberg, 1999). Different mechanisms of calcite dissolution are, according to Plummer *et al*.(1978);

$$CaCO_3 + H^+ = Ca^{2+} + 2HCO_3^- \qquad \text{at pH} < 3.5 \qquad \textit{Eq. 2.2}$$

$$CaCO_3 + H_2CO_3^* = Ca^{2+} + 2HCO_3^- \qquad \text{at } 3.5 < \text{pH} < 7.0 \qquad \textit{Eq. 2.3}$$

$$CaCO_3 + H_2O = Ca^{2+} + 2HCO_3^- + OH^- \qquad \text{at pH} > 7.0 \qquad \textit{Eq. 2.4}$$

Where $H_2CO_3^* = CO_{2(aq)} + H_2CO_3$

Water infiltrating the ground quickly equilibrates with the given P_{CO2}. After percolating through the decalcified, unsaturated zone, the water reaches the saturated zone with a certain concentration of dissolved carbon dioxide. The calcite dissolution processes in the aquifer are best described as a closed system dissolution. Equilibrium arises in accordance with how much carbon dioxide that is fed to the system.

Pyrite Oxidation

The total output of sulphate from the system is higher than the input from wet and dry deposition (Jørgensen *et al*., 1991). Weathering of pyrite, which is present in the sediments, is the most probable cause of the excess sulphate (Jørgensen *et al*., 1991). The process may be described as follows (Appelo & Postma, 2005);

$$FeS_2 + 7/2\, O_2 + H_2O = Fe^{2+} + 2SO_4^{2-} + 2H^+ \qquad \textit{Eq. 2.5}$$

$$FeS_2 + 14Fe^{3+} + 8H_2O = 15Fe^{2+} + 2SO_4^{2-} + 16H^+ \qquad \textit{Eq. 2.6}$$

$$Fe^{2+} + 1/4\, O_2 + H^+ = Fe^{3+} + 1/2\, H_2O \qquad \textit{Eq. 2.7}$$

$$Fe^{3+} + 1/2\, H_2O = Fe(OH)_3 + 3H^+ \qquad \textit{Eq. 2.8}$$

$$Fe^{3+} + 2H_2O = FeOOH + 3H^+ \qquad \textit{Eq. 2.9}$$

The energy yield of eq. 2.5 is much higher than for eq. 2.6. Incomplete oxidation is therefore likely, with the result being a solution rich in Fe^{2+} if the pH is not increased. The amount of sulphate produced by the weathering process above is reduced by adsorption of sulphate in the aquifer and reduction of sulphate to sulphide in deep, anoxic lake water (Jørgensen *et al*., 1991). Where there is oxygen present in the groundwater, dissolved ferrous iron is unstable and will be oxidized to form a precipitate of ferric hydroxide as shown in equations 2.7 through 2.8. The amount of dissolved oxygen will decrease along a flow path where pyrite is oxidized.

At the pyrite/calcite horizon it can be expected that most of the available oxygen will be consumed in pyrite oxidation and releases protons (Basberg, 1999). The resulting drop in pH facilitates silicate weathering, but the extent of this will be limited since acidification will be buffered by calcite dissolution (Basberg, 1999).

Silicate Weathering

Cations like Na^+, K^+, small amounts of Al^{3+} and silica and also Ca^{2+} and Mg^{2+} may be subscribed to silicate weathering. According to studies performed by Teveldal *et al*. (1990) at Nordmoen, the most important weathering processes in the upper soil profile are complete breakdown of chlorite and biotite, and transformation of muscovite to vermiculite and smectite.

Fossil Seawater

As the distal parts of the delta was deposited in a marine environment, the lower aquifer stores fossil seawater (Jørgensen *et al*., 1991). In the budget calculations performed by Jørgensen *et al*. (1991), the output of chloride was higher than the input, which was interpreted to be caused by leaching or diffusion of old seawater from deep sediments. Based on average seawater composition, it was calculated that the discharge contained 2.61 mg/l sea salt or 0.01% fossil sea water. The low contribution indicates that most of the fossil seawater has been removed, or that transport through the sediments is very slow (Jørgensen *et al*., 1991).

In summary; carbonate dissolution, pyrite oxidation and silicate weathering are the main geochemical processes contributing to the assemblage of ions in the groundwater at Gardermoen. These main, and other minor, processes will be related to the dataset and discussed further in chapter 7.

Lake Chemistry

The extent of groundwater influence on the lake water chemistry and water level varies between the lakes in the Romerike area. A high content of electrolytes reveals influence from ground water. This is most common in drainage lakes, which have permanent inlets draining groundwater from the surroundings (Hongve, 1977). In these lakes the water is of Ca^{2+}/HCO_3^- type and similar to groundwater in composition. Some seepage lakes (less groundwater drainage) also have elevated electrolyte content. To determine the degree of groundwater influence in these is difficult, since the springs and inlets are invisible due to low flow. In some the water levels are identical with the groundwater level, and display the same variation (Hongve, 1977). The lakes showing the lowest electrolyte content are seepage lakes with constant water levels mostly above the groundwater level in the area. They are not at all influenced by groundwater due to tight basin walls. This sealing effect may be the result of

precipitation from the water (*i.e.* calcium carbonate or ferric hydroxide) or sedimentation of fine, particulate matter (Hongve, 1977). These lakes are fed solely by precipitation and surface runoff. The latter is contributing less due to the flat ground and permeable surface layers in the area (Hongve, 1977).

3. Groundwater Chemistry

3.1 Sampling Procedures

Most of the sampled wells are permanently open wells with an inserted 6 cm (diameter) plastic pipe and a depth specific filter of varying length situated just above the well bottom. When sampling these wells, a stainless steel Grunnfos submersible pump was used. A few wells that are or have been in use for agricultural or groundwater monitoring purposes have permanent submersible pumps installed (FU1, K1, TW1 and TE1). Measurements performed in the field were pH, temperature and electrical conductivity. All readings were made after pumping three times the well volume, when values were stabilized. Subsequently water samples were collected. Samples to be analysed for organic content were put in non-adsorbing glass bottles having Teflon membrane in the screw cap. Samples for alkalinity and oxygen content analyses were contained in gas-tight glass bottles (Winkler-bottles) and analysed the same day, while samples for remaining chemical analyses were filtrated through 0.45 µm disposable filters into plastic bottles and later kept in a dark and cold (7-8^{o}C) storage. HNO_3 and HCl were added to two different samples for conservation of cations and alkalinity, respectively.

3.1.1 BAT Wells

Six of the sampled wells have filter-tips permanently installed in the bottom, accommodated to the BAT sampling system. The system components are depicted in figure 3.1. The procedure is to lower an evacuated glass sampling container into the well, where it will, when it reaches the bottom, establish contact with the filter-tip. A double-ended hollow needle penetrates silicon membranes in both the sample container and the filter-tip, and water is sucked in. The time it takes to balance the pressure depends on the permeability of the aquifer material. The wells sampled here are all located in fine sand deposits (distal part of delta), and to fill a 25 ml sample container takes approximately 5 minutes. When the sampling equipment is pulled up, the needle is disconnected first from the sampling container, then from the filter-tip. The silicon material immediately seals itself.

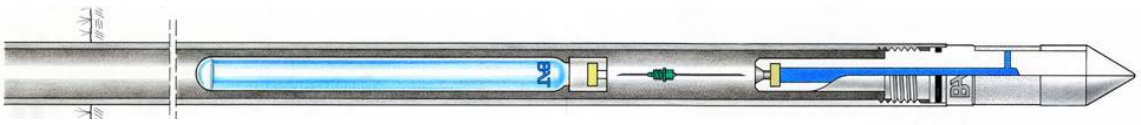

Figure 3.1: BAT groundwater sampling system (BAT, 2006).

3.2 Methods of Analysis

3.2.1 Ion Chromatography

The principle of all chromatography is to separate the different constituents in a sample. In liquid chromatography, which is used here to determine major cat- and anions in the water samples, ions are separated when the water sample is pumped through an exchanging column. Separation arises due to differences in equilibrium distribution in the mobile and stationary phases. Electrical conductivity is proportional to the dissolved ion content and is measured to estimate the ion concentrations (Johansson, 1987). Most samples have been analysed for both anions and cations using a Dionex IC 25. Some are, however, analysed for only anions on a Dionex QIC-2.

The eluent is the liquid that drives the sample through the instrument. The mixture used in Dionex QIC-2 consists of 1.7 mM $NaHCO_3$ and 1.8 mM Na_2CO_3. In Dionex IC 25 an eluent generator was used, with a KOH eluent for anions and a MSA (methanesulfonic acid) eluent for cations. The sample first passes through a front column (figure 3.2) protecting the main column. Inside it, particles like dust and sand or bacteria that may clog the column are held back (Johansson, 1987). When the sample subsequently passes through the main column, the ions are separated in time and space (figure 3.2). Within the column there is a three dimensional lattice structure. Here columns HPIC-AS4 (Dionex QIC-2), IonPac AS16 (anions, Dionex IC 25) and IonPac CS16 (cations, Dionex IC 25) were used. Light ions with weak electrical charge will pass more quickly than heavier ions with higher charge, due to the columns affinity for the latter (Johansson, 1987). Consequently, the ions emerge on the other side in a fixed order given by their size, charge and shape. The time needed to pass through the column depends on the pumping speed and the eluent composition.

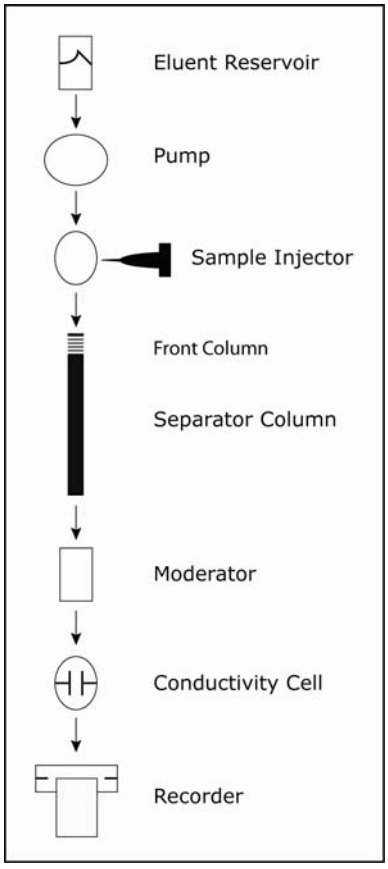

Figure 3.2: Configuration of ion chromatograph (modified from Rudolph-Lund, 1997).

In the moderator (figure 3.2), following the main column, the objective is to eliminate the contribution to the electrical conductivity from the eluent. Finally the sample passes through the detector, which simply measures the electrical conductivity via two electrodes (figure 3.2). The current induced in the solution by the electrode voltage is directly proportional to the dissolved ion content as long as the concentrations are not too high, but within a linear area defined for the device (Johansson, 1987). The data emerge as a chromatogram, which needs to be interpreted in terms of which peaks, arriving after a delay time, are representing the different anions. The area of the peak is compared to a peak generated by a known standard, and the concentration may then be calculated.

3.2.2 Flame Atomic Absorption Spectrometry

Flame atomic absorption spectrometry has been used to determine the concentration of various cations. This method is based upon how electromagnetic radiation interacts with matter. In order to extract quantitative information about the amount of matter, a spectrophotometer which measures the intensity of radiation, which is reduced due to absorption by the analyte, is used (Haswell, 1991).

During operation light is passed through a cloud of atoms. To produce the atom cloud required for making the measurements, sample water is aspirated into a flame (figure 3.3). The applied thermal energy produces free, unexcited ground state atoms which absorbs light at the analytical wavelength from a source lamp (Beaty & Kerber, 2002).

The amount of absorbed light is proportional to the number of atoms in the light path. In order to quantify individual elements in the presence of others, it is necessary to use different light sources with characteristic wavelengths (Beaty & Kerber, 2002). The light with reduced intensity is directed onto a detector and measured (figure 3.3). By comparing with the initial light intensity the amount of absorbed light is determined.

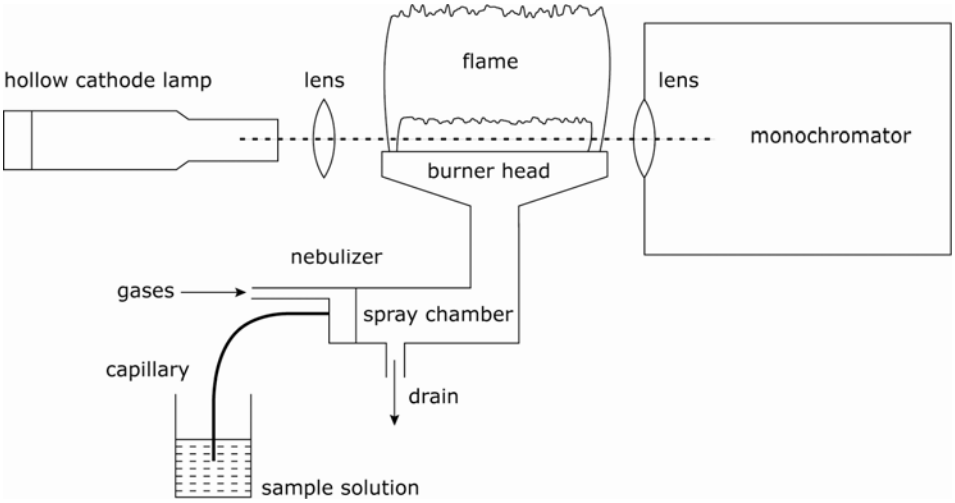

Figure 3.3: Configuration of an atomic absorption spectrometer (modified from Potts, 1992).

The bright light source used is a hollow cathode lamp. It works as a line source in order to measure the narrow light absorption. The lamp cathode is made of the same metal whose spectrum is to be produced and is, together with the anode, sealed within a gas-filled glass cylinder (Beaty & Kerber, 2002). Gas atoms are ionized by the anode/cathode electric potential. Ground-state metal atoms attain emission state through kinetic energy transfer in impacts with the fill gas ions.

So called multi-element lamps have a cathode constructed from mixtures or alloys of two or more different metals. They may be used as a source for all metals contained in the cathode (Beaty & Kerber, 2002). These lamps shorten the time spent and the cost of the analyses. There are, however, drawbacks if high precision or low detection limits are required. The intensity of the emission for a single element is often lower when using a multi-element lamp (Beaty & Kerber, 2002). In the analysis performed here multi-element lamps have been used for Ca/Mg and Na/K.

In table 3.1 properties of the analysed elements are listed. All of these wavelengths lay within the UV (100-400 nm) or visible light (400-720 nm) spectra.

Elements	D.L.	λ	C.R.	O.W.R.
	µg/ml	nm	µg/ml	µg/ml
Mg	0.00020	285.2	1.00-4.00	0.1-0.4
K	0.00300	766.5	0.50-2.00	0.5-2.0
Mn	0.00300	279.5	0.50-4.00	1.0-4.0
Ca	0.00100	422.7	1.00-4.00	1.0-4.0
Ba	0.01500	553.6	5.00-20.00	10.0-40.0
Fe	0.00300	248.3	1.00-10.00	2.5-10.0
Li	0.00160	670.8	1.00-4.00	1.0-4.0
Na	0.00023	589.0	1.00-2.00	0.15-0.60
Sr	0.00100	460.7	1.00-4.00	2.0-10.0

Table 3.1: Properties of analysed elements. D.L. = Detection Limit, **λ** = Wavelength, C.R. = Calibration Range and O.W.R. = Optimum Working Range. Detection limits from Haswell (1991).

Constant wavelengths, as given in table 3.1, have been used here when analysing elements of varying concentration. If concentrations exceeded calibration ranges (table 3.1) as to produce an unacceptable fault rate (>10%), samples were diluted 1:10 or 1:100, instead of adjusting the wavelength.

3.2.3 The Molybdate Blue Method

The concentration of silica has been determined by the Molybdate Blue Method, in which the silica concentration is measured indirectly by spectrophotometry. Analyses have been performed based on the following principles, as described by Aagaard & Wensaas (1994). When silicon is present in solution in the form of silicic acid (H_4SiO_4) or silicate, it will react with ammonium molybdate in acid solution and form a yellow silicon molybdate complex. This complex is reduced by the addition of sodium sulphite (Na_2SO_3), and the solution obtains a molybdate blue colour. The concentration of SiO_2 may then be determined by measuring the extent to which a ray of light with known wave length, here 710 nm, is absorbed by the complex compared to a standard solution.

3.2.4 Alkalinity

The alkalinity of a water sample equals the number of dissociated weak acid equivalents. It is therefore an expression of how much acid that can be buffered by solution. Carbonic acid anions are the main contributors, with other weak acids mostly being insignificant in groundwater. The following simplification for alkalinity, *A*, is therefore commonly made;

$$A_{carbonate} = [HCO_3^-] + 2[CO_3^-] \qquad \textit{Eq. 3.1}$$

When pH is lower than 8.3, the carbonate contribution is less than 1% (Appelo & Postma, 1999). This applies for most water samples analysed in this study. It is to be noted, however, that the alkalinity measured by use of the methods described below is the total alkalinity, given by;

$$A_{total} = A_{carbonate} + \Sigma A_{weak\ acids} \qquad \textit{Eq. 3.2}$$

Autotitration

All samples have been titrated by means of an autotitrator, TT 80 Titrator was used. The device produces a continuous stream of HCl of optional molar strength, which is directed into a volume *V* of water sample while stirring constantly. The pH is measured continuously. The volume of acid added and the corresponding change in pH is registered by a PHM 82 Standard pH meter connected to a printer in order to transcribe a curve directly. The point of equivalence is found manually on the output curve, and the alkalinity *A* given in *mekv/l* is calculated using the following relationship;

$$A = \frac{y \cdot n \cdot 1000}{V} \qquad \textit{Eq. 3.3}$$

Where y = ml HCl, n = molarity of HCl and V = ml sample water (Bøyum & Kaasa, 2001).

Gran's plot

As an extra reassurance some samples have been acidified in the field, by immediately adding HCl (25 ml 0.001M) to the sampled water (2 ml). The alkalinity may then be determined by

titrating with NaOH and finding the equivalence point by using the Gran's plot method, in which volume base added is plotted against the Gran's function, *F*, below.

$$F = (V + V_0) \cdot 10^{-pH} \qquad \textit{Eq. 3.4}$$

V = volume base added and V_0 *= volume of water and acid* (Aagaard & Wensaas,1994).

Field Titration with Indicator

A rough estimate of the alkalinity was also made in the field by manual titration. An indicator, which is a pH sensitive colour complex, was added to 20 ml sample. The indicator used here was bromophenol blue. It changes from yellow at pH 3.0 to purple at pH 4.6. The point of equivalence in groundwater samples normally lies around pH = 4.5, while the initial pH in waters at Gardermoen were in the range of 6.0 – 8.6. Water samples with bromophenol blue added display a colour shift from dark bluish purple to light greyish purple at pH ≈ 4.5, as observed in the lab. In the field 0.02 M hydrochloric acid was added to 20 ml of sample through a burette, until there was a shift in colour. The alkalinity calculated from this (eq. 3.3) was only used qualitatively to ensure that no large changes had occurred during hours of storage and transport to the lab.

3.2.5 Dissolved Oxygen

The principle of this method for determining the dissolved oxygen content is based on a series of induced reactions. When adding divalent manganese hydroxide to oxygen containing water samples, the oxygen will immediately oxidise an equivalent amount to become trivalent (Bøyum & Kaasa, 2001). Provided an excess amount of reagent, the amount of trivalent manganese corresponds to the dissolved oxygen content. To determine the produced amount of trivalent manganese, sulphuric acid and potassium iodide are added in order to have the manganese release an equivalent amount of iodide by oxidation (Bøyum & Kaasa, 2001). Finally the iodide content is determined by titration with sodium thiosulphate of known concentration. This entire process may be summarised by the following sequence of equations (Bøyum & Kaasa, 2001);

$$2MnCl_2 + 4KOH = 2Mn(OH)_2 + 4KCl \qquad \textit{Eq. 3.5}$$

$$2Mn(OH)_2 \; {}^{1}\!/\!_{2}\, O_2 + H_2O = 2Mn(OH)_3 \qquad \textit{Eq. 3.6}$$

$$2Mn(OH)_3 + 3H_2SO_4 = Mn_2(SO_4)_3 + 6H_2O \qquad \textit{Eq. 3.7}$$

$$Mn_2(SO_4)_3 + 2KI = 2MnSO_4 + K_2SO_4 + I_2 \qquad \textit{Eq. 3.8}$$

$$2Na_2S_2O_3 + I_2 = 2NaI + Na_2S_4O_6 \qquad \textit{Eq. 3.9}$$

When titrating to find the unknown amount of iodide as described in equation 3.9, 50 ml of water sample was used in order to use the following relationship given by Bøyum & Kaasa (2001) to calculate ml O_2 / l ;

$$V = 111.96 \cdot a \cdot n \qquad \textit{Eq. 3.10}$$

Where V = ml O_2 / l, a = ml thiosulphate and n = normality of thiosulphate.

3.2.6 LiquiTOC

Here a liquiTOC apparatus has been used to determine total inorganically bound carbon (TIC), non purgeable organic carbon (NPOC) and total bound nitrogen (TN_b). All of these parameters are determined from one sample injection into a multi-functional reactor.

First TIC is purged by adding acid (HCl) at a temperature of 70^{o}C in the reactor. The sample continues through a two zone combustion system in which the first furnace is operated dynamically between 90-900^{o}C and the second heats the catalyst for post combustion with a temperature of 900^{o}C. The CO_2 (from oxidation of NPOC) and NO (from oxidation of TN_b) formed are transported with carrier gas (synthetic air) through an electronic mass flow controller which ensures steady flow, before entering a wide range multi-channel IR (infra red) photometer for detection.

3.2.7 Thin Layer Chromatography- Flame Ionisation Detection (TLC-FID)

The Iatroscan instrument combines thin layer chromatography (TLC) and flame ionisation detection (FID) in order to detect, quantify and classify the organic fraction. When using this method to analyse groundwater samples, the first step is to extract the organic content. Di-chloro-methane (DCM) was added to the water samples of known volumes around 2 dm^3 contained in non-adsorptive glass bottles with Teflon-coated caps, which were subsequently shaken vigorously manually and then over some time in a machine. As the majority of organic substances prefer solution in apolar liquids, most of these substances contained in the polar water phase will migrate and solve in DCM when contact is established. The two phases contained in the sample bottle were transferred to a separatory funnel for separation. The DCM sinks to the bottom, as it has higher density than water; 1.325 g/cm^3, and is easily drained from the funnel. The last step of sample preparation was evaporation, which is necessary in order to increase the relative concentrations. The initial volume of DCM; approximately 100 ml, was reduced to 50 µl before analysis.

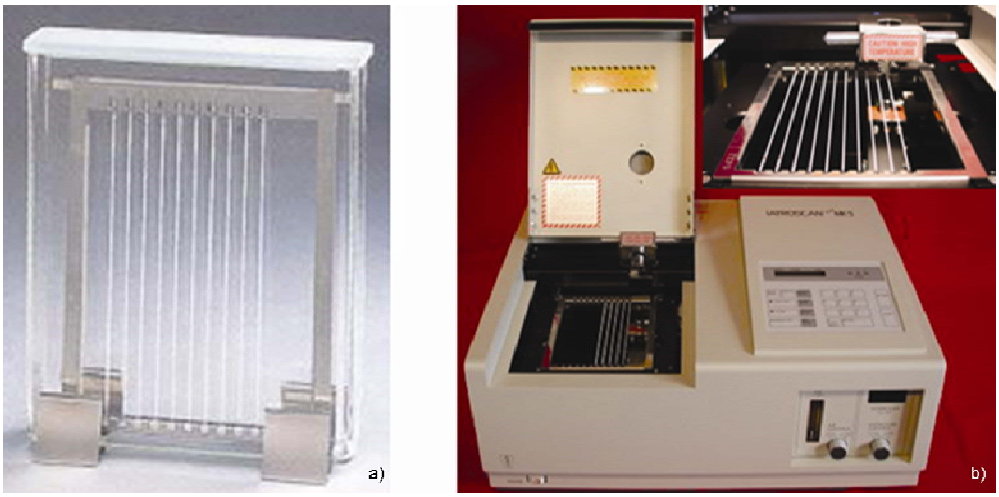

Figure 3.4: a) Set of chromarods in solvent. b) Set of chromarods placed in the iatroscan instrument, detail photo of the burning of chromarods. (INRA, 2006).

The Iatroscan TH-10, MK IV (Iatron inc., Tokyo) instrument (figure 3.4b)) is equipped with a flame ionisation detector (FID) and interfaced with an electric integrator (Perkin-Elmer LCI-100) for quantification. Components were separated using quartz rods coated with silica to perform like columns (Chromarods-S III) and solvents of different polarity (figure 3.4a)). 5 µl of sample was applied to a fixed point on the chromarods. In each set one blank sample and a standard oil sample (1 µl NSO-1 oil) were run as references. The rods were put in hexane for 32 minutes (figure 3.4a)), causing saturated compounds to rise to the upper part of the rods.

After drying in air for 3 minutes, the rods were placed in toluene for 8 minutes, causing aromatic compounds to rise to the middle part of the rods. The result was three bands, each representing a group of compounds (saturated, aromatic, polar). Finally the rods were run through a flame of hydrogen and air (figure 3.4b)). The compounds produce ions as they burn, which conducts electricity. A Flame Ionisation Detector (FID) registers changes in the current within the flame. The final result is drawn as chromatograms and quantified by an integrator.

3.2.8 Gas Chromatography - Flame Ionisation Detector (GC - FID)

In gas chromatography individual organic components are separated due to differences in their ability to partition from the stationary to the mobile phase. Samples are vaporized before they enter the chromatographic column. A film layer on the inside of the column acts as the stationary phase. Short-chained molecules travel quickly through the column, while longer or more complicated molecules are retained. The carrier gas, or the mobile phase, is an inert gas. Nitrogen (N_2) is used in this study. The column is slowly heated from 40^{o}C up to 325^{o}C in order to mobilize compounds having lower vapour pressures. When molecules exit the column, they are passed through a flame ionisation detector (FID, described in section 3.2.7). The signal is registered by a computer, producing a chromatogram.

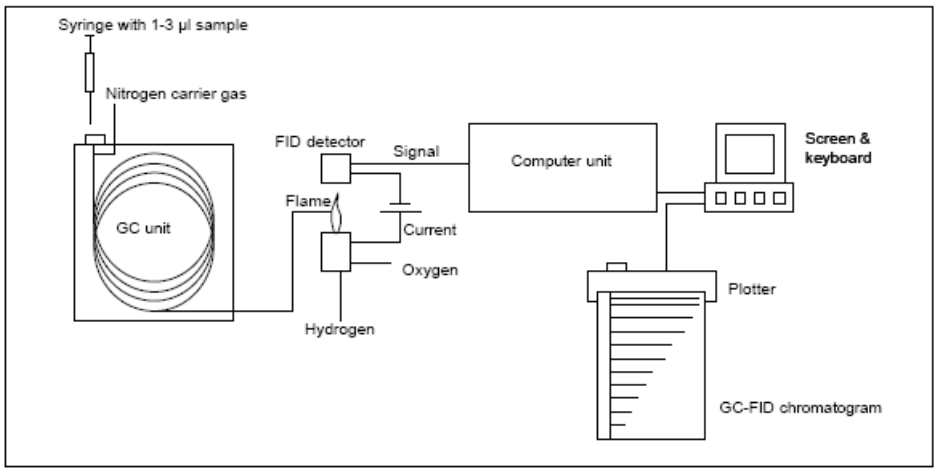

Figure 3.5: GC-FID configuration (Pedersen, 2002).

The GC-FID instrument used in this study is a Varian Capillary Gas Chromatograph Model 3500 with a 50 m length HP Ultra-1 column, which has a 0.2 mm internal diameter and a film thickness of 0.33 µm.

3.2.9 Gas Chromatography – Mass Spectrometry (GC-MS)

With Gas Chromatography – Mass Spectrometry (GC-MS) identification and quantification of individual compounds are possible. After the chromatographic separation (cf. section 3.2.8) the molecules in the sample are ionized by a wolfram filament and introduced to a quadropole analyzer. Here ions of interest may be selected according to their mass. Each molecule fragment may be characterized by a ratio (m/z) of its mass (m) and electronic charge (z). The detector registers the m/z value and amount of each ion, which is plotted against the retention time by a computer.

The GC-MS instrument used in this study was a Fisons MD800 quadropole-instrument with a 50 m long Chompack, WCOT, CP-sil 5 CB LOW BLEED/MS column, which had a 0.32 mm internal diameter and a film thickness of 0.40 µm. The starting temperature was 80^{o}C, with a subsequent slow increase to a final temperature of 310^{o}C.

3.3 Results

3.3.1 Groundwater Characterisation

Analyses of the set of new water samples taken mainly from deeper parts of the Northern Romerike Aquifer confirm, like previous studies (*e.g.* Hongve, 1977; Jørgensen *et al.*., 1991; Dagestad, 1998; Basberg, 1998), that groundwater at Gardermoen is mainly of Ca/HCO_s^- type. In the Piper-plot below the major ions for each sample are plotted, displaying the bulk chemical composition. However, some deviation from the dominating Ca^{2+} - HCO_s^- system occurs. Deviating points in the upper section are caused by elevated concentrations of sulphate and chloride, while in the lower section points deviate due to larger influence of sodium and magnesium.

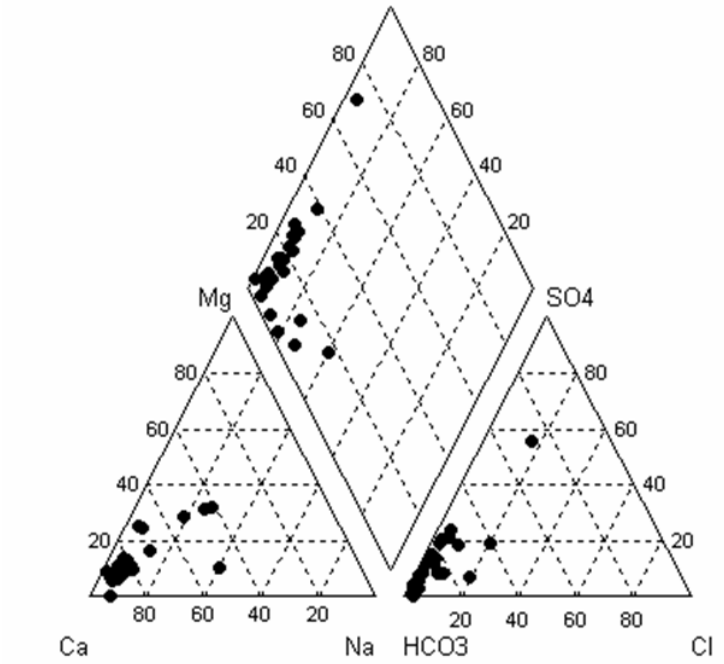

Figure 3.6: Bulk chemical composition of water samples plotted in a Piper diagram. Each triangular plot displays relative concentrations of cations and anions, given in percentage of total meq/l. Corresponding pairs are extrapolated onto the diamond shaped diagram.

3.3.2 Inorganic Ions

The accuracy of chemical analysis of ion concentrations may be estimated based on the principle of electro-neutrality in water. In order to have electrical balance, the sum of positive and negative charges in the water should be equal. The percentage deviation may be estimated as follows (Appelo & Postma, 2005);

$$E.B.(\%) = \frac{\left(\sum cations + \sum anions\right)}{\left(\sum cations - \sum anions\right)} \cdot 100 \qquad \textit{Eq. 11}$$

Where *E.B.* = Electrical Balance given in % and *cations* and *anions* are expressed as meq/l and inserted with their sign of charge. The sums are normally mainly dependent on the major cations Na^+, K^+, Mg^{2+} and Ca^{2+}, and anions Cl^-, HCO_3^-, SO_4^{2-} and NO_3^-. In some cases other elements, like Fe^{2+}or NH_4^+ in reduced groundwater or H^+ or Al^{3+} in acid waters, might contribute significantly (Appelo & Postma, 2005). Here all analysed ions are included, which are cations: Ca^{2+}, Na^+, Mg^{2+}, K^+, Fe^+, Mn^+, Ba^{2+}, Sr^{2+}, NH_4^+ and anions: HCO_3^-, Cl^-, SO_4^{2-}, NO_3^-, NO_2^-, F^-, Br^- and PO_4^{3-}. In general, a fairly good analysis has E.B. < 2% (Appelo & Postma, 2005).

The concentrations of major ions and charge balances for the sample set are listed in appendix B. The deviations are in the range of -0.24 – 0.16 %, which is low and indiative of high accuracy. The total dissolved content (TDS), also listed in appendix B, is within the range of 47.6 – 255.2 mg/l. Further discussion on quantitative and regional distributions of individual ions is given in section 7.1.

In the process of analysing the water samples several technical problems were encountered. Because of this, most wells have been re-sampled and re-analysed one or several times. The dataset consequently spans a time interval of approximately six months (final sampling dates are given in appendix B1). As all well screens are well below the groundwater table, the seasonal change is assumed to be insignificant when comparing the samples. Major ions; Ca^{2+}, Mg^{2+}, Na^+, K^+, Cl^-, SO_4^{2-} and NO_3^- were analysed by anion chromatography on Dionex IC 25, for all wells except TM1 – 5. Remaining ions (all ions in TM1 – 5) were analysed with Dionex QIC-2 (anions), and atomic absorption (cations). Despite different methods of

analysis all ions have been compared in the same way, as samples for cations and anions, were taken from the same bottles, respectively.

3.3.3 Field Parameters: pH, Electrical Conductivity and Temperature

Values for the field parameters: pH, electrical conductivity (EC) and temperature as measured *in situ* are given in appendix B1.

pH

pH is an important parameter with respect to mineral saturation states. To obtain reliable measurements in the field, however, proves difficult. The electrode stabilizes only to a certain extent; it never reaches a complete standstill. The pH value keeps increasing slowly. In order to make the results comparable, the electrode was placed in a bucket with continuously flowing water (imitating a flow cell); after pumping three well volumes, measurements were taken subsequently after ten minutes. The problems with measuring pH are related to the removal of groundwater from its *in situ* position. When contact with atmospheric oxygen is established, components present in anoxic groundwater, like for instance Fe^{2+} or H_2S, may be oxidised and affect pH values. Degassing of CO_2 might also increase pH and cause precipitation of $CaCO_3$ (Appelo & Postma, 2005).

Another source of error is the temperature factor. The voltage output from the electrode, and correspondingly the pH of any solution, is a function of temperature. The dissociation constant of water, K_w, like all other equilibrium constants, varies with temperature. The neutral point of the pH scale is 7 only at 25°C. At lower a temperature, which is the case here, K_w is lower. This causes the pH scale to comprise a larger interval; *e.g.* 0 – 14.53 at 10°C (Faure, 1998). The pH electrode used in the field was calibrated for two points; pH = 7 and pH = 4, at 25°C. Considering the above, true values may be slightly higher. This variation is, however, probably minor compared to the total uncertainty in the measurements.

The pH measurements taken in the field averages at 7.3. In figure 3.7 pH measurements are plotted against depth. There is a clear trend for pH to increase with depth, which is expected as pH increases while calcite weathering proceeds. According to Jørgensen *et al.* (1991) pH is close to 5 when the weathering of calcite starts, at the calcite dissolution front, and 7.7 in the

river Risa. Weathering of several other minerals (*e.g.* Albite and K-feldspar) also consume acid and increases pH, but to a lesser extent.

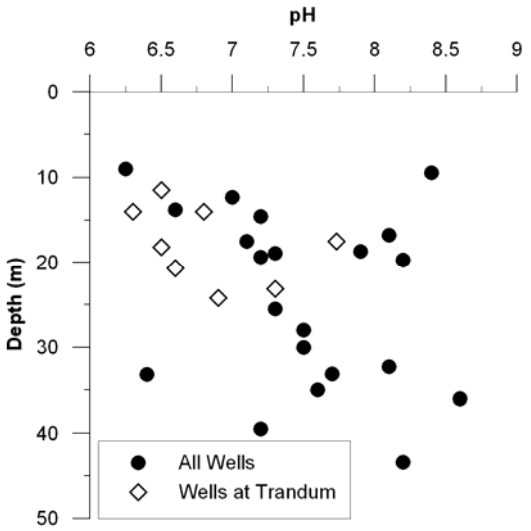

Figure 3.7: Plot of pH versus depth for sampled wells. The dotted line emphasises what seems to be the normal trend, but it is not statistically fitted.

The wells at Trandum landfill also display increasing pH with depth. The eight wells at Trandum have an average pH of 6.8, while the pH in the sample set excluding the Trandum wells, averages at pH 7.5. In accordance with studies made by Sæther *et al.* (1992) and Basberg (1999) the values in central parts of the landfill (wells TM2 – 5) are markedly lower than the surrounding mean. The multilevel well south of the landfill (TM6 – 8) seems to have below average values in the two upper filters, but the lower screen, at 17.5 m, display a pH above average. Well TM1 is situated at the northern fringe of the landfill and display a pH close to average.

The largest deviations in the "all wells" series in figure 3.7 are in samples from wells BAK1 and BAK2 at Kabberudsæther, BAR1 at the Horse Ranch and TE1 at Lake Transjøen (which has a non depth-specific filter with screen length ~ 20 m) which are more acidic, and wells GW1, GW2 and GE1 at the airport, wells TW1 and TW2 at Lake Transjøen and BAV2 at Vigstein farm, that are more alkaline.

Electrical Conductivity

The electrical conductivity is a measure of the waters ability to conduct an electric current, which is dependent on the concentration of ions in solution. It proves to be a reliable parameter with high reproducibility when performing field measurements. EC yields a fair estimate of the sum of anions or cations. For EC below 1500 µS/cm the following relationship is valid at 25°C (Appelo & Postma, 2005);

$$\sum anions(meq/l) = \sum cations(meq/l) \approx \frac{EC}{100}(\mu S/cm) \qquad \textit{Eq. 12}$$

As an indication of the quality of water analysis, in addition to the electro-neutrality criterion (cf. section 2.3.2), a comparison of EC and ion concentrations according to equation 12 is listed in appendix B4.

Since most groundwaters have relatively low ionic strength (Hongve, 1977), high EC might indicate additional ionic input in the form of contamination. Sæther *et al*. (1992) defined groundwater in the Trandum area to be contaminated if EC was higher than 400. Using this definition, and stating, based on figure *3.8* and the general average of 7.3, that waters with pH lower than 7 are acidic well below average, the water samples may be classified with respect to contamination. This is done in figure 3.8 below.

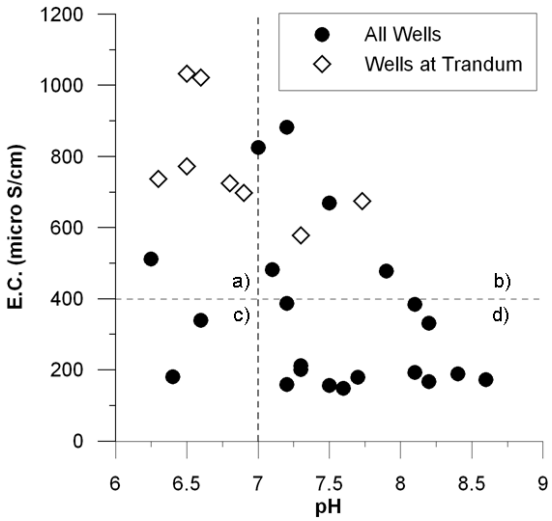

Figure 3.8: Plot of pH versus electrical conductivity for all wells. Wells situated at the Trandum landfill are in a separate series. a) Contaminated samples, b) slightly contaminated samples, c) and d) uncontaminated samples.

When sorting the samples with respect to pH and EC (figure 3.8), all samples from Trandum are defined as contaminated. Wells TM1 at the northern fringe, and TM6 which has the deepest screen (17.5 m) downstream of the landfill, are, however, only slightly contaminated according to this definition. The wells at the landfill show a distinct decrease of EC with depth, while pH increases with depth. This trend is evident both at (TM1 – 5) and downstream (TM6 – 8) of the landfill. The downstream multilevel well does, however, display lower values.

The only well not situated at the landfill clearly belonging to section a) in figure 3.8 is BAK1 at Kabberudsæther. Among samples defined as slightly contaminated, not situated at Trandum, are well K1 at Kabberudsæther, FU1 at Furusmo and GW1, GE2 and GE3 at the airport. Wells in section c); BAR1 and BAK2, are acidic below average, but do not have above average ionic content. In the case of BAR1, which is shallower, the lower pH might be caused by the infiltration of low pH surface water. It should be noted, however, that deep wells such as FU1 and GW1 with well developed groundwater, may have a higher dissolved content due to natural geochemical reactions along the flow-path.

Temperature

The temperature in deep groundwater is expected to maintain a fairly constant value throughout the year. Elevated values might indicate exothermal biodegradation of organic material. The field measurements of temperature are in general reliable with high reproducibility. A possible source of error concerning wells sampled in the winter, *i.e.* GE1 – 5, GW1 and TM1 – 5, is that the low air temperature (~ -15 ^{o}C) might have cooled the water while measuring. This possible source of error was minimised by ensuring constant through-flow in a relatively large volume (10 l bucket), and measuring well below the water surface.

Wells at Trandum display a higher mean temperature than surrounding wells; 9.0^{o}C. In the central part of the landfill samples TM2 and TM3, the two deeper screens of the multilevel well, both have high temperatures close to 10^{o}C, while in the shallower TM4 it is 6.2^{o}C. In the multilevel well downstreams of the landfill the temperature is slightly higher (~0.5 ^{o}C) in the upper two screens; close to 10^{o}C. TM5, which has a shallow screen close to the central area, has a temperature of 9.3^{o}C, while TM1 at the northern fringe of the landfill has a temperature of 8.8^{o}C.

Among the general well distribution there seem to be no tendency of the temperature to increase or decrease with depth (figure 3.9). Also no apparent regional relation was found. FU1 and RB1 stand out having particularly low (4.6 ^{o}C) and high (10.2 ^{o}C) temperatures, respectively. Remaining samples are evenly distributed in the interval 6.1 – 9.2^{o}C. There is no apparent connection between sampling dates and higher/lower temperatures explaining the large interval. The average temperature for all sampled wells; including wells at Trandum is 8.0, and 7.7 excluding wells at Trandum.

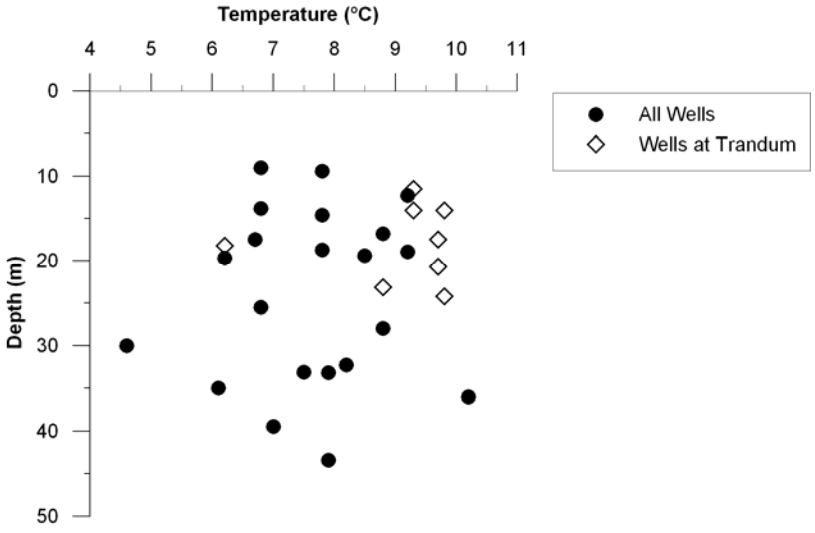

Figure 3.9: Plot of temperature versus depth.

3.3.4 Dissolved Oxygen

Oxygen (O_2) is an important oxidant in aquifer systems. It is supplied through water that has been in contact with the atmosphere infiltrating the aquifer. In the atmosphere P_{O2} = 0.21 atm (Appelo & Postma, 2005). The equilibrium concentration of oxygen may thereby be calculated using Henry's law, which states that at a constant temperature, the amount of a given gas dissolved in a given type and volume of liquid, is directly proportional to the partial pressure of that gas in equilibrium with that liquid (Appelo & Postma, 2005).

The oxygen saturation is a relative measure of the amount of O_2 dissolved in water (DO). It may be calculated as percentage relative to a theoretical maximum concentration given the temperature, pressure, and salinity of the water. The salinity in groundwater at Gardermoen may be disregarded in this connection; as it is generally low. The electrical conductivity is less than 1050 µS/cm for all wells, and corrections are normally not necessary for

conductivities lower than 2000 µS/cm (Appelo & Postma, 2005). To calculate the percentual saturation, taking the *in situ* temperature and pressure into account, the following formula has been used (Bøyum & Kaasa, 2001):

$$n\% = \frac{V \cdot 100 \cdot 760}{m \cdot p} \qquad \textit{Eq. 13}$$

Where V = concentration in ml/l as measured in the lab (c.f. section 3.2.4), m = temperature dependent 100% O_2 saturation in ml/l (table value in Bøyum & Kaasa, 2001) and p = air pressure in mmHg, as given in equation 14 below (Bøyum & Kaasa, 2001):

$$p = 760 - \frac{h}{10.6} \qquad \textit{Eq. 14}$$

where h = height given in m.a.s.l.

The percentual saturation of oxygen in the water samples, as plotted in figure 3.10, has been calculated with respect to the *in situ* temperature and height above sea level. Values are listed in appendix B5. Below 5% saturation, the uncertainty of analysis becomes high (as observed in multiple samples in the lab), and the water may simply be classified as anoxic.

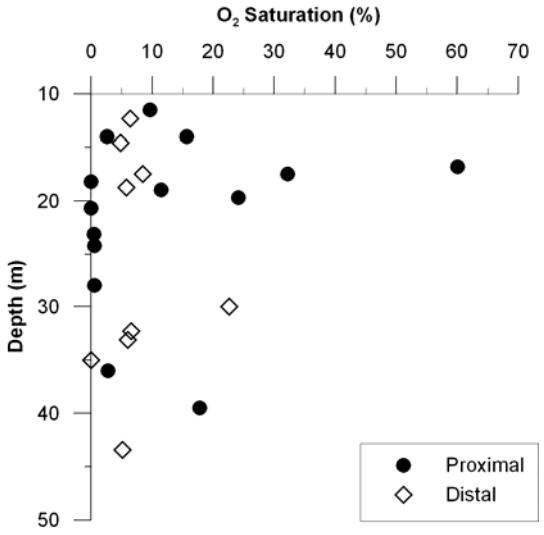

Figure 3.10: Plot of oxygen saturation versus depth, for all wells.

What seems to be the most prominent source of error is contact with the atmosphere while sampling. Especially wells with permanently installed pumps (FU1, K1, TW1 and TE1) that have a powerful, uncontrollable water jet are difficult to sample without atmospheric influence. The six BAT wells have not been analysed for oxygen because of the large amount of water needed for analysis relative to the volume of the sampling bottles and a bottle design (small opening) making atmospheric mixing hard to avoid.

Several factors influence the oxygen content of groundwater. The thickness of the unsaturated zone is one. If it is several meters, the travel time normally is long and O_2 may be resupplied by gas diffusion from the atmosphere while used in reactions with dissolved organic content (DOC). If such is the case, most DOC will be degraded within the unsaturated zone and the water feeding the groundwater will be oxic (Appelo & Postma, 2005). If the unsaturated zone is thin, however, most DOC will be transported down to the groundwater, as there is no time for degradation. Also important is soil permeability (*i.e.* porosity and fraction of water filled porosity), as it affects the efficiency of O_2 diffusion.

In figure 3.10 it is evident that groundwater from the deepest wells all have low oxygen content. The oxygen content in the saturated zone may be rapidly consumed if the groundwater enters sediments with reduced substances. The main oxygen consuming reaction in the aquifer, in addition to reduction of organic matter, is pyrite oxidation (c.f. section 2.4.4). The upper part of the aquifer is assumed to be free of pyrite (Jørgensen *et al.*, 1991; Basberg, 1999), but below this the oxygen consuming reduction of pyrite starts.

The plot (figure 3.10) was made with depths below surface in order to include wells K1 and FU1, from which head observations have not been made. A plot of depth below the groundwater table, however, displays the same trends which are described in the following. High oxygen saturation values are mostly in the upper part of the aquifer, and in the proximal part of the delta where the sediments are coarser (*i.e.* higher permeability) than in more distal parts. This might indicate that water infiltrating the aquifer is richer in oxygen in proximal parts due to more efficient diffusion, but in deeper parts >20 m below the surface all water seem to be almost anoxic. Clearly deviating from this trend is FU1 and TE1, which have relatively high saturations relative to depth. This is, however, thought to be caused by sampling difficulties (as described previously).

3.3.5 The Organic Fraction

All wells have been analysed by liquiTOC. A selection of 11 wells were analysed further with TLC-FID, and another three with GC-FID and GC-MS for organic fractions. In these analyses samples have been compared with the NSO-1 standard oil, which is a petroleum sample from the Oseberg field that is commonly used for compound identification and to calibrate laboratory instruments.

LiquiTOC

The results from the liquiTOC analysis seem to be unreliable, as the total inorganic carbon content (TIC) is less than measured alkalinity. When comparing calibrations before running the sample set and standards run afterwards, there seem to be a build-up of carbon within the instrument. The results might, however, be used semi-qualitatively as an indicator of relative concentrations, and are listed in appendix B7.

TLC-FID

Each sample was run two times with 9 µl of 250 µl concentrate and two times with 5 µl of 50 µl concentrate. From these the significant peaks were interpreted. The quantifications, listed in table 3.2, were made from the mean of the last two runs, as the accuracy of analysis increases with increasing concentration. The corresponding chromatograms are given in appendix C1.

Well	Saturated	Aromatic	Polar	Total
	micro g / l	micro g / l	micro g / l	micro g / l
RB1	14.04	0.00	218.25	232.29
RB2	9.25	0.00	18.05	27.30
RB3	7.06	0.00	15.23	22.29
TM6	4.36	0.00	53.48	57.84
TM7	2.84	0.00	45.10	47.94
TM8	9.22	0.00	78.58	87.80
TW1	10.56	0.00	19.08	29.64
TW2	2.27	0.00	24.31	26.58
TØ1	6.16	0.00	33.53	39.69
G20	1.83	0.00	26.48	28.31
K1	21.15	0.00	68.42	89.57

Table 3.2: Mean concentrations of the organic fractions in water samples. Analyses were performed using TLC/FID.

In all samples a larger polar fraction and a smaller saturated fraction were detected. No definite signals representing aromatic compounds were found. In figure 3.11 below typical peak configurations is displayed, compared to the NSO-1 standard oil.

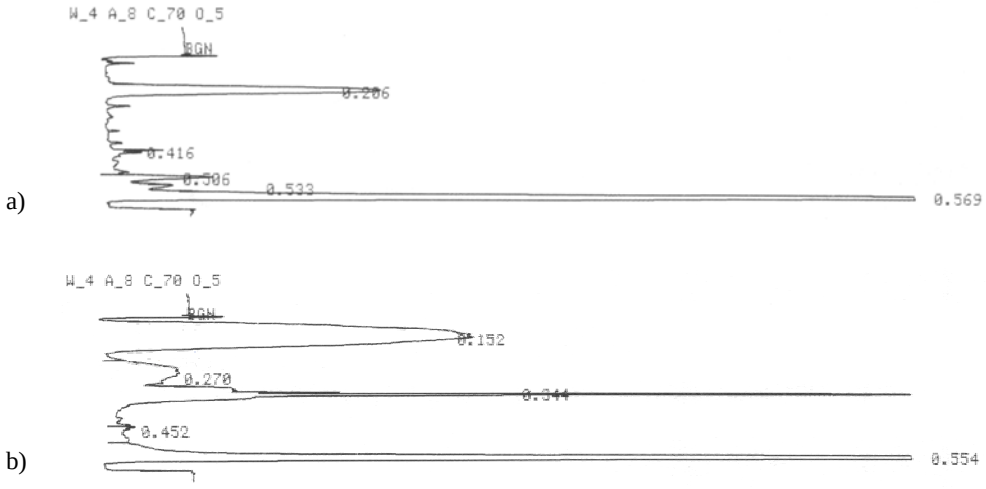

Figure 3.11: TLC-FID chromatograms. a) Sample TW1 (run 4.1). b) Standard NSO-1 (run 6.10). Retention times (no specific time unit) are listed on peaks.

Relative retention times, which have no specific time unit, are listed at each peak (figure 3.11), but should not be compared directly between samples as the integrator is started manually at every run. The first peak appearing is the saturated fraction, which was eluted using hexane and forms the upper band on the chromarod. Mono- and diaromatic compounds that are mobilized by toluene and form the middle band appear at retention times around 0.300, as seen in the standard sample (figure 3.11b)). Spikes and minor peaks are disregarded as noise along the base line, as they are found also when running the blanc sample. The last peak is the polar fraction; it is the largest and has the tripartite configuration seen in figure 3.11a) in all groundwater samples.

In general, the method offers high precision and accuracy for separation and quantification of hydrocarbons, presuming correct use (Karlsen & Larter, 1991). Several manual steps in the procedure require accurate performance. Here, with groundwater samples, large volumes of solvent (~100 ml DCM) with low concentration of extracted material are evaporated in several steps. When switching containers (four times), some substances might be lost due to adsorption. It is also uncertain whether the complete organic fraction has been extracted. The band widths of the eluted fractions are controlled mainly by the size of the applied spot, the

mass applied and the elution length (Karlsen & Larter, 1991). This source of error is, however, not systematic and is, if large, detected if two runs do not match. The temperature, which is a controlling factor for the vapour pressure inside the solvent containers, is thought to have been fairly constant during all runs.

GC-FID

Three samples containing a relatively large saturated fraction; RB1, TM8 and K1, were analysed and compared to a NSO-1 oil. The resulting chromatograms are displayed in figure 3.12 (note the different scale on the y-axes). Producing the most powerful signals is the RB1 sample. Larger copies of the individual chromatogram with higher vertical resolution are given in appendix C2 for a more detailed study of peaks.

The set of samples analysed with GC-FID are identical to those analysed with TLC-FID. As GC-FID is a highly automatic method, there are few sources of error following the sample preparation (discussed above). The instrument is normally used for high concentration petroleum samples, although thoroughly rinsed with solvent before sampling; there is still a slight possibility of contamination from previous samples. In some cases siloxanes from the Teflon cap in the sample bottles might contaminate samples.

In all three samples series, heavy n-alkanes are clearly recognisable, when comparing to the standard sample. Also common for all three samples is the large peak in between n-alkanes C25 – C26. Being identical in the samples, while not found in the standard, it is assumed that this is a contaminant in the solvent (DCM). The solvent has been concentrated more than a hundred times in the samples, explaining why it is not visible in the standard - although the NSO-1 oil was diluted slightly with DCM.

Several of the peaks in the samples all display tailing (rightwards drag at the base) compared to the very narrow, straight peaks in the standard oil. Tailing indicates presence of polar compounds in the sample, as the column in use is a non-polar column designed for saturated hydrocarbons in crude oils.

In the K1 sample definite matches are found for alkanes C19 – C33. For the heavier fractions noise exceeds the signal. The convex noisy baseline from ~35 – 60 minutes is an unresolved complex mixture (UCM); it is representing a complex mixture of organic components which

can not be chromatographically separated. This feature is characteristic for biodegraded petroleum, and is unrelated to column bleeding which will cause a similar effect, but the baseline will then continue the upwards trend due to increasing temperature (Peters *et al*., 2005). It is highly likely, based on relative retention times, that the single peak just before C19 is phenantrene, and that what appears to be a double peak (doublet) in between C19 and C20 is a quadruple peak representing the 3, 2, 9 and 1-methylphenantrenes.

In the RB1 sample, exact matches are found for alkanes C20 – C30. As it is displayed in figure 3.12, there is a distinct odd-even pattern. Alkanes having odd carbon numbers have higher peaks. Both odd and even peaks show, however, two convex peak height distributions, one higher (odd) and one lower (even). In between the n-alkanes are several other larger or smaller peaks. These are compounds with similar properties as nearby n-alkanes, as the retention times from the column are close and the peaks are well defined. Various iso-alkanes, cyclo-alkanes and alkylated aromatic hydrocarbons may form such peaks. In this sample it is more difficult to determine a definite peak of phenantrene as the peak height is relatively small compared to numerous peaks close by. Therefore it is only tentatively indicated (with P?) in figure 3.12. In the time-window indicative of methyl-phenatrenes, the signal is strong, but does not show the normal configuration. There seem to be several substances arriving at short intervals, making it difficult to identify potential methyl-phenantrenes, and it should be kept in mind that the concentrations of analyte is low.

In the final sample; TM8, alkanes from C22 – 35 (36 – 38) are recognised. The peaks are clearly separated, with insignificant signals from other components in between. Some column bleeding has occurred, causing the baseline to be somewhat elevated towards the end of the run. The specific peak between C18 and C19 is likely to be phenantrene, while the doublet-peak between C19 and C20, although not quite separated from a subsequent signal from an unknown component, may be interpreted as methyl-phenantrene isomers.

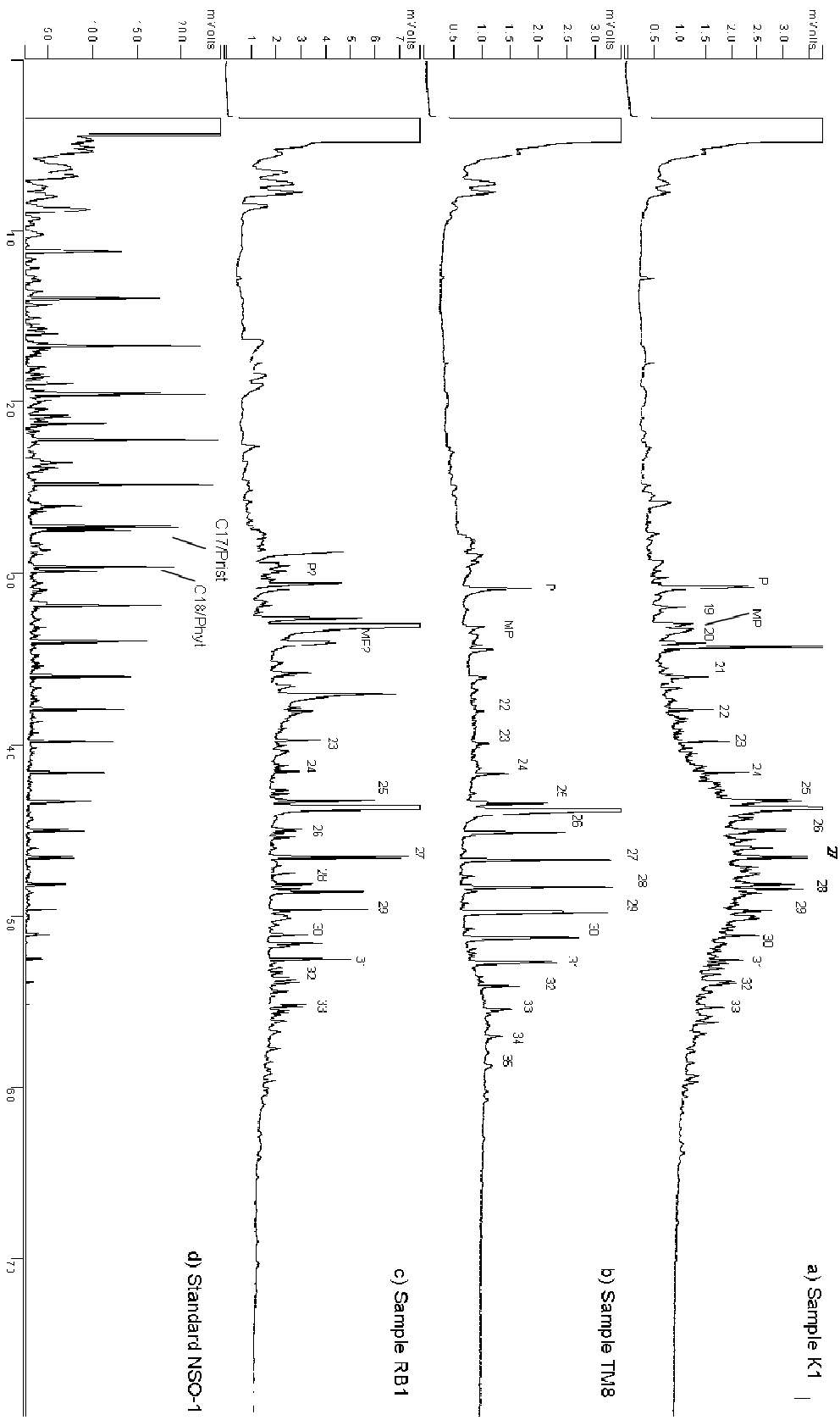

Figure 3.12: GC-FID chromatograms. a) K1, b) TM8, c) RB1 og d) standard NSO-1. P = phenantrenes, MP = methyl-phenantrenes.

GC-MS

Three samples were run; RB1, TM8 and K1 and compared with a standard NSO-1 oil. Using the existing MS-library and the NSO-1 standard, attempts to identify specific target compounds, with known m/z ratios, was performed. The same sources of error as discussed for GC-FID are also valid here, albeit the mass spectrometer acts as a mass selective detector, capable of detecting specific compounds in a complex, organic mixture.

TM8 and K1 turned out to have too low concentrations of individual compounds to make certain identifications of the PAH's (phenantrenes and methyl-phenantrenes) indicated in the GC-FID results, or any other unknown compounds. The n-alkane series observed in the GC-FID were, however, confirmed, although the samples turned out to be somewhat contaminated with siloxanes from the Teflon cap inside the sample-bottle. The GC-MS n-alkane series (also including RB1) are displayed in appendix C3.

In addition to the n-alkane series, positive identifications of petroleum-biomarkers were made in the RB1 sample (terpanes). A biomarker is defined as a chemical compound whose carbon skeleton is irrefutably derived from a functionalized identical skeleton in living organic matter (Peters *et al.,* 2005). In addition, biomarker derived compounds, such as phenantrenes and methyl-dibenzothiophenes, were detected. Well resolved signals of these more water soluble compounds were recorded, and matches were found for: phenantrene (178.08), the 3, 2, 9 and 1 isomeres of methyl-phenantrene (192.09) and 4, 3, 2 and 1 isomers of methyl-dibenzothiophenes (198.05). These compounds are displayed in sections of the chromatogram, and compared to standard in figures 3.13 and 3.14 below.

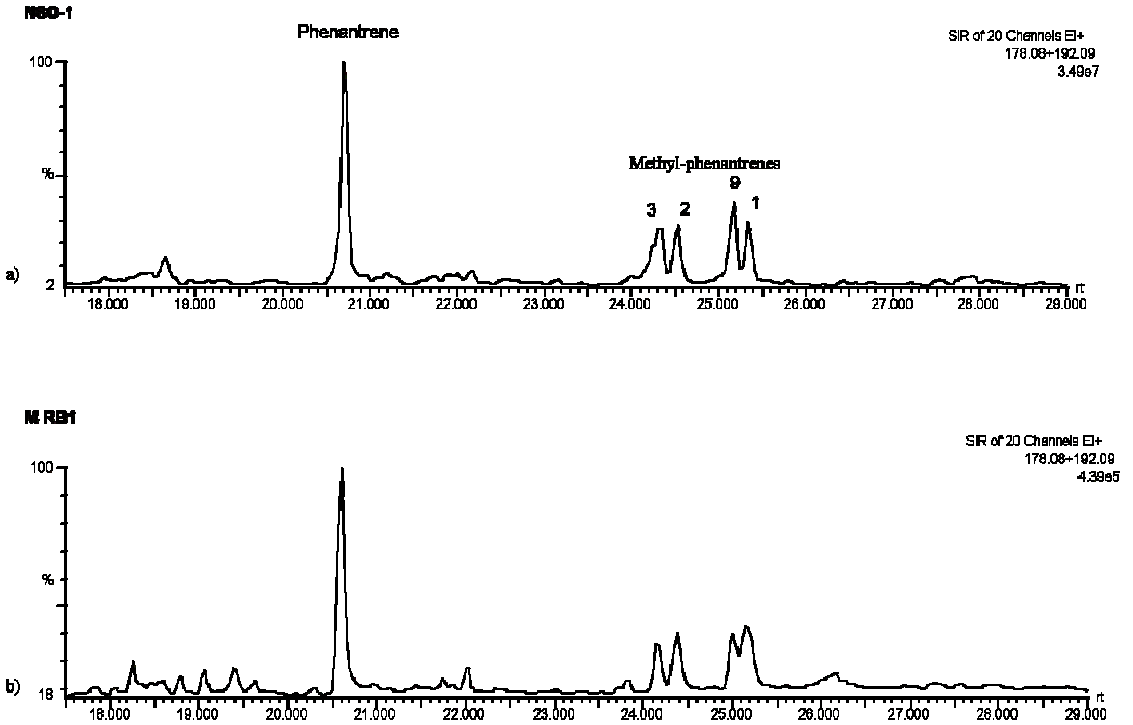

Figure 3.13: GC-MS chromatogram displaying phenantrene and 3, 2, 9, 1 methyl-phenantrenes. a) NSO-1 standard, b) sample RB1

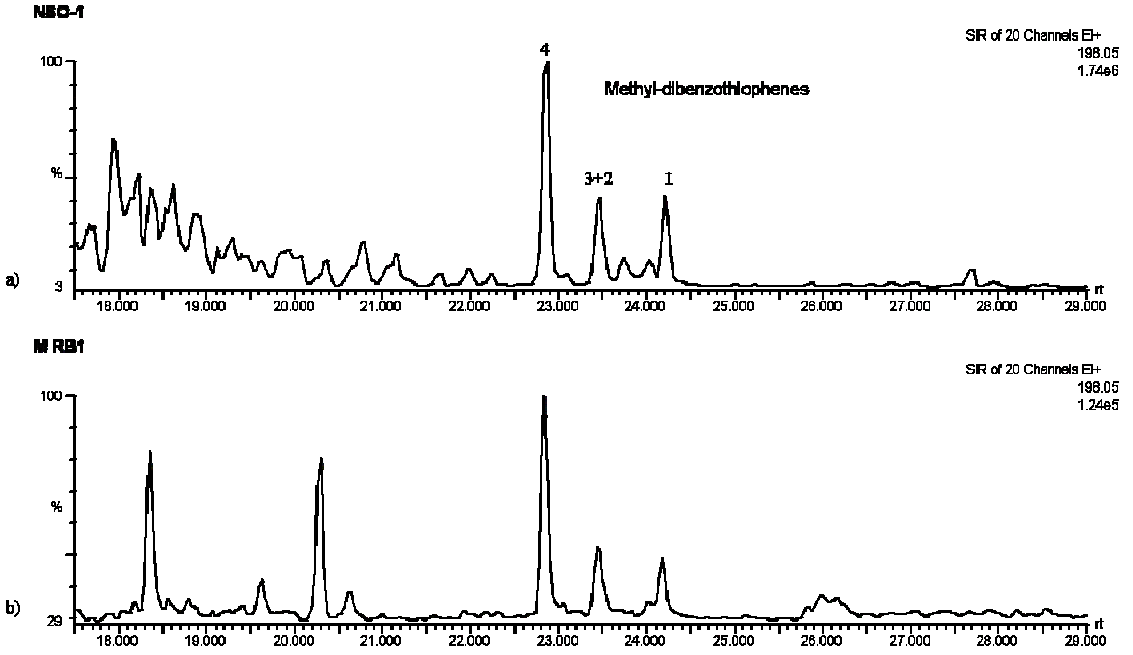

Figure 3.14: GC-MS chromatogram displaying the 4, 3+2, 1 isomers of methyl-dibenzothiophenes. a) NSO-1 standard, b) sample RB1

Also identified were tri-cyclic terpanes 23 and 24 and 30 hopane (penta-cyclic terpane), which all yield a 191.18 ion. In the chromatograms below (figure 3.15), it is evident that the configuration of these three compounds is different in sample RB1 and the standard. Based on this observation it may be established that the hydrocarbons in the two samples have different origins, eliminating any potential suspicion of cross contamination.

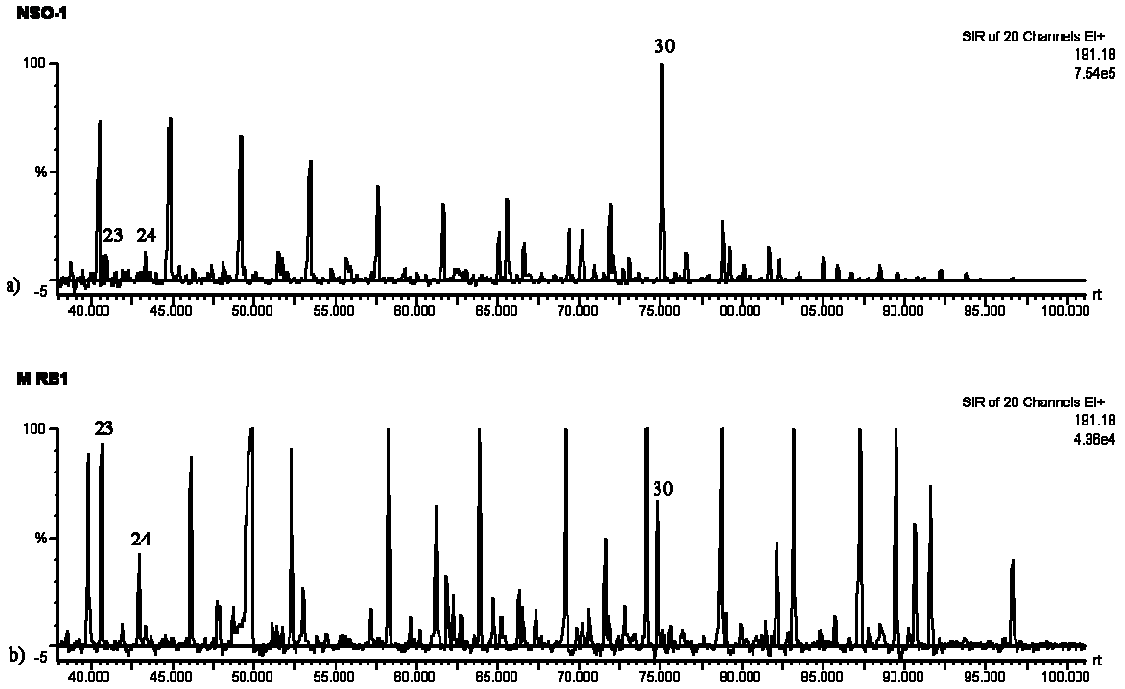

Figure 3.15: GC-MS chromatogram displaying the 23 and 24 isomers of therpanes and 30 hopane. a) NSO-1 standard, b) Sample RB1.

4. Geochemical Modelling

4.1 PHREEQC

The geochemical modelling in this study has been performed using PHREEQC version 2. The program is a tool for simulating chemical reactions and transport processes in natural or polluted water (Parkhurst & Appelo, 1999). It is based on equilibrium chemistry and contains a number of aqueous geochemical reaction models.

PHREEQC is based on the Fortran program PHREEQE (Parkhurst *et al.*, 1980). PHREEQE was capable of simulating a variety of geochemical reactions for a system including:

• Mixing of waters
• Addition of net irreversible reactions to solution
• Dissolving and precipitating phases to achieve equilibrium with the aqueous phase
• Effects of changing temperatures

Parkhurst (1995) developed a new program; PHREEQC version 1, written in the C programming language that comprised a number of new possibilities in addition to all the capabilities of PHREEQE. Among the improvements were:

• Ion-exchange equilibria
• Surface-complexation equilibria
• Fixed-pressure gas-phase equilibria
• Advective transport

PHREEQC version 2 is a modification of PHREEQC version 1. Most of the code and all of the capabilities are the same, but with a number of new ones added, including:

• Kinetically controlled reactions
• Solid-solution equilibria
• Fixed-volume gas-phase equilibria
• Variation of the number of exchange or surface sites in proportion to a mineral or kinetic reactant
• Diffusion or dispersion in 1D transport
• 1D transport coupled with diffusion into stagnant zones
• Isotope mole balance in inverse modelling

4.1.2 Inverse Modelling

The inverse modelling capability yields means for identifying the reactions along a flow-line accounting for observed water compositions between two points. A hypothesis, on which minerals and gases that are involved in geochemical reactions, is necessary, as the program seeks to balance concentrations of constituents in the water solutions relative to reactions involving a given set of phases. The program subsequently deciphers and quantifies the geochemical reactions causing a given solution 1 to develop into another given solution 2. The program may yield several solutions, one of which the user must determine is the most plausible.

4.2 Input Data

Several calculations have been made in the following section, based on one model setup, in which a mean rainwater composition (solution 1) (Heidenstrøm, 1999) is programmed to develop into the observed groundwater chemistry at a well-point (solution 2). An example of the input file is given in appendix D1.

Simulations were performed for 21 samples, based on the water chemistries presented in section 3.3. The Trandum wells were excluded as they may not be considered representative for natural weathering reactions because of the extensive anthropogenic input in the area (Sæther *et al.*, 1992; Basberg, 1998). For comparison one simulation was performed using the water composition in the river Risa (Otnes, 1973; 1975) as a final output.

The simulation is meant to quantify the dominating natural geochemical reactions occurring in the aquifer at Gardermoen (cf. section 2.4.4); calcite dissolution, pyrite oxidation, silicate weathering and leaching of fossil seawater. Therefore, only elements included in these reactions are given, which are: Cl^-, SO_4^{2-}, Na^+, K^+, Ca^{2+}, Mg^{2+}, Fe^{2+}, and also silicon, alkalinity and pH. The *in situ* temperature is also stated.

The possibly reacting phases and solid solutions in the model are chosen based on the mineralogy studies by Jørgensen *et al.* (1991) (cf. table 2.1). Dissolving phases are calcite, chlorite, K-feldspar, K-mica, pyrite and plagioclase. For calcite, chlorite and plagioclase solid solutions were specified according to Jørgensen *et al.* (1991) as; $Ca_{0.975}Mg_{0.025}CO_3$, $Mg_{2.15}Fe_{2.3}Al_{2.7}Si_{2.75}O_{10}(OH)_8$ and $Na_{0.7}Ca_{0.3}Al_{1.3}Si_{2.7}O_8$, respectively.

Precipitating phases are kaolinite and Ca-montmorillonite. These are secondary minerals which form during silicate weathering. At Gardermoen there are a variety of secondary clay minerals and amorphous phases (Teveldal *et al.*, 1990) and it is not an object of this study to determine in what relative amounts they form. Kaolinite and Ca-montmorillonite are chosen here to represent the secondary minerals, which balance the silicon and aluminium not entering the solution. Chalcedony is also inserted as a precipitating phase. It is not considered to be representative of the processes occurring, but is sometimes needed in the model in order to balance the silicon.

Pyrite oxidation will cause iron to precipitate if oxygen is available. In the model representing the entire flow-path; from precipitation input to output in the river Risa (appendix D1), $Fe(OH)_3$ is forced to precipitate, as expected in oxidised surface waters. In remaining models representing well-points within the aquifer, however, $Fe(OH)_3$ may precipitate or dissolve dependent on the program calculations (relative to iron concentrations in the solutions).

No restrains are put on the dissolving gases; CO_2 and O_2, in the solutions input. They exist solely as potential dissolving phases and are not limiting factors on the reactions, as they are abundant in the unsaturated zone.

Amphibole is not included as a phase, as the relative amount in the sediment is low (cf. table 2.1) and the complexity of the model increases with the number of phases. The relatively small contribution of Fe^{2+} and Mg^{2+} originating from the weathering of amphibole will be assigned to the dissolution of chlorite.

Leaching of fossil seawater is simulated by introducing halite as a dissolving phase, assuming the chloride- relative to sodium-content to be 1:1.

4.3 Results

Most runs generated more than one possible model for the geochemical reactions. In general, the largest differences between the models were in the dissolution of K-feldspar and K-mica, and the precipitation of kaolinite and Ca-montmorillonite. In table 4.1 below is an example of such multiple outputs with typical deviations.

Phases	Unit	Model 1	Model 2	Model 3	Model 4
Calcite	mol/l	5,58E-04	5,67E-04	5,50E-04	5,50E-04
Chlorite	mol/	3,54E-05	3,53E-05	3,55E-05	3,55E-05
K Feldsp.	mol/	-	3,60E-05	3,60E-06	-
K Mica	mol/	3,60E-05	-	-	3,60E-05
Pyrite	mol/	6,19E-05	6,19E-05	6,19E-05	6,19E-05
Halite	mol/	2,40E-05	2,40E-05	2,40E-05	2,40E-05
CO2	g	7,07E-04	6,98E-04	7,15E-04	7.150e-4
O2	g	2,52E-04	2,52E-04	2,52E-04	2,52E-04
Kaolinite	mol/	-1,40E-04	-4,14E-05	-1,60E-04	-1,96E-04
Plag.	mol/	1,44E-04	1,44E-04	1,44E-04	1,44E-04
Ca Mont.	mol/l	-4,76E-05	-1,01E-04	-	-
Fe(OH)	mol/	-1,43E-04	-1,43E-04	-1,43E-04	-1,43E-04
Chal.	mol/	-	-	-1,36E-04	-6,377E-05

Table 4.1: Four solution outputs generated in PHREEQC from water sample GW2. Model 1 has been selected as the most plausible. Negative numbers indicate precipitation, positive numbers indicate dissolution.

As it is displayed in table 4.1, which is a typical example of multiple outputs, results for calcite, chlorite, pyrite, halite, CO_2, O_2, plagioclase and Fe(OH) are close to identical. The choice of a plausible model is made based on the variations among the remaining phases. K-feldspar is in general considered to be slightly more weatherable than K-mica (Appelo & Postma, 2005) and is also present in the sediments in a larger amount (cf. table 2.1). However, it seems that it is a preferred weathering of mica at Gardermoen (Teveldal *et al.*, 1990). Therefore models preferring dissolution of K-mica over K-feldspar are chosen (models 1 and 4 in table 4.1). PHREEQC seems, however, to favour K-feldspar as the source of potassium, so when only one model is generated; K-feldspar is the only choice. A combination of the two phases is rare, and was only achieved with sample K1.

Which secondary mineral that precipitate; kaolinite or Ca-montmorillonite, is of minor significance to the final model, as the purpose here is only to balance the aluminium and silicon not entering the solution. Models including the precipitation of chalcedony are discarded if there are alternatives, as the phase is only included in order to even out imbalances in the silicon content. Based on these criteria, one model could be picked for all runs. Of the four models in table 4.1, model 1 was chosen to be the most plausible.

The modelling results are listed in appendix D2. Also given is the number of models generated, although only one has been chosen according to the above. When performing inverse modelling; changes in the solution compositions may not be made. Not all solution

compositions were possible to balance using default uncertainties (5%) and the given phase assemblage. This was the case for some solutions representing shallower wells, and was due to elevated values of specific elements; most often chloride. In order to generate a model still comparable to the other models, the uncertainty was increased only for the deviating ion. Where adjustments in uncertainties have been made, it has been listed in the results table (appendix D1).

5. Isotope Dating

5.1 Background Theory

Noble gas isotopes (*i.e.* He, Ne, Ar, Kr, Xe) are suitable as environmental tracers in water systems, since they are chemically inert under natural conditions (Beyerle *et al*., 2000). The accumulation of these isotopes in groundwater, caused by radiogenic production, yields means for estimating groundwater residence times. In this study the $^3H/^3He$ dating method has been used, in which the amount of the hydrogen isotope tritium (^3H) is compared to the amount of its decay product; tritiogenic helium (^3He).

5.1.1 Cosmogenic Tritium

Tritium (^3_1H) is a radioactive super-heavy isotope of hydrogen. It is produced naturally in the upper atmosphere through the interaction of cosmic ray neutrons, *n*, with nitrogen, as in the following reaction (Faure & Mensing, 2005):

$$^{14}_{7}N + ^{1}_{0}n \rightarrow ^{3}_{1}H + ^{12}_{6}C \qquad \textit{Eq. 5.1}$$

This nuclear reaction produces tritium at a rate of 0.5 ± 0.3 atoms of H^3/cm^2 (Craig & Lal, 1961). The neutrons involved are produced by nuclear reactions induced by high energy protons and other nuclear particles of cosmic rays (Faure & Mensing, 2005). Some tritium may also be derived directly from the sun, by means of solar winds (Craig, 1957).

Tritium is incorporated in water molecules through direct oxidation or by exchange with stable hydrogen isotopes (^1_1H and ^2_1H) (Faure & Mensing, 2005). It subsequently enters the hydrosphere in the form of $^1H^3HO$.

Tritium decays to the stable helium isotope ^3_2He by β-emission (Faure & Mensing, 2005):

$$^{3}_{1}H \rightarrow ^{3}_{2}He + \beta^{-} + v + 0.01861MeV \qquad \textit{Eq. 5.2}$$

where β^- is the β-particle and *v* is the complementary anti-neutrino. Given in million electron volts; *MeV*, is the total decay energy.

The half-life of this decay is $T_{1/2} = 12.38\ y$ (Oliver *et al*., 1987), with the corresponding decay constant being $\lambda = ln\ (2) / T_{1/2} = 0.05599\ y^{-1}$. The concentrations of tritium are most commonly expressed in Tritium Units (TU) (Fontes, 1985):

$$1\ TU = 1\ ^{3}H\ atom\ per\ 10^{18}\ hydrogen\ atoms$$

or in activities (Clark & Fritz, 1997), where;

$$1\ TU = 0.118\ Bq \cdot kg^{-1}\ (3.19\ pCi \cdot kg^{-1})\ in\ water$$

The relationship between TU and cm^3STP/g is (Faure & Mensing, 2005):

$$1 cm^3 STP / g_{water} = \frac{4.0193 \cdot 10^{14}}{(1 - S/1000)} \cdot TU \qquad Eq.\ 5.3$$

where S = salinity of water given in ‰.

The amount of tritium generated naturally in the atmosphere yields a tritium concentration in precipitation of less than 20 TU (Fontes, 1980).

5.1.2 Thermonuclear Tritium

Prior to 1952 there were low and natural levels of tritium in precipitation. From 1952 to 1963, however, large amounts of tritium were released from thermonuclear atmospheric experiments. This anthropogenic input soon entered the natural cycle of tritium in the hydrosphere. Large amounts of tritium would also accumulate to form a stratospheric reservoir, further contaminating global precipitation (Clark & Fritz, 1997).

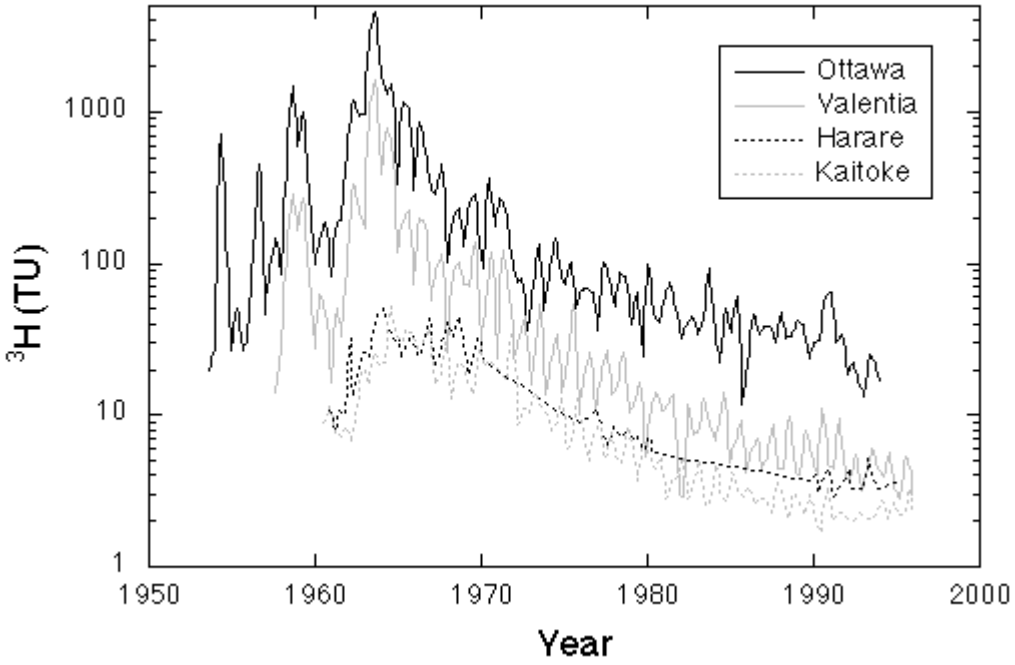

Figure 5.1: Tritium concentration in precipitation since 1950 at four IAEA stations (IAEA/WMO, 2006): Ottawa, Canada (northern hemisphere, conti-nental); Valentia, Ireland (northern hemisphere, marine); Harare, Zimbabwe (southern hemisphere, continental); Kaitoke, New Zealand (southern hemisphere, marine).

When the nuclear testing began, there was a marked jump in concentrations of tritium in precipitation, which kept increasing until a Sovjet-American treaty in 1962 banned further thermonuclear testing. The absolute peak in tritium concentrations appeared in 1963 (figure 5.1), an event which is now used as a hydrogeological marker. From this time point there was a steady decrease, despite the continuation of minor French and Chinese testing until 1980.

In addition to the tritium derived naturally and so called bomb-tritium, there are minor present contributions from nuclear power plants, nuclear fuel reprocessing facilities, preparation of material for nuclear weapons and by the manufacturers of tritiated paints and gases (Clark & Fritz, 1997).

The activity of tritium in precipitation display both geographical and diurnal variations. Globally the activity increases towards middle and high latitudes (figure 5.1), as the transfer of tritium from the stratosphere to the troposphere is greatest in the Polar Regions due to the cooling and subsequent sinking of air-masses (Dincer & Davis, 1967). Seasonal changes also influence these air circulation patterns, causing a spring peak in the tritium concentration in the order of three times the weighted annual mean (Clark & Fritz, 1997; Gat, 1980). Further;

continental precipitation is enriched with respect to tritium relative to coastal rain. This is related to the transit time of wet air masses during which ongoing mixing with tritiated vapour and molecular exchange with the water surface occurs (Haldorsen *et al*., 1997). Additionally concentrations are higher in the northern-, compared to the southern-, hemisphere (figure 5.1) simply due to the geographical distribution of nuclear test sites (Dincer & Davis, 1967).

The ongoing decline in tritium concentrations, as seen in figure 5.1, is not only due to radioactive decay, which only decreases total concentrations by 5.5 % per year. A major sink for thermonuclear tritium are groundwaters and oceans (Clark & Fritz, 1997).

5.1.3 Sources of Helium in Groundwater

Helium isotopes in groundwater have several origins. Radiogenic ^{4}He, which is equivalent to an α-particle, forms during decay of U/Th series elements. Nucleogenic ^{3}He is the daughter product during decay of ^{3}H, which is formed primarily by fission of ^{6}Li in the lithosphere due to neutrons produced during decay of U/Th series elements (Solomon *et al*., 1992). The amount of ^{3}He and ^{4}He formed through alpha decay is dependent on the age of rocks, concentrations of U and Th and the amount of ^{6}Li and other neutron capturing elements (Solomon *et al*., 1992).

Atmospheric helium equilibrates with rainwater which subsequently enters groundwater systems having the same ratio of ^{3}He and ^{4}He as the atmosphere. When determining $^3He_{tritiogenic}$ for groundwater dating it is commonly assumed that the initial content of ^{3}He is exclusively atmospheric. Using the relationship; $^3He/^4He = 1.4 \cdot 10^{-6}$ for the atmosphere (Faure & Mensing, 2005), initial ^{3}He may be determined from the measured concentration of helium in the sample simply as;

$$^3He_{tritiogenic} = {}^3He_{measured} - {}^3He_{initial} \qquad \textit{Eq. 5.4}$$

The measured ^{3}He must, however, be corrected for the 'excess air phenomenon' which is described in section 5.2.

In summary; the different components of helium in groundwater may be described as follows (Beyerle *et al*., 2000):

$$^3He_{tot} = {}^3He_{atm} + {}^3He_{tri} + {}^3He_{nuc} \qquad \textit{Eq. 5.5}$$

$$^4He_{tot} = {}^4He_{atm} + {}^4He_{rad} \qquad \textit{Eq. 5.6}$$

Where *tot* = total amount of dissolved helium, *atm* = atmospherically derived, *tri* = tritiogenic, *nuc* = nucleogenic and *rad* = radiogenic.

5.1.4 Dating Groundwater

The relation between the radioactive isotope ^{3}H and its decay product ^{3}He forms a timescale, independent of the variations of tritium input. Water in contact with the atmosphere is continuously exchanging tritiogenic ^{3}He (*i.e.* ^{3}He derived from ^{3}H decay) with the surrounding air. When a parcel of water is separated from the atmosphere, by infiltrating to groundwater or sinking into oceans, tritiogenic ^{3}He will start to accumulate. The water mass age, τ , expresses the duration of isolation from the atmosphere (Ekwurzel *et al*., 1994):

$$\tau = \frac{1}{\lambda} \cdot \ln\left(1 + \frac{^3He_{tritiogenic}}{^3H}\right) \qquad \textit{Eq. 5.7}$$

Where λ = ^{3}H decay constant and $^3He_{tritiogenic}$ and ^{3}H are concentrations given in TU.
The above relationship is a measure of groundwater age as long as helium does not escape the aquifer and there is no subsurface production of tritium (*e.g.* from Li in the rock matrix). It is also assumed that the groundwater flow is mainly horizontal without vertical mixing of waters of different ages (Faure & Mensing, 2005; Haldorsen *et al*., 1997).

The ^{3}H/^{3}He method is most suitable for determining groundwater ages in the range of 0 to 30 years. Within this interval analytical uncertainty is typically less than 10% (Solomon *et al*., 1993). Concentrations of ^{3}H and ^{3}He are extremely low and difficult to measure. In this study it has been done by means of noble gas mass spectrometry, which is discussed further in section 5.3. From the water mass age groundwater flow velocities (*i.e.* age versus distance), recharge rates (*i.e.* vertical age gradient), and mixing ratios may be determined.

5.2 Sampling Procedure

When sampling groundwater for $^{3}H/^{3}He$ analysis, the main concern is to avoid gas exchange with the atmosphere during sampling, transport and storage. Air is the major contaminant. Groundwater is commonly supersaturated with respect to helium and other atmospheric gases. This is partly caused by a phenomenon known as 'excess air' which is not yet fully understood. Entrapment of air under a transient wetting front in the vadose zone is assumed to be the main reason (Solomon *et al*., 1993). Inadequate sampling procedures may also cause supersaturation. By measuring the content of other noble gases (*e.g.* neon, which has no other significant subsurface source) in excess of solubility and atmospheric ratio (*e.g.* He/Ne), it is possible to estimate the contribution of helium due to supersaturation (Beyerle *et al*., 1999). Since the solubilities of atmospheric gases are known functions of temperature, it is possible to determine the recharge temperature of the groundwater (Stute & Schlosser, 1993; Aeschbach-Hertig *et al*., 1999).

In order to avoid degassing from the samples of gases produced below the surface (*e.g.* CO_2, CH_4, He), it is important to maintain pressure while sampling (Beyerle *et al*., 2000). A submersible pump which is used in this study should provide sufficient pressure. A minimum of three well volumes was pumped before sampling.

Figure 5.2: Sampling groundwater for isotope analysis at Gardermoen, 2006.

Groundwater pumped from the well was lead, via a flexible plastic tube, through a copper tube clamped in an aluminium frame (fig. 5.2). To avoid air bubbles from forming or being

captured within the tube, the water was allowed to flow through for some time while knocking on the frame. The copper tube holding the water sample was then pinched off in both ends by tightening the frame before disconnecting the water hose. In order to sustain pressure, the upper end (fig. 5.2) was sealed off first.

In the sealed containers the water samples may be stored without significant loss or gain. For helium, which is the most mobile gas, the maximum leakage rate to vacuum is less than 10^{-9} cm^3 STP y^{-1} (Kipfer, 1991; Aeschbach-Hertig, 1994; Beyerle *et al*., 2000).

5.3 Method of Analysis

Tritium concentrations are measured indirectly by determining the amount of its decay product; tritiogenic helium, using mass spectrometry. There are only a few noble gas mass spectrometry labs in the world being capable of determining such low concentrations. This sample set was dated at the Swiss Federal Institute of Environmental Science and Technology (Eawag). A thorough description of the individual components in figure 5.3 and the method of analysis are given by Beyerle *et al*. (2000), upon which the following short version is based.

5.3.1 Gas Extraction

In order to extract noble gases from a water sample, the sampling container is connected to an ultra high vacuum (UHV) extraction vessel and line. The entire setup with extraction and purification lines, connected to two mass spectrometers (MS), is displayed in figure 5.3.

A combination of several different pumps in series (figure 5.3) is needed to remove water vapour and generate UHV in the extraction vessel. When the pressure is reduced to circa 10^{-7} mbar, which is considered UHV, the extraction vessel is sealed off from the line, and the sample container opened. The reason for using pure copper tubes is that the soft metal ensures that the sample container may be reopened without breaking.

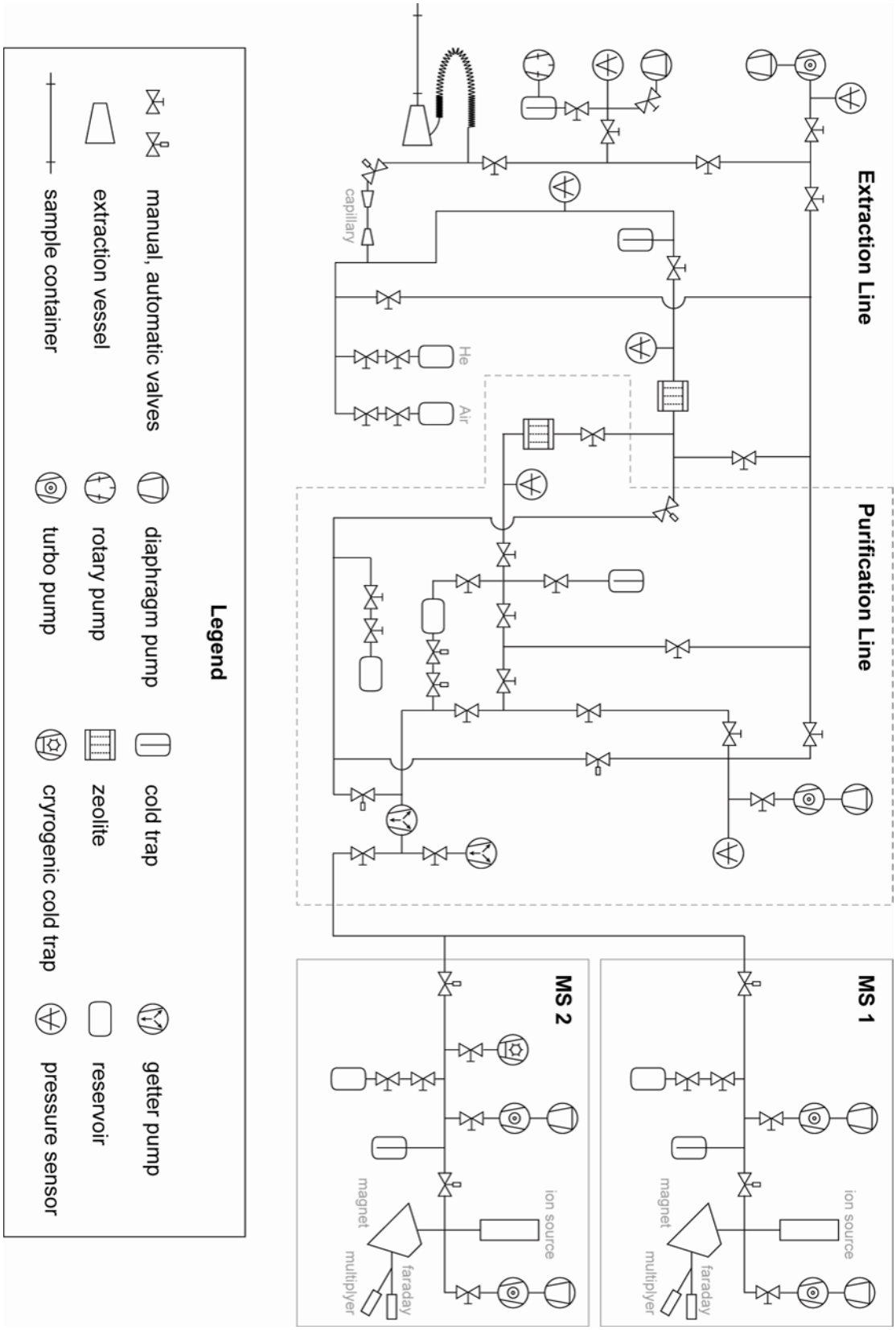

Figure 5.3: Diagram of extraction line, purification line and the two mass spectrometers (modified from Beyerle *et al.*, 2000).

The extraction vessel is shaken mechanically in order to enhance the removal of gases from the water phase. The flow of water vapour and gases is induced by pressure differences and controlled by a capillary (figure 5.3) preventing back diffusion of non-condensable gases (*e.g.* He). Water vapour and gases are adsorbed onto traps of metal or zeolite (figure 5.3), which are cooled by liquid nitrogen.

The process of gas extraction takes about five minutes and is terminated by closing the valve before the capillary (figure 5.3). The extraction efficiency for He is more than 99.995% (Aeschbach-Hertig, 1994).

5.3.2 Helium Measurement

The light, non condensable gases He and Ne stay in the gas phase while other condensable gases adsorb to the traps. When the extraction line is connected to the purification line, the remaining active gases are caught in getter pumps (figure 5.3).

During the first step of the separation process one fourth of the gas phase is transferred into an all-metal, statically operated 90^o magnetic sector spectrometer (MS1 in figure 5.3), where ^4He, ^{20}Ne and ^{22}Ne are detected and measured by use of a Faraday cup. In the second step the remaining gas is let into a second 90^o sector mass spectrometer (MS2), with a double collector system. Here ^4He and ^3He are measured simultaneously, while Ne is adsorbed to a cryogenic cold trap. ^4He is measured by a Faraday cup, while ^3He is determined by counting the $^3He^+$ ion beam with an electron multiplier. The counting error is in the order of 0.3%. The system sensitivity allows for measurements down to 10^{-15} cm^3STP for ^3He.

5.3.3 Tritium Measurement

Tritium is measured indirectly by helium ingrowth. Therefore the degassed water sample is transferred back into the copper tube after the noble gas analysis and sealed. After approximately three months ^3He is measured again, and the ^3H content may be determined based on the known decay rates. The detection limit for tritium in a standard water sample (45 g) is about 1 TU.

5.4 Previous Results

In 1999 T. Torgersen and P. Aagaard sampled nine wells at Gardermoen and sent them to the Eawag laboratory in Switzerland, where analyses were performed by W. Aeschbach-Hertig. The unpublished results are displayed in table 5.1 below, while further details on well data and concentrations of tritium and helium are listed in appendix E.

Sample NO	Well Name	Place	Screen A.	GW depth	Tritium	Age	Error
			m	m	TU	y	y
1	agri sch (FU1)	Furusmo	30,00	8,00	18,14	17,64	0,31
1	duplicate	Furusmo	30,00	8,00	17,42	22,44	0,51
2	G20 (GW2)	Gardermoen, West	35,22	4,20	11,72	4,37	0,47
3	NGU62_c (TM2)	Trandum Military Camp	20,70	17,00	24,95	3,75	0,23
3	NGU62_b (TM3)	Trandum Military Camp	24,20	17,00	51,98	3,31	0,12
4	NGU B3B (TM1)	Trandum Military Camp	23,12	14,00	19,13	5,61	0,47
5	NGU61_c (TM6)	Trandum Military Camp	17,50	9,50	14,50	6,45	0,45
6	G14	Moreppen	5,50	4,50	13,74	0,50	0,49
7	G10	Moreppen	5,50	4,50	13,77	-0,11	0,53
8	NGU43 (TW2)	Lake Transjøen, West	16,80	13,80	8,43	4,57	0,71
9	NGU21	Trandum Military Camp	29,75	26,00	52,25	0,27	0,09

Table 5.1: Unpublished results of isotope dating of groundwater samples from Gardermoen, performed by W. Aeschbach-Hertig, T. Torgersen and P. Aagaard.

The tritium values vary from 8 – 52 TU, and the apparent age from 0 – 22 years. Some of the high tritium samples turned out to be quite young, which might indicate tritium contamination (pers. comm. W. Aeschbach-Hertig, 2006). Samples 1 and 9 were additionally analysed for heavy noble gases, which made it possible to calculate recharge temperatures of 4.26 and 5.63^{o}C, respectively. In these samples there was no indication of excess air fractionation, which simplified further calculations of $^{3}H/^{3}He$ ages. In the remaining samples; 2 – 8, the *in situ* temperature was used when calculating gas solubility in infiltrating water, which is a source of error. Some of these temperatures are somewhat higher than what was calculated for samples 1 and 9, which yield lower solubility of atmospheric gases in the recharge. The calculated error of analysis varies from approximately 0.10 – 0.70 years and displays a linear relationship with the content of tritium; indicating that the accuracy of analysis increases with increasing isotope content.

There is a clear tendency in the dataset of water-age increasing with depth. From figure 5.3 it seems, however, that the age is more correlated with depth below groundwater than with total depth. This is due to the various extent of the unsaturated zone, and that contact with atmospheric gases is not accommodated until infiltrating water reaches the groundwater.

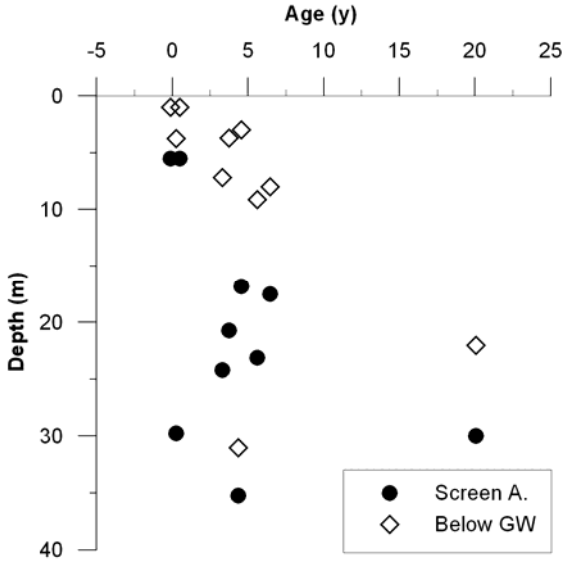

Figure 5.3: Plot of calculated water-age versus depth below the groundwater table and depth below surface.

In the above plot sample 2 is clearly deviating from the trend in the series plotted as depth below groundwater, which otherwise display a linear fit of the data points (figure 5.3). It seems probable the sample may not be representative. A possible explanation would be that groundwater *in situ* has been mixed with younger water through leakage in the well-case.

5.5 Preliminary New Results

During this study ten wells (K1, TM1, RB1 – 3, GE1, GE4 – 5, GW1 AND FU1) were sampled and sent to M. Brennwald at the Eawag laboratory for isotope analyses. At present the final results are not yet ready. Four samples; FU1, RB1, RB2 and K1, have, however, been analysed for noble gases (He, Ne, Ar, Kr and Xe), from which it is possible to make preliminary assumptions on relative ages. The results are listed in appendix E. The exact sample weights can not be determined until the analyses are completed (the sample containers are currently stored until the second run). The concentrations are therefore calculated using an arbitrary sample weight of 45.0 g, assuming an uncertainty of about 1 g, *i.e.* sample weights are commonly in the range of 44.0 – 46.0 g. The isotope ratios are unaffected by the uncertainty in the weights (pers. comm. M. Brennwald). In addition, there are some analytical uncertainties concerning gas extraction, processing and MS analysis. The analytical error estimated at the Eawag-lab is listed in appendix E.

The ^{3}He-^{4}He ratios presented below (table 5.2) are not calculated from the final evaluation of the MS data (after enrichment of ^{3}He in the samples), but derived from a manual evaluation done at the lab during the analyses. These evaluations are normally close to the final data; within 1% (pers. comm. M. Brennwald, 2006).

Sample	$^{3}He/^{4}He$	He Conc.	He Equil.	Rel. Supers.
		ccSTP/g	ccSTP/g	%
FU1	1,17E-06	7,88E-08	4,75E-08	66,0%
RB1	2,56E-06	7,27E-08	4,66E-08	56,0%
RB2	1,52E-06	7,00E-08	4,66E-08	50,2%
K1	1,20E-06	1,24E-07	4,71E-08	162,5%

Table 5.2: Results from noble gas analyses at Eawag for He concentrations. Where conc. = concentration, equil. = equilibrium concentration at given (*in situ* temperature), rel. supers. = relative supersaturation.

All samples display supersaturation with respect to equilibrium concentrations of the atmospheric noble gases, as is common in groundwaters due to the excess air phenomenon. The saturation levels have been calculated based upon the temperatures measured *in situ*. The He concentration in particular is high for all samples, especially in K1, indicating accumulation of terrigenic ^{4}He.

The $^{3}He/^{4}He$ ratios of FU1 and K1 are lower than for air-saturated water ($^{3}He/^{4}He$ = 1.36E-6), which also indicates the presence of a significant amount of terrigenic ^{4}He in excess. Based on these low $^{3}He/^{4}He$ ratios it seems that FU1 and K1 infiltrated before the Tritium-Peak in the 1960s, possibly much earlier (pers. comm. M. Brennwald, 2006). Having the largest amount of terrigenic ^{4}He in excess, K1 seems to be the 'oldest' of these four samples.

The $^{3}He/^{4}He$ ratios of RB1 and RB2 are higher than that of air-saturated water ($^{3}He/^{4}He$ = 1.36E-6), which indicates the presence of tritiogenic ^{3}He. RB1 and RB2 also show lower ^{4}He excess. RB1 in particular has a high $^{3}He/^{4}He$ ratio, which suggests that a large amount of tritium has decayed to ^{3}He. Infiltration during the 1960 – 70s is likely to be the cause of such high levels (pers. comm. M. Brennwald, 2006). Because of the lower $^{3}He/^{4}He$ ratio RB2 is probably younger than RB1.

6. Groundwater Flow

6.1 Theory

Groundwater may flow through a variety of different materials. The speed and nature of flow is mainly dependent on the properties of the medium and the potential energy of water. For most granular materials Darcy's law (eq. 6.1) is valid for describing groundwater flow towards lower potential (Domenico & Schwartz, 1997).

$$\frac{Q}{A} = q = -K\frac{\partial h}{\partial x} \qquad \textit{Eq. 6.1}$$

Where Q = volumetric flow rate (m^3/s), A = area (m^2), q = specific discharge (m/s), K = hydraulic conductivity (m/s), h = hydraulic head (m) and x = flow length (m). $\partial h / \partial x$ is the hydraulic gradient.

Darcy's law defines a linear relationship between the specific discharge and the hydraulic gradient. As long as the flow is laminar, which is the case for most groundwaters, the expression is valid. In nature, however, the area of through-flow is less, as the water only moves through connected pore spaces. An expression of the true velocity is given as follows (Domenico & Schwartz, 1997);

$$\frac{Q}{n_e A} = \frac{q}{n_e} = v = -\left(\frac{K}{n_e}\right)\frac{\partial h}{hx} \qquad \textit{Eq. 6.2}$$

Where n_e = effective porosity and v = linear velocity (m/s).

Bernoulli's equation states that, under conditions of steady state flow the total energy of an incompressible fluid is constant at all positions along a flow path in a closed system (Domenico & Schwartz, 1997). It is given as follows:

$$gz + \frac{P}{\rho_w} + \frac{v^2}{2} = const. \qquad \textit{Eq. 6.3}$$

Where g = acceleration due to gravity, z = elevation, P = pressure by water column, ρ_w = fluid density and v = velocity.

In the case of groundwater flow, which has a very low velocity, the kinetic term may be discarded. A simplified expression of the total head; h, as a sum of elevation head and pressure head is given by (Domenico & Schwartz, 1997);

$$h = z + \frac{P}{\rho_w g} \qquad \textit{Eq. 6.4}$$

In aquifers flow is three dimensional in the x, y and z directions. As natural media rarely are homogenous, hydraulic conductivity and hydraulic gradient needs to be defined for three directions. Correspondingly, specific flux may vary with direction of flow. Groundwater flow models solve a set of differential equations describing the flow in all directions. The equations are solved for each cell through matrix calculations. In transient simulations (not discussed or used here) and natural systems groundwater flow would also change with time, and the specific storage of the aquifer would have to be included. Only the main principles of groundwater flow have been presented here. For derivation of 3D and transient flow equations, consult Domenico & Schwartz (1997).

6.2 Groundwater Flow Patterns at Gardermoen

The general hydrogeology at Gardermoen was presented in section 2.4. Østmo (1976) made a thorough map of the hydraulic head distribution at Gardermoen. This has, however, been slightly changed since the Gardermoen airport became operative.

6.1.1 Existing Models

Several models simulating groundwater flow at Gardermoen have been made. The first 2D model was made for a distal section of the Trandum delta by Sønsterudbråten (1994). Later Wong (1996) and Butt (1997) made 2D models of flow in the Trandum Delta, based on the cross section mapped by Tuttle (1997) (figures 2.5 and 2.8). Below is an image of modelling results produced by Wong (1996).

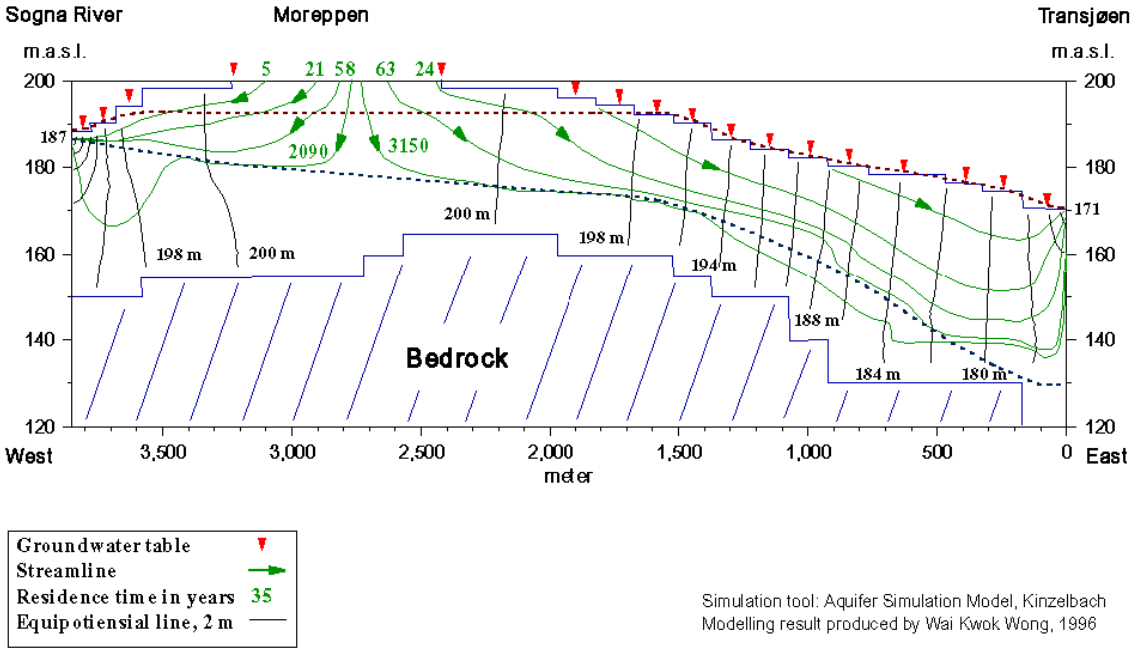

Figure 6.1: Numerical modelling of groundwater flow across the Gardermoen delta. The modeling result is produced by Wong (1996).

The cross section on which the above model is based extends from the paleo melt water portal at Lake Transjøen and out to the ravines in the west, but not along a straight line (cf. appendix A1, profile 1). A three dimensional flow model of the Trandum Delta has been developed at OSL using Visual MODFLOW, and is further described in section 6.3. Below a simulation of flow-paths have been made for a corresponding cross section (appendix A1, profile 2), for comparison.

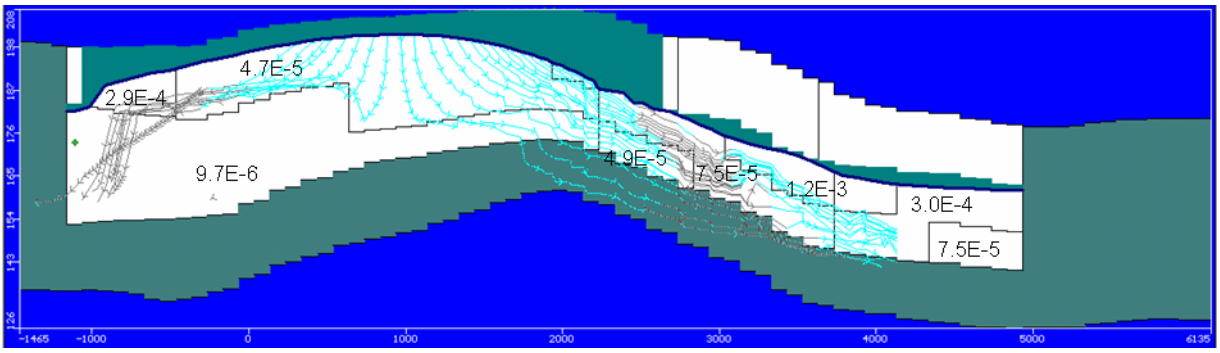

Figure 6.2: Cross section from Lake Transjøen and out to the ravines. The result has been generated using the OSL 3D model (Helberg, 2000; Wejden, 2005). Pathlines: aqua colour indicates movement inwards in the plane of view, grey colour indicates outwards movement. Between each arrowhead is a travel time of two years. Different conductivities given in m/s are separated with black lines.

The general flow pattern in the 2D model (figure 6.1) and the 3D model (figure 6.2) is similar, with a division of flow (groundwater divide) where the total head is highest, and decreasing flow velocities with depth. The outflow solutions in the two models seem to produce slightly different results. The head observations made in this study have been plotted and compared with simulations in the OSL 3D model. In a 2D model the planar or xy dimension of groundwater flow would be lost. As it is illustrated in figure 6.3, there seem to be also a northwards component to the flow of water from the line-surface of the cross- section. If the observations of this study were to be compared to a 2D model, they would have to be projected onto the cross section, as they are distributed across a large area on the delta plain. This could be done using radial projection of the individual wells onto the cross section, based on an assumption of radial delta symmetry cf. Kitterød (2004).

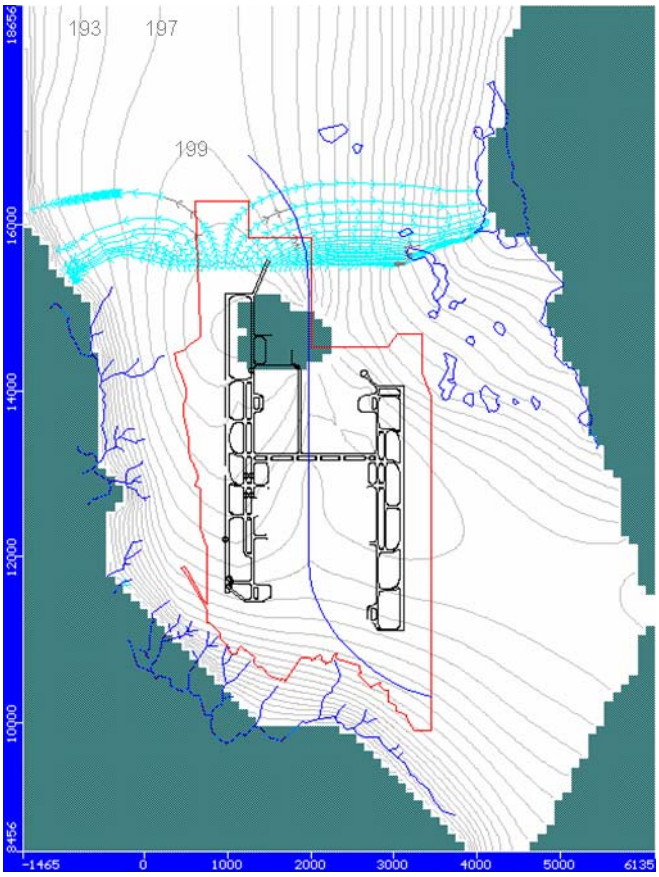

Figure 6.3: Flow of water (particles) from the surface. The result has been generated using the OSL 3D model (Helberg, 2000; Wejden, 2005). Pathlines: aqua colour indicates movement inwards in the plane of view (downwards), grey colour indicates outwards movement (upwards). Between each arrowhead is a travel time of two years. Head equipotentials are given with 2m intervals.

6.3 The OSL Groundwater Flow Model

A model simulating groundwater flow was developed at OSL by D. Helberg (2000), taking the changes in the water balance induced by the building and running of the airport into account. This model was generated using the software Visual MODFLOW version 4.0. In 2005 B. Wejden started a revision of the OSL groundwater model, to implement observations of hydraulic heads and other data from the seven years the airport has been operative. The model is still being developed and further refinements are planned.

6.3.1 Visual MODFLOW

The software package Visual MODFLOW professional (VM) version 4.0 was developed by Waterloo Hydrogeologic, which is now a Schlumberger company, and has been available on the market since 1994. During following years it has been subject to numerous revisions. VM integrates the use of the MODFLOW, MODPATH and MT3D packages.

In MODFLOW the groundwater flow equations are solved for three dimensions using finite difference approximation. The modelled domain is divided into cells by planar perpendicular lines that may have variable spacing. Further, the model may have several layers of varying thickness. The hydraulic head is calculated in the centre of the cell. A flow equation is solved for each cell, which individually has homogenous properties. The resulting matrix may be solved with different solvers (the PCG solver is used here) adapted to the type of problem to be solved, for both steady state and transient flow.

MODPATH simulates the movement of water particles. Particle tracking is a useful tool which estimates both flow velocities and directions, based on the calculations performed in MODFLOW. The simulation is done by tracking particles forwards or backwards, i.e. towards or onwards from any point in the model domain.

MT3D makes it possible to simulate 3D transport of contaminants within the model domain. Different transport processes like advection, dispersion, sorption, first-order decay and production reactions may be simulated independently or jointly.

6.3.2 Model Configuration

The following description of the model configuration, parameters and input values are based on the model documentation written by Helberg (2000). The model may perform both stationary and transient simulations. Only the stationary flow model will be discussed and used here.

Layers

Five individual layers were originally defined in the model, including the terrain level and bedrock surface, based on a seven layer stratigraphic model made by SINTEF (1993). This model was developed based on surface observations, seismic investigations, sonder drillings and sedimentological well logs. When assigning the distribution of hydrogeological properties, a geological model of grain size distribution by VBB VIAK (1990; 1992) was used, in addition to grain size analyses and pumping tests. In general, the layers have decreasing grain size with depth, as from proximal towards distal parts of the deposit. In order to reduce the number of dry cells in the upper layer when running the model using new values on precipitation input, the two upper layers have been merged into one (pers. comm. B. Wejden). The definitions of the model units are slightly different east and west of the groundwater divide, as the upper units are coarser and thicker in the east. The flow properties within the layers are given by assigning specific values to the flow parameters; horizontal and vertical hydraulic conductivity and effective porosity. The material properties may vary within one layer.

Boundary Conditions

A standard sized cell in the model is 100 times 100 meters. In some areas, along the eastern and western runways and the railway track, the cell width is reduced in order to increase the resolution. The active model domain covers 52.39 km^2, approximately half of the Romerike aquifer. A constant head boundary surrounds the model area, except in the north and south (pers. comm. Wejden), corresponding to observed heads in the rivers Sogna and Vikka in the southwest and to Lake Hersjøen and the river Risa in the northeast. In order to simulate the western ravine area, the K values are high in the vicinity of the river Sogna. In addition cells within the modelled area representing Lake Transjøen and Lake Danielsetertjern have constant head, while cells representing basement exposure (Garderfjell) are inactive and represent no flow boundaries.

Waterbalance

When running stationary simulations, the precipitation input is the total precipitation measured in 1998, which was 3790 mm. Asphalted surfaces are considered to have zero recharge. Surface runoff is constricted to Garderfjell, in addition to asphalted surfaces. How much water that is infiltrated on other surfaces is dependent on evaporation, which is assigned different values dependent on surface properties: 30% from asphalted surfaces, 40% within area regulated by airport and 50% in surrounding area. In addition, there are a number of artificial infiltration- and drainage-points.

Calibration

The model was calibrated for stationary flow using hydraulic head data from November 1975 (98 observations) and June 1993 (144 observations) by D. Helberg. When performing these tests, pre-airport surface properties were used together with measured precipitation and estimated groundwater renewal (based on discharge in the river Risa) for the particular year; for exact values consult Helberg (2000). For both stationary simulations there is a fair agreement between observed and calculated head. The residuals have close to normal distribution around the calibration line, with minimum and maximum deviations of -5.02 m to 6.5 m (1975) and -4.39 m to 6.21 m (1993), respectively. Mean residuals are 1.30 (1975) and 1.10 (1993). Water balances were performed within four zones surrounding the airport (north, south, east and west) in addition to the total area. Neither displayed any substantial deviations.

Sensitivity and Verification

Sensitivity analyses were performed using the data set from November 1975. In the case of stationary flow, the model proved to be more sensitive to reduction than to increase in hydraulic conductivity. With mean absolute error < 1.5 m and scaled RMS < 5% as criteria for acceptable deviation, reductions in hydraulic conductivity < 15% and increases < 25% will be insignificant with respect to the final result. When considering groundwater recharge, the model was equally sensitive to increases or decreases, and < 15% would not be significant.

The final, calibrated model, taking the hydrogeological changes induced by the airport into account, was verified comparing simulated head with 36 observations from April 1998. The results were satisfactory with absolute error of 1.02 m and scaled RMS = 3.69%.

6.4 Results

The existing OSL model (Helberg, 2000; Wejden, 2005) has been run and compared with the hydraulic heads observed in this study and the water ages presented in section 5.4.

6.4.1 Hydraulic Head Observations

In the field, hydraulic head was measured at 13 well points (the remaining 5 well points are BAT wells and permanently installed submersible pumps). In some of the multilevel wells, however, two different groundwater levels were noted for filters at different depths. Despite this feature not being included in the model, all observed hydraulic heads are plotted below in order to represent reality (15 observations).

In some areas the terrain surface in the model (SINTEF, 1993) display large deviations from the observed height above sea level. As the surface level is averaged within each cell, some surface features will disappear. The largest terrain deviations were at well points in the kettle-hole depression at Trandum (wells TM1 – 8) and wells in the steep slope west of Lake Transjøen (wells TW1 – 2). These differences caused difficulties when comparing observed versus calculated hydraulic head. Instead of using the observed hydraulic head given as m.a.s.l. as input data, the depth of the groundwater table below surface (m.b.s.) has been subtracted from the simulated surface level of the particular well in the model. By assuming the modelled terrain surface to be a representative neutral point, the deviations are reduced. Plotting of filter depths in later sections has been done in the same way.

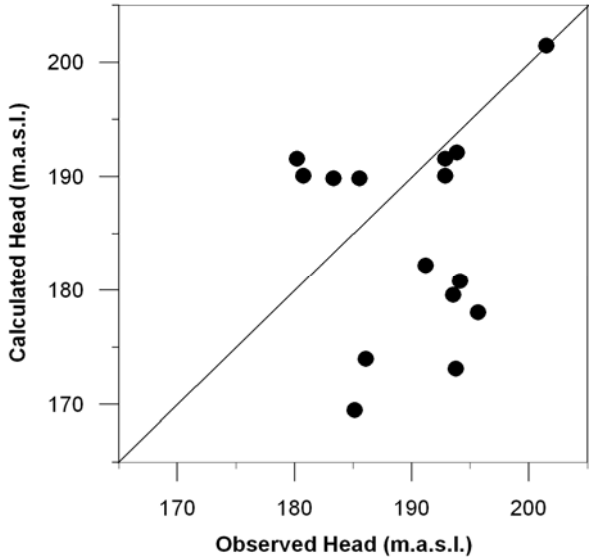

Figure 6.4: Observed versus calculated groundwater level (m.a.s.l.), plotted in relation to the modelled terrain surface. Plotted values and residuals are given in appendix F1.

Deviating points in the upper left half of the plot in figure 6.4 are all wells west of Lake Transjøen or at Trandum. As previously mentioned, these are the locations where the deviations between the real surface level and the model terrain are the largest. The three points deviating the most in the lower right part of figure 6.4, might be caused by a lower confined unit. Two of them have been observed as a second, deeper groundwater table in the lower filters of multilevel wells RB123 and GE345. The third well with lower groundwater level is GE1, which is a single well, but in the vicinity of the shallower GE2 which display a groundwater level much closer to what is calculated.

Based on figure 6.4 it seems that the model is more accurate within the relatively flat airport area, except for the deep wells in the eastern part where the aquifer is thought to comprise a lower, confined unit.

6.4.2 Flow Patterns and Residence Times

In figure 6.5 below the general flow pattern towards the filters in the sampled wells are displayed, viewed in the xy plane. Using the MODPATH function, a particle was placed at the location of each well screen and tracked backwards to the point of infiltration.

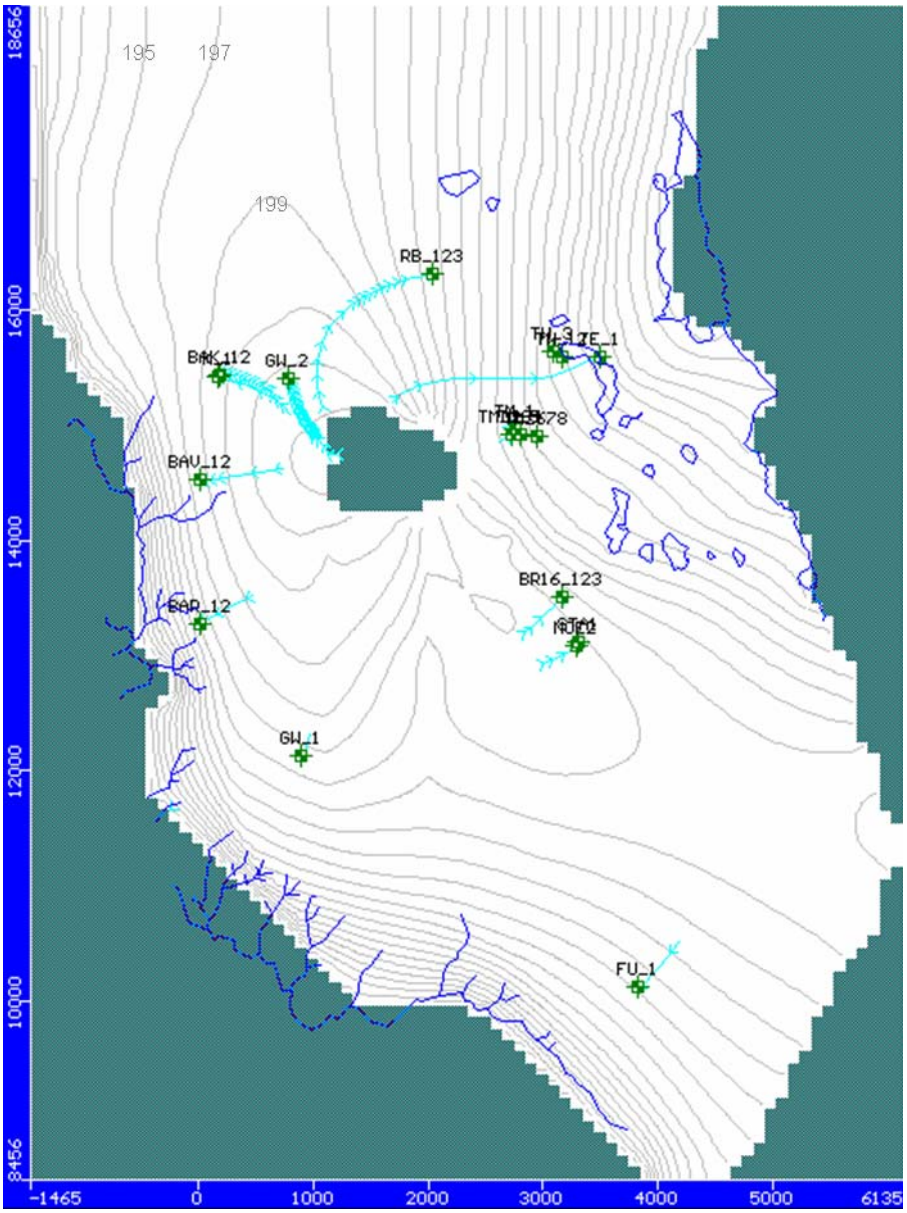

Figure 6.5: Backwards particle tracking from sampled well screens performed using the MODPATH package. Where wells are multilevel, the deepest screen has been plotted, except at GE3 – 5 where a particle was placed on top of the lowermost inactive layer at 173 m.a.s.l. Between each arrowhead is a travel time of two years. Head equipotentials are given with 2m intervals.

Each arrowhead represents a flow period of two years. In this figure the deepest screens are inserted where the wells are multilevel, except in GE3 – 5, where the two deeper screens were situated in the lowermost inactive layer. In order to still give an impression of the infiltration area, a particle was tracked from the top of the inactive layer; from 173 m.a.s.l. The aqua colour of the pathlines indicates the third dimension; that particles also move inwards in the plane of viewing; which is downwards in reality (grey colour would indicate outwards or upwards movement).

The well screens were plotted in relation to the simulated terrain surface, as described above. In some wells particle tracking could not be performed, as well screens plotted above the simulated groundwater table (TM2, TM4 – 8 and TW1 – 2). As previously mentioned GE3 – 4 plotted within the inactive layer and could not be tracked.

In general the model shows that water infiltrates at or near groundwater ridges and flows downwards in the direction of the largest decrease in head, perpendicular to the equipotential lines. Wells near the groundwater divide, to which the groundwater infiltrates almost vertically, display slower velocities (shorter intervals between arrows). This is due to lower conductivities in the z direction within each cell. The residence times are listed in appendix F2 and summarised in the plot below.

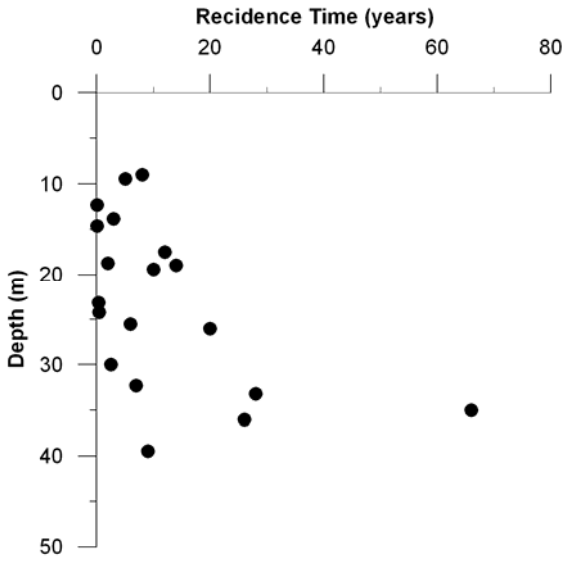

Figure 6.6: Plot of simulated residence times in years versus depth.

Figure 6.6 shows increasing age with depth, which is expected in a closed flow system like the Gardermoen aquifer, having inflow only from precipitation on the surface. There are, however, some surprisingly low residence times. Unfortunately, in some of these wells (FU1, BAV1 – 2 and BAR1 – 2) it is not possible to measure hydraulic head. However, in other deep wells displaying remarkably low residence times (e.g. TM1 and TM3) the screens plotted in the model are situated just below the groundwater table, while they are in fact several meters below. The simulated hydraulic heads displayed large deviations from observed heads in certain areas (cf. figure 6.4). This will have a large effect on the estimated residence times. There was no evident regional trend with respect to residence times.

Dated Wells

Particle tracking has been performed for the wells from which water was dated (c.f. section 5.4). The resulting residence times are displayed in table 6.1. For wells TM2, TM6 and TW2 simulations could not be performed (discussed above). The correlation between simulated and calculated (dated) residence times is generally poor. The large deviation in sample 2 (GW2) may, however, be caused by error in dating results rather than in the simulation (c.f. section 5.4). This is the case also in sample 7, where the isotope dating analyses yielded a negative result.

Sample NO	Well Name	Place	Screen A.	GW depth	Iso. Age	Sim. Age
			m	m	y	y
1	agri sch (FU1)	Furusmo	30,00	-	17,64	3,20
1	duplicate	Furusmo	30,00	-	22,44	3,20
2	G20 (GW2)	Gardermoen, West	35,22	4,20	4,37	66,00
3	NGU62_c (TM2)	Trandum Military Camp	20,70	17,00	3,75	-
3	NGU62_b (TM3)	Trandum Military Camp	24,20	17,00	3,31	0,50
4	NGU B3B (TM1)	Trandum Military Camp	23,12	14,00	5,61	0,38
5	NGU61_c (TM6)	Trandum Military Camp	17,50	9,50	6,45	-
6	G14	Moreppen	5,50	4,50	0,50	0,17
7	G10	Moreppen	5,50	4,50	-0,11	0,33
8	NGU43 (TW2)	Lake Transjøen, West	16,80	13,80	4,57	-
9	NGU21	Trandum Military Camp	29,75	26,00	0,27	1,04

Table 6.1: Measured (^{3}H-^{3}He dating) water ages and simulated residence times.

7. Discussion

7.1 Geochemical Processes

7.1.1 Carbonate Dissolution

Most of the contribution of Ca^{2+} and HCO_3^- within the saturated zone is due to calcite dissolution (cf. section 2.4.4). According to Jørgensen *et al*. (1991) 48.5% of the bicarbonate may be assigned to calcite dissolution. In addition, bicarbonate is produced during weathering of silicates and to a small extent from degradation of organic matter (Appelo & Postma, 2005). Ca^{2+} is also supplied through additional processes, like leaching of fossil seawater and weathering of silicate minerals. These processes are expected, however, to make up for less than 3 % of the total concentration (Jørgensen *et al*., 1991). Calcium containing silicates at Gardermoen are anorthite ($Ca(Al_2Si_2)O_8$) and hornblende ($(Ca, Na)_2(Mg, Fe, Al)_5(Al, Si)_8O_{22}(OH, F)_2$, of which anorthite is present in larger amounts Jørgensen *et al*. (1991) and display higher weatherability (Lasaga, 1984).

The magnesium content in calcite at Gardermoen is 2.5 mole % according to studies by Jørgensen *et al*. (1991). There is a linear relationship between the concentrations of bicarbonate and magnesium, but there are additional processes increasing the amount of the latter. The Mg^{2+} concentrations in all samples exceed 2.5 mole % of the bicarbonate expected to originate from carbonate dissolution (48.5%). Among the silicate minerals found at Gardermoen the largest magnesium contributor is the breakdown of chlorite. Minor contributors are hornblende and biotite. Markedly elevated concentrations were found in TM2, TM4 and TM5 at the landfill (upper part of the saturated zone), which may be explained by increased mineral dissolution due to acid leachate or direct input from waste (and in GE3 at the airport). Among deeper wells, TE1, BAK2 and FU1 displayed somewhat elevated values, which might indicate influence of fossil seawater and/or higher amount of ions due to long residence times.

Below the calcite weathering front, which is situated at a depth of approximately ten meters at Moreppen and Trandum (Jørgensen *et al*., 1991; Basberg, 1999), a sudden increase in concentrations of calcium and bicarbonate is expected, with the amount mainly dependent on the P_{CO2}. The regional distribution of the extent of the decalcified zone is uncertain. Since the wells sampled in this study all (except BAV2 at 9.41 m and BAK1 at 8.98 m) have relatively

deep screens (well below 10 m), the marked increase in bicarbonate concentrations at the calcite dissolution front cannot be observed (figure 7.1). The relatively constant concentrations of bicarbonate relative to depth (excluding wells at Trandum) confirm that most of the calcite dissolution has occurred within the upper saturated zone at the calcite dissolution front, where infiltrating water soon approaches equilibrium with respect to calcite according to the P_{CO2}. The PHREEQC simulations confirmed that calcite dissolution is the dominant weathering process, with an average dissolution of 1.31 mmol.

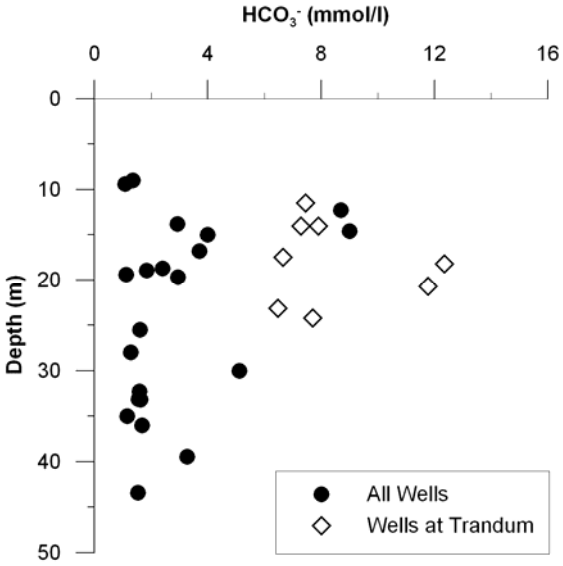

Figure 7.1: Plot of bicarbonate concentrations versus depth.

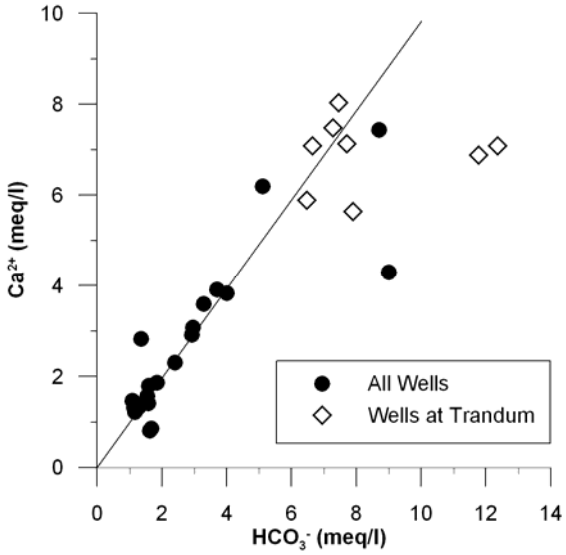

Figure 7.2: Plot of bicarbonate versus calcium concentrations. Line indicating the Ca-HCO_3 relationship found by Jørgensen et al. (1991).

A close to linear relationship between calcite and bicarbonate concentrations is evident in figure 7.2. The line in the plot, having a slope of 0.982, illustrates the relationship between the total meq of carbonic acid consumed and the bicarbonate and calcium produced from calcite weathering as found in the output-input budget by Jørgensen *et al*. (1991). The data is fitted fairly well, which verifies that approximately 48.5% of the total bicarbonate production within the aquifer may be subscribed to calcite weathering. Deviating points above the line; FU1 and BAK1, are indicative of higher relative silicate weathering, as the relative calcium content is higher.

All wells at Trandum display relatively high alkalinity; their content of calcium seems to be correspondingly high, except in wells TM2, TM4 and TM5. When concentrations of both

calcium and bicarbonate are elevated, it may be explained by increased calcite dissolution due to higher P_{CO2} and acid input. The tendency for alkalinity to decrease with depth at the Trandum landfill, as observed by Sæther *et al*. (1992), was also found in this data set. Wells TM2 and TM4 (the two upper screens in central multilevel well) are situated in the central part of the landfill, while TM5 is shallow and lies slightly downstreams, and these display the highest alkalinities. The excess bicarbonate in shallow and central parts of the landfill is likely to be due to the degradation of organic matter, which is consistent with observations of low oxygen content and high temperatures (cf. section 3.3.4). In the remaining dataset GE3 and GE2 (to a lesser extent), shallow wells at the airport, also displayed high alkalinity relative to calcium content. Along with low oxygen saturation relative to depth, biodegradation is a possible cause, although largely elevated TOC levels were not observed in this study and have also been found in routine investigations by OSL.

7.1.2 Silicate Weathering

The weathering rates of silicates are slow relative to calcite distribution. Although equilibrium is not reached, and the weathering reactions continue along the flow path, most of the silicate weathering is also assumed to take place in the unsaturated and the upper saturated zone (Jørgensen *et al*., 1991). This was the conclusion also in forward modelling of the geochemical processes at Gardermoen, performed by Heidenstrøm (1999).

The results in this study confirm that weathering of silicates along the flow path is minor, compared to that in shallower parts of the aquifer. There is no evident trend of increasing amounts of cations or silicon with depth. In figure 7.3 below is a plot of the dissolution of silicates according to the geochemical modelling results.

When performing the inverse geochemical modelling in PHREEQC, part of the original purpose was to use samples from multilevel wells as reference points along the flow path in the aquifer and run inverse modelling on the difference in solution at the different filter depths. It proved, however, to be impossible, as the differences in the solutions were too small, and did not show consistent or balanced variations in between two depths. This is also an indication that little weathering is happening along the flow path in the deeper aquifer. Instead, models were run between an average infiltration input and the concentration in each of the water samples, to capture the regional picture. When comparing these final models to

each level in the multilevel wells, the small differences were consistent with the regional trend (figure 7.3), which is discussed below.

As displayed in figure 7.3, the amount of dissolved K-mica and K-feldspar is fairly constant with depth, and although both are among the major silicates present in the sediments, they are only modest contributors to the water chemistry, releasing only small amounts of potassium and silicon. As mentioned in section 4.2, the dissolution of K mica was preferred when choosing plausible models, based on observations by Teveldal (1990). The total surface area of K-mica in the sediments is assumed to be much larger, which makes it more exposed to weathering than K-feldspar. Modelling the breakdown to secondary minerals at Gardermoen, using this PHREEQC phase assemblage, will not be accurate, as the program is based upon total dissolution and precipitation of minerals. The weathering of mica is, however, not always complete. Therefore numerous intermediate products and x-ray amorphous phases are present in the sediment as secondary phases (Teveldal, 1990). As the silicon content in the different product phases is different and silicon is also absorbed, the precipitation of secondary clay minerals in these models is probably not representative. In order to simulate such processes, a more specific secondary phase assemblage would have to be given. The focus of this study has, however, been mainly on the reactants.

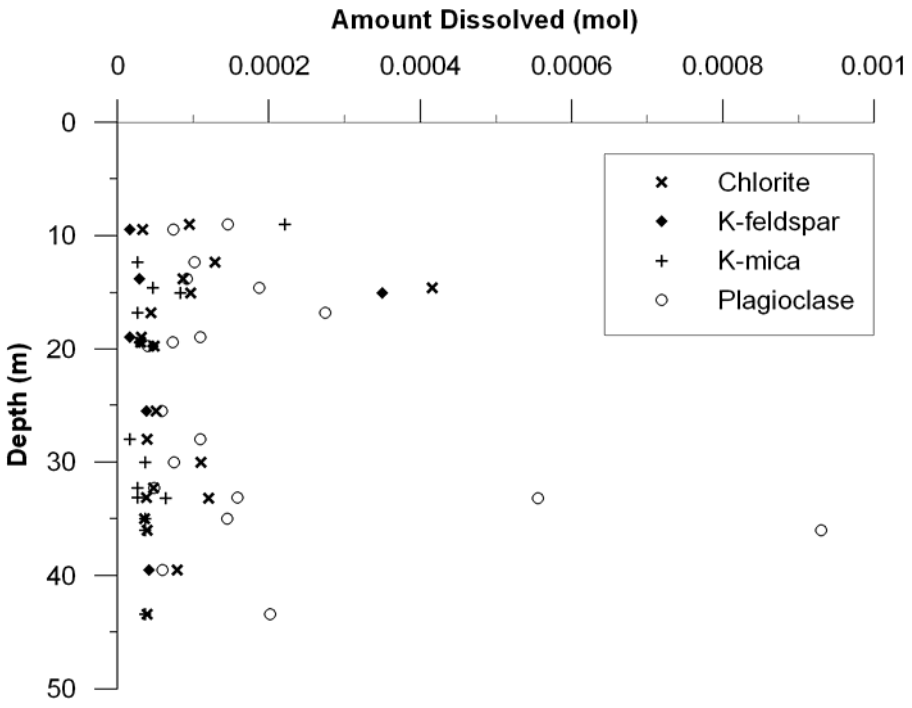

Figure 7.3: Plot of the amount of dissolved silicates versus depth, based on the PHREEQC geochemical modelling results (appendix D2).

Chlorite is more weatherable and dissolves to a larger extent than K-feldspar and K-mica (as seen in figure 7.3), adding magnesium and calcium to the solution. There is, however, no evident increase with depth, indicating that the dissolution along the flow path is minor.

Consistent with studies by Jørgensen *et al.* (1991) and with the modelling performed by Heidenstrøm (1999), is also a slightly larger dissolution of plagioclase compared to chlorite within the aquifer. From the results displayed in figure 7.3 it also seems to be a clear trend of plagioclase dissolution to proceed with depth, *i.e.* along the flow path.

In figures 7.4 and 7.5 below, the concentrations of magnesium, sodium and potassium relative to bicarbonate concentrations as analysed in water samples are plotted.

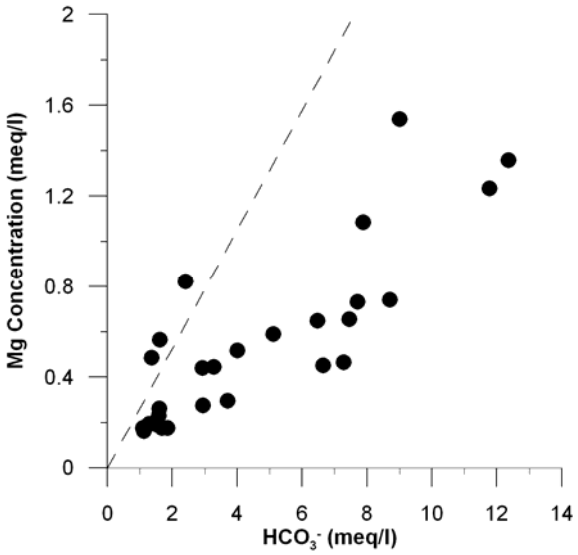

Figure 7.4: Plot of bicarbonate versus magnesium concentrations. Dotted line indicates the relationship given in Jørgensen et al. (1991).

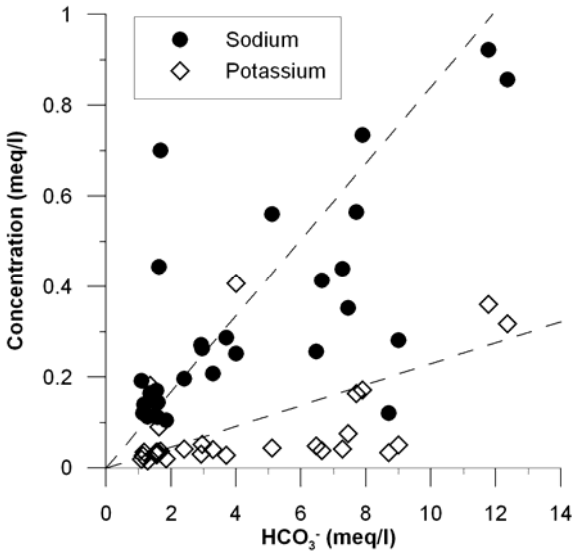

Figure 7.5: Plot of bicarbonate versus sodium and potassium concentrations. Dotted line indicates the relationship given in Jørgensen et al. (1991).

When comparing the distributions of the major cations relative to bicarbonate (figures 7.2, 7.4 and 7.5) found in this study, which are representative of the total amount of acid consumed in weathering reactions, to the relations as given in Jørgensen et al. (1991), it seems that slightly less magnesium and potassium is being released. Relating this to the geochemical processes, it would seem that less chlorite (releasing Mg) and less K-mica or K-feldspar (releasing K) is dissolved within the aquifer. It is also possible that the Mg content in calcite and/or chlorite is lower on a regional scale relative to the mineral analyses performed at Nordmoen (Jørgensen et al., 1991).

As mentioned above; the release of calcium seems fairly consistent with the budget calculations by Jørgensen et al. (1991). Sodium displays a more scattered distribution relative to the bicarbonate. Exceeding values (above the dotted line in figure 7.5) may indicate more extensive weathering of the sodic plagioclase, consistent with the observed trend of plagioclase dissolution along the flow path. High sodium values correlate, however, also with elevated chloride concentrations. The subject of anthropogenic and seawater input is discussed in section 7.1.3. Sodium and calcium concentrations may vary relative to each other due to cation exchange. This is assumed, however, in general, to be in equilibrium in the sediments, and systematic variations were not observed.

7.1.3 Fossil Seawater

Within the saturated zone chloride is considered a conservative, non reactive ion. Elevated concentrations in groundwater at Gardermoen may be due to anthropogenic sources in shallower wells (*e.g.* road salt, leachate), or influence by fossil seawater leaching/diffusing from underlying marine layers (cf. section 2.4.3). In figure 7.8 below, the chloride concentrations are plotted relative to depth below the surface. FU1 displays a very large deviating value, and may be disregarded, as it might be a case of sample contamination. Other high values in the upper saturated zone are assumingly due to anthropogenic input such as road salt, as these are all wells close to roads or farms. Wells at Trandum display elevated concentrations, as is expected for groundwater influenced by leachate.

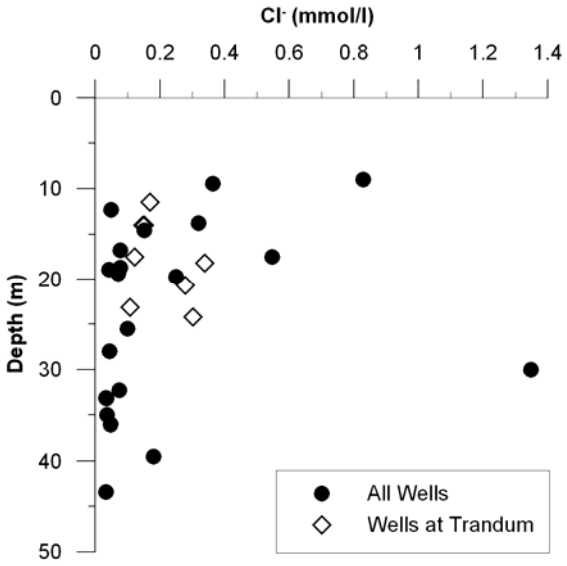

Figure 7.8: Plot of chloride concentration versus depth.

Among concentrations in deeper wells (>20 m), there is also no direct relation with depth. Ideally a plot should have been made also relative to the distance to the underlying marine layers, but such information is not available. There seems, however, to be a correlation with the assumed flow length and probable residence time near or within the marine bottomset unit. The highest concentrations are found in wells furthest east and west of the groundwater divide (BAR2, BAV1, TE1, TW), and are close to, or higher than the concentrations found in the river Risa (Jørgensen *et al*., 1991). The geochemical modelling results related to the extent of seawater influence display the same trends as the chloride concentrations, as the dissolution of halite was defined as a direct function of chloride concentrations.

7.1.4 Pyrite Oxidation

The only natural source of sulphate within the aquifer is oxidation of pyrite (cf. section 2.4.4). As this process is dependent on oxygen supply, the addition of sulphate is expected to decrease as oxygen is being consumed. The sulphate concentrations observed in this study have a uniform distribution with depth, which corresponds well with the studies by Basberg (1999), where the pyrite oxidation front is suggested to be located just above the calcite dissolution front, and sulphate to stabilize with depth. The oxygen content in deeper groundwaters is low (cf. section 3.3.4), which will be a limiting factor for the oxidation process to proceed with depth.

According to the modelling results, an average of 0.08 mmol/l pyrite was dissolved. The concentrations of sulphate display no increasing trend with depth, which indicates that oxygen is a limiting factor on pyrite oxidation. The presence of iron in some wells shows that not all has been precipitated as $Fe(OH)_2$ and the conditions are reducing. The redox zoning is discussed further in section 7.1.5.

Released protons from pyrite oxidation (according to equation 2.5) may associate with HCO_3^- and increase calcite dissolution (Basberg, 1999). The process is summarised in equation 7.1 below.

$$FeS_2 + 4CaCO_3 + 15/2\, O_2 + 7/2\, H_2O = Fe(OH)_3 + 2SO_4^{2-} + 4Ca^{2+} + 4HCO_3^- \qquad \textit{Eq. 7.1}$$

In figure 7.9 a correlation between bicarbonate and sulphate seems evident, but protons released through pyrite oxidation (dotted line in figure 7.9) contribute to only small parts of calcite dissolution.

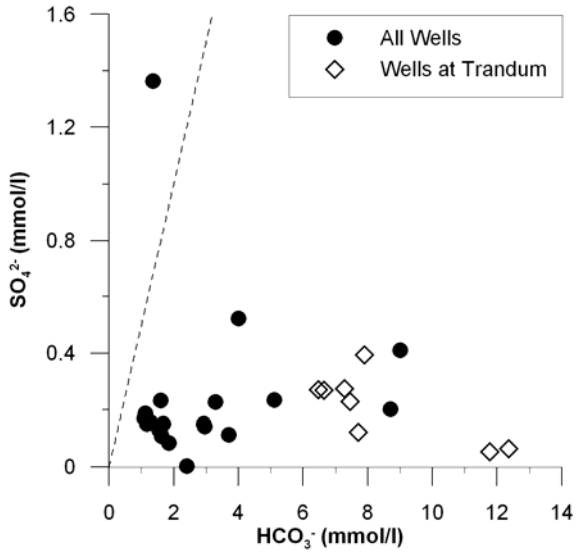

Figure 7.9: Plot of bicarbonate versus sulphate. The contribution from protons released through pyrite oxidation is indicated with a dotted line.

Well BAK1 at Kabberudsæther stands out with a remarkably high concentration of sulphate; 1.36 mmol/l, relative to the mean concentration of 0.23 mmol/l, indicating anthropogenic input. Also K1 and GE3 display elevated concentrations.

7.1.5 Redox Zonation

The aquifer comprises an upper oxic zone, cf. section 3.3.4, and a lower oxygen depleted or anoxic zone (Jørgensen *et al*., 1991). It is generally observed in natural environments, that redox processes proceed sequentially from the highest energy yield along the flow path in an aquifer, starting with the consumption of oxygen (Lovley & Goodwin, 1988). These processes are reflected in the groundwater chemistry, by the relative concentrations of redox sensitive species.

At the Trandum landfill the redox conditions are different from what is observed in other parts of the aquifer, as a strongly reducing plume of leachate has formed under the landfill.

Basberg (1999) made a sequential model of the plume aqueous chemistry, based on 18 water samples taken in the area. The model result is displayed in figure 7.10.

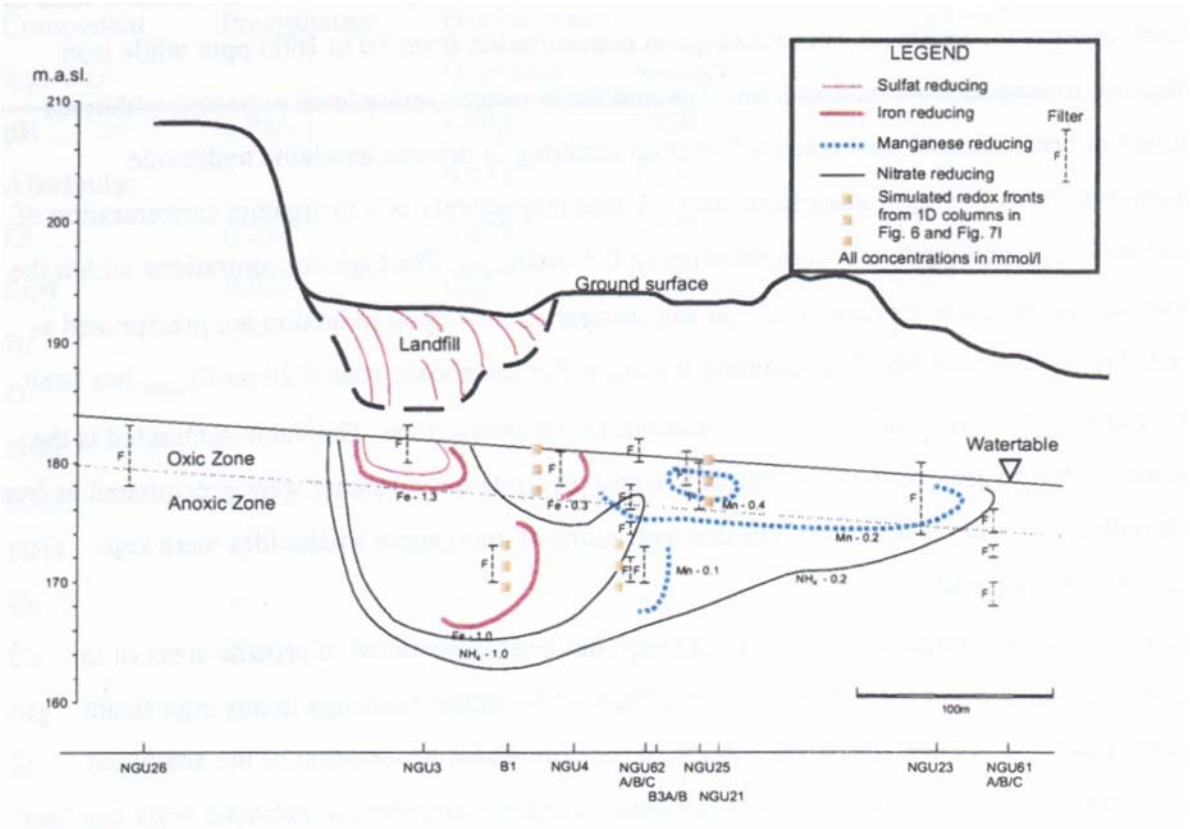

Figure 7.10: Vertical crossection (a surface map with is given in appendix A3) through the Trandum landfill, displaying modelled redox zonation (Basberg , 1999). Well B3B = TM1, NGU62A/B/C = TM2 – 4, NGU25 = TM5 and NGU61A/B/C = TM6 – 8.

The crossection is made along the direction of groundwater flow. Some of the wells sampled in the study by Basberg (1999) were also sampled in this study: TM1 - 8. Corresponding well names are given in the figure text. A surface map of the landfill showing the placement of the crossection is given in appendix A3. It is now seven years since the area was investigated and the model was made, and it is expected that the plume has advanced since then.

Nitrogen Species

The main source of nitrate in groundwater is normally application of fertilizers and manure in agriculture. Oxidation of organically bound nitrogen (nitrification) in soils is another, but minor, contributor (Appelo & Postma, 2005). Nitrate is reduced by bacteria in the soil, forming N_2, with nitrite as an intermediate product (denitrification). Nitrate may also, but to a lesser extent, be reduced to ammonium. The reduction series of common nitrogen species, with decreasing energy yield, may be written as (Appelo & Postma, 2005);

$$NO_3^- \rightarrow NO_2^- \rightarrow N_{2(g)} \rightarrow NH_4^+ \qquad \textit{Eq. 7.2}$$

Relatively high concentrations (>0.01 mmol/l) of nitrate were found in wells RB3, TM6 – 8, and TW2, all in the upper part of the saturated zone. Nitrite was detected only in wells TM2 – 5, which are situated in the central part of the landfill. Ammonium was found only in some wells and in very small amounts, except for elevated concentrations in shallow wells TM8 (downstreams of the Trandum landfill) and K1.

TM8 corresponds to the shallowest filter in well NGU61 in figure 7.10, and it seems that it is now within the nitrate reducing, outer fringe of the plume, based on the relatively high amount of ammonia. However, there is also relatively high concentration of nitrate, indicating that the change towards a reducing environment is relatively recent. The two lower filters are not yet affected by this.

Iron and Manganese

Elevated values of Fe^{2+} and Mn^{2+} in groundwater indicate reduction of Fe(III) and Mn (IV) in solid phases within the aquifer. Iron and manganese are present in various amounts in the sample solutions. It may be observed from the samples that, in general, either ion is dominating with respect to the individual concentration.

Wells TM2 and TM4 at Trandum, which are the two upper screens of NGU 62 in figure 7.10, display high concentrations of both Fe^{2+} and Mn^{2+} are high. This indicates that the plume has advanced, and that the screens now lie within the iron reducing zone. The lower screen, TM3, has much lower concentrations, still with manganese as a dominant species. TM5 (NGU25), which is situated slightly downstreams of the multilevel well (TM2 – 4), is still within the manganese reducing zone. TM1 (B3B) is situated in the northern fringe of the landfill, and is not highly affected by the leachate. It displays relatively low values of both iron and manganese.

Sulphate Reduction

The distribution of sulphate concentrations within the aquifer was discussed in the previous section. There was no general trend of increase (pyrite oxidation) or decrease (sulphate reduction) with depth.

Among the wells at Trandum, which all have relatively high concentrations of sulphate compared to the regional average (figure 7.9), the two upper screens TM2 and TM4 in the central multilevel well (NGU62 in figure 7.10) display markedly lower sulphate values compared to surrounding and downstream wells. This indicates sulphate reducing and sulphide forming conditions (Sæther *et al*., 1992). From this observation it seems that the sulphate reducing zone is more extensive than in the model (figure 7.10). Also high concentrations of dissolved iron are observed in TM2 and TM4, which would be expected to precipitate as iron sulphides. A surplus of dissolved iron relative to sulphide prevents total removal as long as sulphide precipitates. Also, Postma & Jakobsen (1996) suggest that Fe(III) and sulphate reduction may occur simultaneously or even reversed, depending upon stability of the iron oxides present and pH.

Present Redox Zonation at Trandum

Based on the observations of the relative distributions among redox species at Trandum, it seems that the plume has advanced since the last study was performed by Basberg (1999), as would be expected. The observed nitrate and iron reducing fronts seem, based on the observations described above, to have advanced in the order of 20 – 150m relative to the zonation in figure 7.10. It may seem, however, that the sulphate reducing zone was somewhat underestimated by Basberg (1998), as it now seems to comprise wells TM2 and TM4 (NGU62AB).

Regional Redox Zonation (excluding wells at Trandum)

Deeper groundwater at Gardermoen belongs, according to the definition by Lasaga (1984), to the post oxic zone. Nitrate seems to have been largely reduced or to a little extent entered the saturated zone, as the concentrations are generally low. No significant amounts of nitrite (except in a shallow well at Vigstein) were found, indicating that nitrate reduction is not a very active process.

The extent, to which the iron reducing zone has been reached, varies. There is no distinct regional pattern in the distribution of manganese and iron. In some of the multilevel wells, however, increasing reducing conditions with depth is evident (RB1 – 3, GE3 – 5). High concentration of iron in the upper saturated zone at Kabberudsæther may indicate some sort of anthropogenic influence. More reducing conditions in the upper- relative to the lower saturated zone were also found at the Horse Ranch and Vigstein Farm, indicating

antropogenic influence. The shallow well GE2 at the airport had high concentrations of manganese, which, along with elevated concentrations of bicarbonate and low oxygen saturation, indicates increased biological activity, most probably due to input of de-icing chemicals.

7.2 The Organic Fraction

Dissolved organic matter (DOM) is a highly complex mixture of organic compounds, of which it is impossible to give a general characteristic as to its structures and sources, which may be very different and also vary regionally. DOM is continuously affected by processes like sorption and desorption, dissolution and precipitation, aggregation and disaggregation. Here the organic fraction within the saturated zone has been studied with respect to the amount and configuration of organic carbon and the polarity of compounds.

7.2.1 Total Organic Carbon

Although not quantitatively reliable, the results from the liquiTOC analyses may be viewed semi-qualitatively as a screening of sampled wells with respect to the contents of organic carbon. The concentrations of non purgeable organic carbon (NPOC) vary within the interval 40 – 520 µmol/l. For comparison, Thurman (1985) suggests 60 µmol/l total organic carbon (TOC) to be a "typical" value for groundwater. The purgeable carbon fraction in the groundwater samples, which would add to NPOC in order to yield TOC, is not known. Still groundwater samples from the Trandum landfill stand out as to have a particularly high organic fraction. Abundance of organic material at Trandum fits well with observations of elevated temperatures and low content of oxygen (cf. section XX), which might indicate exothermal degradation of organic material and lowered pH, which may be caused by the production of organic acids. Higher NPOC values at Trandum are consistent with TOC observations made in the OSL environmental surveillance program (Holm, 2000) and studies by Basberg (1999). Apart from the observations at Trandum, highly elevated concentrations were found in wells BAK1 – 2 and GEW1; here there are no obvious surface sources. Well K1 at Kabberudsæther (in the vicinity of BAK1 – 2) is discussed in the following section.

7.2.2 Distribution of Organic Fractions

Further analyses of 11 samples with respect to the organic fraction, using TLC-FID, yielded more reliable quantitative results. These confirmed somewhat elevated values of the total organic fraction at Trandum, although the analysed samples were from the multilevel well TM6 - 8 downstreams of the landfill and not in the central part. Furthermore, K1 and RB1 displayed markedly elevated concentrations, which were not evident in the liquiTOC analyses. Based on this small sample set, displaying relatively large variations, it is not possible to determine a background value for the organic fraction at Gardermoen. The individual distributions between the saturated, aromatic and polar fractions, however, seem to be fairly constant; with a large polar fraction, a smaller saturated fraction and an indeterminable aromatic fraction. The polar fraction comprised 72 – 93 % of the total organic fraction in the sample set, with a mean of 83%. The tripartite configuration of the polar peak, as pointed out in section 3.3.5, is characteristic in all samples, independent of concentration. The organic polar fraction in groundwater is expected to consist mainly of weak organic acids, the main groups being carboxylic, hydroxylic and phenolic acids. As the pH in the groundwater at Gardermoen generally is quite high; >7, it would be expected that the acids in solution are not highly protonised and are negatively charged. Carboxylic acids are the strongest and the most polar, with pK_a's less than 5, while phenolic acids are the weakest and least polar, with pK_a's larger than 8. Hydroxylic acids are intermediate (Appelo & Postma, 2005).

The polarity of an acidic compound belonging to either of these groups will also depend on the number and properties of the functional groups affecting the m/z ratio. The pK_a's within a main group of acids will often display a normal distribution (Appelo & Postma, 2005). Less polar compounds may be mobilised by a solvent with π-electrons, such as toluene, and rise on the chromarods. A plausible explanation of the tripartite configuration would be that phenolic acids, comprising a benzene ring, and having low pK_a, would be slightly mobilised by toluene and rise on the chromarod, forming the first and least polar peak. The middle peak would subsequently represent hydroxylic acids, and the last, largest and most polar peak would represent carboxylic acids. This is an over-simplification of reality as the compounds are numerous and different, representing a continuum with respect to polarities, but might fit as a general characteristic of the organic acids in this particular aquifer, as the pattern seem to be very consistent.

7.2.3 Saturated and Aromatic Compounds

The saturated fraction eluated by hexane yielded one single peak in the TLC-FID chromatograms, being of variable size in all samples. A certain identification of aromatic compounds eluded using toluene, could not be established. Three samples were subject to further investigation of the saturated and aromatic fractions, by GC-FID and GC-MS. These analyses are not quantitative (no standard was added), and aimed only at identifying individual compounds and their relative distributions.

As the saturated fraction in these three samples seems to be elevated, it is of interest to look into whether the distribution of organic compounds could reveal whether the excess organic content might be due to anthropogenic input.

Sample K1

A distribution of heavy n-alkanes; C19 – C32, was recognised in both GC-FID and GC-MS chromatograms (cf. section 3.3.5). The alkanes found were long-chained and heavy, having low water solubilities. The presence of aromatic biomarker derived products; phenantrene and methyl-phenantrenes, as identified with GC-FID, and an UCM configuration, are signs of biodegradation. The shape and size of the UCM indicates that there has been more than one period of biodegadation (Peters et al., 2005). The degradation seems quite extensive, as only heavy n-alkanes are left, and biodegradation normally starts at C8 – C10 (Karlsen *et al*., 1995). It is not possible to determine if the biodegradation has occurred *in situ*. Some petroleum products consist of oil that has already been biodegraded in the reservoir, such as poor quality diesel oil ("bunker oil"). This is, however, not extensively used other than in shipping. Most of the common commercial petroleum products are, however, not biodegraded. Based on this, it may be assumed that most of the biodegradation has occurred *in situ* or while the petroleum products moved from the surface and down into the aquifer, and that the contaminant is old.

There is no obvious surface source of hydrocarbons. However, a relatively high total concentration and a large saturated fraction relative to the polar fraction (cf. TLC-FID results) indicate an additional input of saturated hydrocarbons relative to natural background levels. Also, that the entire saturated fraction can not have been generated by natural activity in the sediments, is proven by the presence of phenantrenes, which are never formed in recent

sediments (Peters et al., 2005). A possible source for organic contamination is the previous military airport, of which the northern part is likely to be comprised in the infiltration area of this well considering the general flow pattern. Elevated TOC concentrations were, however, not detected in the infiltration area when mapping the influence on groundwater quality from previous activities (Holm, 2000). As the well is situated at a farm and downstreams of a road, another likely source would be a point spill or leakage of a petroleum product such as fuel.

Sample TM8

As in sample K1, heavy alkanes were recognised in both GC-FID and GC-MS, while phenantrenes and methyl-phenantrenes were identified in the GC-FID chromatogram. Also in this sample n-alkanes were heavy; C22 – C36, with low water solubilities. Although an UCM heap is absent, the presence of phenantrene and methyl-phenantrenes, as well as lowered concentrations of lighter alkanes, indicate biodegradation (Peters *et al*., 2005).

The Trandum landfill seems to be an obvious source of the excessive hydrocarbons in the downstream well TM8, as high TOC values have been determined in the area (cf. section 3.3.5; Basberg, 1999; Holm, 2000) and as the presence of organic contamination in an old landfill is likely. TM8 is the shallowest screen in a multilevel well, and compared to the two lower screens, the concentration of saturated hydrocarbons is markedly higher. This fits well with the observations of redox species, discussed previous, showing that the plume of leachate has reached the TM8 well. Thereby it is likely to believe that also the excess organic fraction origin from the landfill. Although how, and to what extent, the organic contaminants from the Trandum landfill is spreading, is not known.

In samples TM6 - 8 the polar fraction was also high and consistent with the elevated saturated fraction (in contrast to K1). This may be explained by the excess production of organic acids at the landfill, which is a typical feature of relatively young leachates, and is believed to be the cause of the observed low pH's at Trandum (Sæther *et al*., 1992).

The overall distribution of n-alkanes, phenantrene and methyl-phenantrenes seems quite similar to the K1 sample both in range and order of relative magnitudes. This might indicate a similar source. The fact that the UCM heap is absent signifies less biodegradation and thereby a younger pollutant.

Sample RB1

In the RB1 sample heavy alkanes C23 - C33 were identified with both GC-FID and GC-MS. The saturated fraction in this sample was the largest among the ones analysed. A distinct odd-even pattern was observed (figure 3.12), which indicates selective biodegradation. This process is currently poorly understood, and may not be explained based on what is known of bacteria cultures, but is observed in some biodegraded oils in commercial oil fields (pers. comm. D. Karlsen, 2006).

Positive identifications were made of PAH's in GC-MS analyses. The 4, 3+2 and 1 isomers of methyl-dibenzothiophenes, phenantrene and the 3, 2, 1 and 9 isomeres of methyl-phenantrenes were found. This allows the maturity of the source rock for this oil to be determined. The vitrinite reflectance, $\%R_V$, may be calculated using the following equations (Kvalheim et al., 1987; Radke, 1988);

$$\%R_V = 2.242 \cdot F1 - 0.166$$

$$\%R_V = 0.073 \cdot MDR + 0.51$$

Where F1 describes the relationship between the peak heights in the chromatogram of the methyl-phenantrene isomeres by (3+2)/(3+2+9+1), and MDR is the ratio of the two methyl-dibenzothiophenes 4 and 1 (4/1). The calculations are possible as isomers 3 and 2 of methyl-phenantrene are more stable than are the 9 and 1 isomers. Similarly, for methyl-dibenzothiophenes, isomer 4 is more stable than isomer 1. The maturities calculated are 0.86 for methyl-phenantrene, and 0.74 for methyl-dibenzothiophenes, respectively. Methyl-dibenzothiophenes are assumed to yield the most accurate determination of $\%R_V$ for such relatively immature oils (Peters et al., 2005); therefore 0.74 is considered representative. Using the correlation between $\%R_V$ and temperature given by Price (1992), this transcribes into a temperature of about 150^{o}C. Assuming a first approximation on a geothermal gradient of 35^{o}C/km, this is evidence for the original petroleum to have been generated in a source rock at about 4 km depth. Based on this, it is certain that there has been antropogenic input of the saturated fraction, in well RB1.

RB1 is the lowest screen in a multilevel well north of the Gardermoen airport. The concentrations of the saturated fraction are increasing with depth, as seen in the TLC-FID analyses of RB1 – 3. As evident from the PAH distributions, a natural source of these fractions within the sediment is not possible. A known surface source does not exist. The infiltration area of this well may be in the same region as for K1; somewhere on the northern part of the groundwater table ridge, making the previous military airport a possible source. Furthermore, there have been various other military activities in the area in the vicinity of these wells, since the 2. world war and up until now (Holm, 2000). The extremely large polar fraction, however, is not a common feature of petroleum products. This feature is not valid for the two shallower well screens. This might indicate a second, natural source, *e.g.* an upstreams peat layer, or a secondary alteration process.

7.3 Residence Times

Calculated water ages (cf. section 5.4) proved to be well fitted to the general assumption on residence times and flow patterns at Gardermoen (*e.g.* Østmo, 1976; Jørgensen & Østmo, 1990; Wong, 1996). The ages increase with depth below the groundwater table. At present the dataset comprises too few samples, however, to yield a proper regional overview. More, and also deeper, samples are needed in addition to the dataset from 1999 (previous results, presented in section 5.4) in order to establish an impression of flow lines. When the analyses of the ten samples taken during this study (cf. section 5.5) are concluded, the picture will be more complete.

Comparison of the calculated water ages to simulations performed using the 3D groundwater flow model in development at OSL (Helberg, 2000; Wejden, 2005), proved difficult, mainly because of divergences in the observed and simulated head distribution. The main problem in this regard seemed to be that the terrain surface level in the model domain was poorly fitted to real observations in some areas; especially near Lake Transjøen and at Trandum. Also in some areas, a lower, confined unit is observed (GE1, GE4-5 and RB1-2), which is not included in the model, thus causing head deviations. Apart from in these areas, the simulated residence times, as calculated by backward particle tracking from the screen points, yielded increasing residence times with depth and flow length. The simulations of residence times performed for the wells that were dated in 1999, were in general not very well fitted. For wells 2 and 4, however, the dating results – rather than the model - seem to be wrong (cf.

section 6.4.2). To improve or to evaluate the quality of the groundwater flow model is not within the scope of this study. In the further development and calibrations of the model to be carried out at OSL, however, the final results of the isotope analyses may be used as indicators of model accuracy.

Among the preliminary results K1 seems to be the "oldest" sample, having the longest residence time. This well is not very deep compared to the other sampled wells. From detailed stratigraphical mapping performed by Sønsterudbråthen (1994) at Kabberudsæther, it is known that the K1 screen is situated 6 m above the top of the bottomset unit (22 m.b.s.) in fine to medium grained sand. The pump is permanently installed and very powerful, as it is used for agricultural purposes. Possibly affecting the apparent water ages could be that older water is pulled also from the underlying, marine layers while pumping, or that part of the groundwater has been retained in clay lenses. FU1 is believed to be situated (there are no available well logs) right above the marine layers, and also here fossil water could potentially be pumped, as the permanently installed pump is very powerful. Two samples from FU1 were analysed in 1999, yielding sample ages of approximately 17 and 22 years, respectively. The preliminary results of the new isotope analyses of the FU1 sample indicate a much higher age. It might be possible that some of these variances are due to mixing with fossil water.

8. Conclusions

This master thesis, as a whole, may be viewed as a regional chemical characterization of deep groundwater at Gardermoen. The project aim was to determine whether regional and/or depth-related chemical differences existed in within the aquifer, based on the set of water samples which have been collected and analysed during this study. The results were further to be related to the dominating geochemical processes occurring along the groundwater flow path. Also part of the project was to look into to what extent it was possible to investigate the organic fraction in the groundwater, by means of the instrumentation available at the institute. Finally, residence times were to be determined by isotope dating of part of the sample set, and presented along with previously unpublished water age data from Gardermoen. The findings and conclusions are summarized in the following.

Calcite dissolution was confirmed to be the dominating weathering process and the aquifer may be classified as a Ca^{2+} and HCO_3^- system. The PHREEQC modelling results yielded an average amount of dissolved calcite of 1.31 mmol/l. Most of the dissolution is confirmed to happen in the upper saturated zone, as the Ca^{2+} and HCO_3 concentrations are fairly constant with depth. In accordance with Jørgensen *et al.* (1991) approximately 48.5% of the bicarbonate may be assigned to calcite dissolution.

The results of this study confirms that weathering of silicates along the flow path is minor, compared to in shallower parts of the aquifer. The geochemical modelling results confirm plagioclase to be the silicate mineral contributing the most to the groundwater chemistry, followed by chlorite and K-mica (K-feldspar). It seems that, however, on a regional scale, it is less dissolution of chlorite and K-mica than predicted by Jørgesen et al. (1991). Furthermore, plagioclase dissolution appears to proceed along the flowpath, *i.e.* concentrations increase with depth.

The chloride content, indicative of the extent of fossil seawater contribution, shows no direct relation with depth. Depth below the surface is not consistent with the closeness to the bottomset unit on a regional scale. There seem however, to be a correlation with the assumed flow length and probable residence time near or within the marine bottomset unit. Excessive concentrations of chloride in the upper saturated zone was recorded in some areas, in addition

to leachate influenced wells at Trandum, and are assumed to be due to anthropogenic input from road salt.

Pyrite oxidation is the only natural source of sulphate within the aquifer. The sulphate concentrations displayed no increasing trend with depth, as is expected along with the observed low oxygen saturations, i.e. most of the pyrite oxidation occurs in the oxic upper saturated zone. The observed relationship between bicarbonate and sulphate indicates that protons released from pyrite oxidation do contribute to calcite dissolution, as suggested by Basberg (1998), but to a small extent.

Deeper groundwater at Gardermoen, as represented by the dataset of this study (excluding wells at Trandum), belongs to the post oxic zone. Concentrations of nitrate are generally low. The extent, to which the iron reducing zone has been reached, varies. Either manganese or iron is predominant in sample concentrations. Sulphate reduction was not evident. Comparing the concentrations of redox sensitive species at Trandum to the observations and leachate-plume aqueous geochemistry modeling performed by Basberg (1999), the plume seems to have advanced somewhere in the order of 20 – 150m. Furthermore, the extent of the sulphate reducing zone seems to have been underestimated.

During the investigations of the organic fraction in groundwater, liquiTOC analyses turned out to be quantitatively unreliable for the low concentrations generally found in the groundwater at Gardermoen. Elevated concentrations of organic material were observed at Trandum and Kabberudsæther.

TLC-FID analyses of 11 wells yielded good, quantitative estimations of the organic fraction. A tripartite configuration in the peak representing the polar fraction in TLC-FID chromatograms, common for all samples, may be viewed as a characterisation of the distribution among organic acids at Gardermoen, with respect to polarity. Based on this, carboxylic acids are most abundant, followed by phenolic and hydroxylic, respectively.

In further analyses of the relatively large saturated fractions in samples K1, RB1 and TM8, with GC-FID and GC-MS, positive identifications of heavy n-alkanes (higher than C19) were made in all samples. The presence of phenantrenes (and methyl-dibezothiophenes in RB1) proves anthropogenic input. The samples displayed various amounts of biodegradation; with

K1 being the most biodegraded, and TM8 the least, respectively. The contaminant sources for K1 and RB1 are unknown. For TM8 the Trandum landfill seems to be an obvious source, with high observed TOC values.

As the ^{3}H-^{3}He dating of the water samples collected during this study has not yet been concluded; the present dataset of previous results (cf. section 5.4) comprises too few samples in order to establish a regional overview of residence times. The current dataset displays, however, increasing ages relative to the depth below the groundwater table, corresponding to the general assumption on residence times. Modeling of residence times using the OSL 3D model (Helberg, 2000; Wejden, 2005) for comparison with the isotope ages, proved to be difficult due to large head and surface deviations in some areas.

8.1 Recommendations for Future Studies

This study has provided interesting results with respect to the organic content of the groundwater at Gardermoen. Further work may be carried out concerning the characterisation and identification of the dissolved organic matter, first of all by analysing a larger set of samples to establish a regional overview of background levels and potential anthropogenic input. It would also be interesting to see whether the tripartition of the polar fraction, as observed in this study, is reproducible and valid for the entire region, and to identify compounds in the polar fraction by use of GC columns designed for organic acids.

The NFR project on dating the deep groundwater by use of the ^{3}H-^{3}He – method, will be continued after the submittal of this thesis. When a more extensive dataset of residence times is established, it may be related to regional chemical differences and flow paths. In future development of groundwater flow models representing the Gardermoen aquifer, the dating results may be used in the calibration process, as means for evaluating the model accuracy. Furthermore, when the dating results are available, they may be related to the organic contamination found in this study (or future studies), and prove useful in considerations of possible sources and biodegradation rates.

References

Aeschbach-Hertig, W., Peeters, F., Beyerle, U. & Kipfer, R. 1999. Interpretation of dissolved atmospheric noble gases in natural waters. *Water Resources Research* **35**(9), 2779-2792.

Aeschbach-Hertig, W. W. 1994. Helium und tritium als tracer für physikalische prozesse in Seen. Unpublished Dr. thesis, Eidgenössische Technische Hochschule Zürich.

Appelo, C. A. J. & Postma, D. 2005. *Geochemistry, groundwater and pollution*. Balkema, Leiden.

Basberg, L. 1999. Field and numerical investigations of landfill leachate in the Gardermoen glaciofluvial aquifer, Norway. Unpublished Dr.ing thesis, Norwegian University of Science and Technology.

BAT. 2006. BAT groundwater sampling equipment. Available at: http://www.bat-gms.com. (Accessed: 12.05.2006).

Beaty, R. D. & Kerber, J. D. 2002. *Concepts, instrumentation and techniques in atomic absorption spectrophotometry*. Unpublished user's manual.

Beyerle, U., Aeschbach-Hertig, W., Hofer, M., Imboden, D. M., Baur, H. & Kipfer, R. 1999. Infiltration of river water to a shallow aquifer investigated with $^{3}H/^{3}He$, noble gases and CFCs. *Journal of Hydrology* **220**(3-4), 169-185.

Beyerle, U., Aeschbach-Hertig, W., Imboden, D. M., Baur, H., Graf, T. & Kipfer, R. 2000. A mass spectrometric system for the analysis of noble gases and tritium from water samples. *Environmental Science & Technology* **34**(10), 2042-2050.

Brennwald, M. 2006. Personal communication. (E-mail 31.05.2006).

Bogen, J. 1989. Glacial sediment production and development of hydro-electric power in glacierized areas. *Annals of Glaciology* **13**, 6-11.

Butt, F. A. 1997. Hydrogeological modelling of an E-W traverse across the Trandum delta. Unpublished Cand. scient thesis, University of Oslo, The Gardermoen Project, Report Series C, No 9.

Bøyum, A. & Kaaa, B. 2001. Limnologisk metodikk. Biologisk Institutt, Universitet i Oslo, 61 p.

Clark, I. D. & Fritz, P. 1997. *Environmental isotopes in hydrogeology*. Lewis Publishers, New York.

Craig, H. 1957. Distribution, production rate, and possible solar origin of natural tritium. *Physical Review* **105**(3), 1125-1127.

Craig, H. & Lal, D. 1961. The production rate of natural tritium. *Tellus,* 13(1), 85-105.

Dagestad, A. 1998. In situ luftinjeksjon i grunnvannssonen som opprensningstiltak i akviferen ved Gardermoen, Sørøst Norge. Unpublished dr.ing thesis, Norwegian University of Science and Technology.

Dincer, T. & Davis, G. H. 1967. Some considerations on tritium dating and the estimates of tritium input function. In: *Memoirs of the 8th Congress of the International Association of Hydrogeology*, Istanbul, 276-186.

Domenico, P. A. & Schwartz, F. W. 1997. *Physical and chemical hydrogeology*. Wiley, New York.

Ekwurzel, B., Schlosser, P., Smethie Jr, W. M., Plummer, L. N., Busenberg, E., Michel, R. L., Weppernig, R. & Stute, M. 1994. Dating of shallow groundwater: Comparison of the transient tracers $^{3}H/^{3}He$, chlorofluorocarbons, and ^{85}Kr. *Water Resources Research* **30**(6), 1693-1708.

Elverhøi, A., Svendsen, J. I., Solheim, A., Andersen, E. S., Milliman, J., Mangerud, J. & Hooke, R., LeB. 1995. Late Quaternary sediment yield from the high Arctic Svalbard area. *Journal of Geology* **103**(1), 1-17.

Faure, G. 1998. *Principles and applications of geochemistry.* Prentice-Hall, Upper Saddle River.

Faure, G. & Mensing, T. M. 2005. *Isotopes; principles and applications*. John Wiley & Sons, Hoboken.

Follestad, B. A. & Østmo, R. S. 1977. Eidsvoll Kvartærgeologisk kart, 1915, 1:50 000. Norges geologiske undersøkelser, Trondheim.

Fontes, J. C. 1980. Environmental isotopes in groundwater hydrology In: *Handbook of environmental isotope geochemistry* (edited by Fritz, P. & Fontes, J. C.) **Vol 1A**. Elsevier, Amsterdam, 545 p.

Fontes, J.C. 1985. Some considerations on groundwater dating using environmental isotopes. In: *Hydrology in the service of man 1, Memoirs of the 18th congress of the international association of hydrogelogists* (edited by Fritz, P. & Fontes, J. C.), Cambridge, 118-154.

Gat, J. R. 1980. The isotopes of hydrogen and oxygen in precipitation. In: *Handbook of environmental isotope geochemistry* (edited by Fritz, P. & Fontes, J. C.) **Vol 1A**. Elsevier, Amsterdam, 22-47.

Gvein, Ø., Sverdrup, T. L. & Skålvoll, H. 1973. Hamar NP 31, 32-16. Preliminært berggrunnskart. Norges geologiske undersøkelser, Trondheim.

Hafsten, U. 1979. Late and post-Weichselian shore level changes in South Norway. In: *The Quaternary history of the North Sea* (edited by Oele, E., Schüttenhelm, R. T. E. & Wiggers, A.) **2**. Societas Upsaliensis pro Geologia Quaternaria, Uppsala, 45-59.

Haldorsen, S., Riise, G., Swensen, B. & Sletten, R. S. 1997. Environmental isotopes as tracers in catchments. In: *Geochemical processes, weathering and groundwater recharge in catchments*. A.A Balkema, Rotterdam, 185-210.

Haswell, S. J. 1991. *Atomic absorption spectrometry : theory, design, and applications*. Elsevier, Amsterdam.

Heidenstrøm, B. 1999. Geokjemisk modellering av Gardermoenakviferen. Unpublished Cand. scient thesis, University of Oslo.

Helberg, D. 2000. Grunnvannsmodell for Oslo Lufthavn AS – Modelldokumentasjon. In: *Report: OSLAS-AN-RA-0020.*

Holm, T. 2000. Grunnvannskvalitet på Gardermoen. Vurdering av vannkvalitet fra miljøovervåkningsprogram. In: *Report: OSLAS-AN-RA-0035.*

Holtedahl, O. 1924. Studier over israndterrassene syd for de store østlandske sjøer. *Videnskapsselskapets skrifter. I Matematisk-naturvidenskabelig klasse* (14), 1-109.

Holtedahl, O. 1974. Noen glasifluviale israndavsetninger i den sydlige del av Glommavassdragets (nåværende) dreneringsområde : med en del berggeologisk-morfologiske data fra de nordlige Øyeren-trakter. *NGU skrifter* **306**, 1-85.

Hongve, D. 1977. The ionic composition of lakes fed by groundwater and precipitation in the Upper Romerike district. *Nordic hydrology* **8**, 141-162.

IAEA/WMO. 2006. Global Network of Isotopes in Precipitation (GNIP) and Isotope Hydrology Information System (ISOHIS), IAEA, Vienna. Available at: http://www-naweb.iaea.org/napc/ih/IHS_science2.html. (Accessed: 08.03.2006).

INRA, 2006. Institut National de la Recherche Agronomique, Paris. Available at: http://www.unsa.jouy.inra.fr/lipides/cpg.htm. (Accessed: 16.06.2006).

Johansson, T. 1987. *Kort innføring i anionkromatografi*. Unpublished users manual.

Jørgensen, P., Stuanes, A. O. & Østmo, S. R. 1991. Aqueous geochemistry of the Romerike area, Southern Norway. *Norges Geologiske Undersøkelse Bulletin* **420**, 57-67.

Jørgensen, P., Sørensen, R. & Haldorsen, S. 1995. *Kvartærgeologi* Landbruksforlaget, Oslo.

Jørgensen, P. & Østmo, R. S. 1990. Hydrogeology in the Romerike area, Southern Norway. *Norges Geologiske Undersøkelse Bulletin* **418**, 19-26.

Karlsen, D. A. 2006. Personal Communication. (Conversation 28.06.2006).

Karlsen, D. A. & Larter, S. R. 1991. Analysis of Petroleum Fractions by TLC-FID - Applications to Petroleum Reservoir Description. *Organic Geochemistry* **17**(5), 603-617.

Karlsen, D. A., Nyland, B., Flood, B., Ohm, S. E., Brekke, T., Olsen, S. & Backer-Owe, K. Petroleum geochemistry of the Haltenbanken, Norwegian continental shelf. In: *The geochemistry of reservoirs* (edited by Cubitt, J. M. & England, W. A.) Special publication No. **86**. The Geological Society, London, 203-256.

Kipfer, R. 1991. Primordiale edelgase als tracer für fluide aus dem erdmantel. Unpublished Dr. thesis, Eidgenössische Technische Hochschule Zürich.

Kitterød, N. O. 2004. Dupuit-Forchheimer solutions for radial flow with linearly varying hydraulic conductivity or thickness of aquifer. *Water Resources Research* **40**(11), W1150701-W1150705.

Kvalheim, O. M., Christy, A. A., Telnæs, N. & Bjørseth, A. 1987. Maturity determination of organic matter in coals using methyl-phenantrene distribution. *Geochemica et Cosmochimica Acta*, **51**, 1883-1888.

Lasaga, A. C. 1984. Chemical kinetics of water-rock interactions. *Journal of Geophysical Research,* **89,** 4009-4025.

Longva, O. 1987. Description of the Ullensaker 1915 II 1:50,000 Quaternary geologic map, with attached map. *NGU Skrifter* **76**, 1-39.

Longva, O. & Thoresen, M. K. 1989. The age of the Hauerseter Delta. *Norwegian Journal of Geology* **69**(2), 131-134.

Lovley, D. R. & Goodwin, S. 1988. Hydrogen concentrations as an indicator of the predominant terminal electron-accepting reactions in aquatic sediments. *Geochemica et Cosmochimica Acta*, **52**, 2993-3003.

Lønne, I. 1995. Sedimentary facies and depositional architecture of ice-contact glaciomarine systems. *Sedimentary Geology* **98**(1-4), 13-43.

Oftedahl, C. 1981. *Norges geologi : en oversikt over Norges regionalgeologi*. Tapir, Trondheim.

Oliver, B. M., Farrar, H. & Bretscher, M. M. 1987. Tritium half-life measured by ^{3}He growth. *Applied Radiation and Isotopes* **38**(11), 959-965.

Otnes, J. 1973. Hydrological Data – Norden Romerike, Norway. *Norwegian National Committee for the IHD.* Data Volume1965-1971.

Otnes, J. 1975. Hydrological Data – Norden Romerike, Norway. *Norwegian National Committee for the IHD.* Data Volume1972-1974.

Parkhurst, D. L. 1995. User's guide to PHREEQC - a computer program for speciation, reaction path, advectiv-transport, and inverse geochemical calculations. U. S. Geological Survey Water Resources Investigations. In: *Report 95-4227.*

Parkhurst, D. L. & Appelo, C. A. J. 1999. User's guide to PHREEQC (version 2) - a computer program for speciation, batch-reaction, one-dimensional transport, and inverse geochemical calculations. U. S. Geological Survey Water Resources Investigations. In: *Report 99-4259.*

Parkhurst, D. L., Thorstenson, D. C. & Plummer, L. N. 1980. PHREEQE – A computerprogram for Geochemical calculations. U. S. Geological Survey Water Resources Investigations. In: *Report 80-96.*

Pedersen, J. H. 2002. Atypical oils, unusual condensates and bitumens of the Norwegian Continental Shelf : an organic geochemical study. Unpublished Cand. scient thesis, University of Oslo.

Peters, K. E., Walters, C. C. & Moldowan, J. M. 2005. The biomarker guide. Cambridge University Press, Cambridge.

Plummer, L. N., Wigley, T. M. L. & Parkhurst, D. L. 1978. The kinetics of calcite dissolution in CO_2 -water systems at 5 degrees to 60 degrees C and 0.0 to 1.0 atm CO_2. *American Journal of Science* **278**(2), 179-216.

Postma, D. & Jakobsen, R. 1996.Redox zonation: Equilibrium constraints on the Fe(III)/SO_4^- reduction interface. *Geochemica et Cosmochimica Acta*, **60**, 3169-3175.

Potts, P. J. 1992. *A Handbook of silicate rock analysis*. Blackie Academic, Glasgow.

Price, L. C. 1992. Thermal stability of hydrocarbons in nature: limits, evidence, characteristics, and possible controls. *Geochemica et Cosmochimica Acta*, **57**, 3261-3280.

Radke, M. 1988. Application of aromatic compounds as maturity indicators in source rocks and crude oils. *Marine and Petroleum Geology* **5**, 224-236.

Rudolph-Lund, K. 1997. A three-dimensional, natural gradient tracer study in theRomerike aquifer near the Gardermoen international airport. Unpublished Cand. scient. thesis, University of Oslo, The Gardermoen Project, Report Series C, No 10.

Sæther, O. M., Misund, A., Ødegard, M., Andreassen, B. T. & Voss, A. 1992. Groundwater contamination at Trandum landfill, southeastern Norway. *Norges Geologiske Undersøkelse Bulletin* **422**, 83-95.

SINTEF. 1993. Grunnundersøkelser Gardermoen. Vurdering av grunnforhold In: *Report: STF69 F93023*.

Skarstad, B. 1996. Undersøkelse av løsmassene på Moreppen, Gardermoen : fysisk sammensetning, mineralogi og vannkjemi. Unpublished Cand. scient. thesis, Norwegian Agricultural University, The Gardermoen Project, Report Series C, No 4.

Solomon, D. K., Poreda, R. J., Schiff, S. L. & Cherry, J. A. 1992. Tritium and ^{3}He as groundwater age tracers in the Borden Aquifer. *Water Resources Research* **28**(3), 741-755.

Solomon, D. K., Schiff, S. L., Poreda, R. J. & Clarke, W. B. 1993. A validation of the ^{3}H/^{3}He method for determining groundwater recharge. *Water Resources Research* **29**(9), 2951-2962.

Stute, M. J. & Schlosser, P. 1993. Principles and applications of the noble gas paleothermometer. In: *Climate change in continental isotopic records* (edited by Swart, P. K., Lohmann, K. C., McKenzie, J. A. & Savin, S.) **78**, 89-100.

Sønsterudbråten, S. 1994. Et hydrogeologisk studie av de distale deler av Trandum is-kontakt delta. Unpublished Cand. scient thesis, University of Oslo, The Gardermoen Project, Report Series C, No 3.

Sørensen, R. 1979. Late Weichselian deglaciation in the Oslofjord area, South Norway. *Boreas* **8**(2), 241-246.

Sørensen, R. 1982. Pre-Boreal avsmelting i Sørøst-Norge In: *NORDQUA-eksursjon Turbeskrivelse Rapport 17*. Norwegian Agricultural University, Ås 77 p.

Sørensen, R. 1983. Glacial deposits in the Oslofjord area. In: *Glacial deposits in North-West Europe* (edited by Ehlers, J.). A.A Balkema, Rotterdam, 19-28.

Teveldal, S., Jørgensen, P. & Stuanes, A. O. 1990. Long-term weathering of silicates in a sandy soil at Nordmoen, southern Norway. *Clay Minerals* **25**(4), 447-465.

Thurman, E. M. 1985. *Organic geochemistry of natural waters.* Martinus Nijhoff/Dr. W. Junk Publishers, Lancaster.

Tuttle, K. J. 1990. A sedimentological, stratigraphical and geomorphological investigation of the Hauerseter delta and a hydrogeological study of the Westerly Øvre Romerike aquifer. Unpublished Cand. scient thesis, University of Oslo.

Tuttle, K. J. 1997. Sedimentological and hydrogeological characterisation of a raised icecontact delta - the Preboreal deltacomplex at Gardermoen, southeastern Norway. Unpublished dr. scient thesis, University of Oslo.

Tuttle, K. J. & Aagaard, P. 1996. Review of the depositional structure and hydrogeology of the northern Romerike aquifer. Unpublished paper, 1-28.

VBB VIAK AB. 1990. Gardermoen – Jordartsgeologsik modell. In: *Report: 122202.662360*.

VBB VIAK AB. 1992. Gardermoen – Komplettering av geomodell. In: *Report: S0943.000*.

Wejden, B. 2005. Modifications of unpublished 3D groundwater flow model in Visual Modflow, belonging to OSL.

Wejden, B. 2006. Personal communication. (Conversation, 23.05.2006).

Wong, W. K., Kitterød, N. O. & Pedersen, T. S. 1996. A 2D flow modell of the Trandum delta. In: The 6th seminar on hydrogeology and environmental geochemistry 1996, NGU 11-12 November, 1996. (edited by Frengstad, B.)

Østmo, R. S. 1976. Hydrogeologisk kart over øvre Romerike: grunnvann i løsavsetninger mellom Jessheim og Hurdalssjøen, 1:20 000. Norges geologiske undersøkelse. Universitetsforlaget, Oslo.

Østmo, S. R. 1975a. Kort beskrivelse til kvartærgeologisk kart, Gardermoen, 1:20 000, C QR O51 O52 - 20 og hydrogeologisk kart, øvre Romeriket, 1:20 000 In: *Upublisert NGU-rapport*. Norges geologiske undersøkelse, Oslo, 24 p.

Østmo, S. R. 1975b. Kvartærgeologisk kartlegging med spesiell vekt på registrering og undersøkelser av sand -og grusforekomster i Ullensaker kommune. In: *NGU-rapport O-75045*. Norges geologiske undersøkelse, Trondheim, 102 p.

Østrem, G. 1975. Sediment transport in glacial melt water streams In: *Glaciofluvial and glaciolacustrine sedimentation* (edited by Jopling, A. V. & McDonald, B. C.) **Special Publication 23**. Society of Econmic Paleontologists and Mineralogists, Tulsa, 101-122.

Aagaard, P. & Wensaas, L. 1994. Kompendium for G 242 sedimentologisk laboratorium. Institutt for Geologi, Universitet i Oslo, 61 p.

List of Appendices

Appendix A: Maps

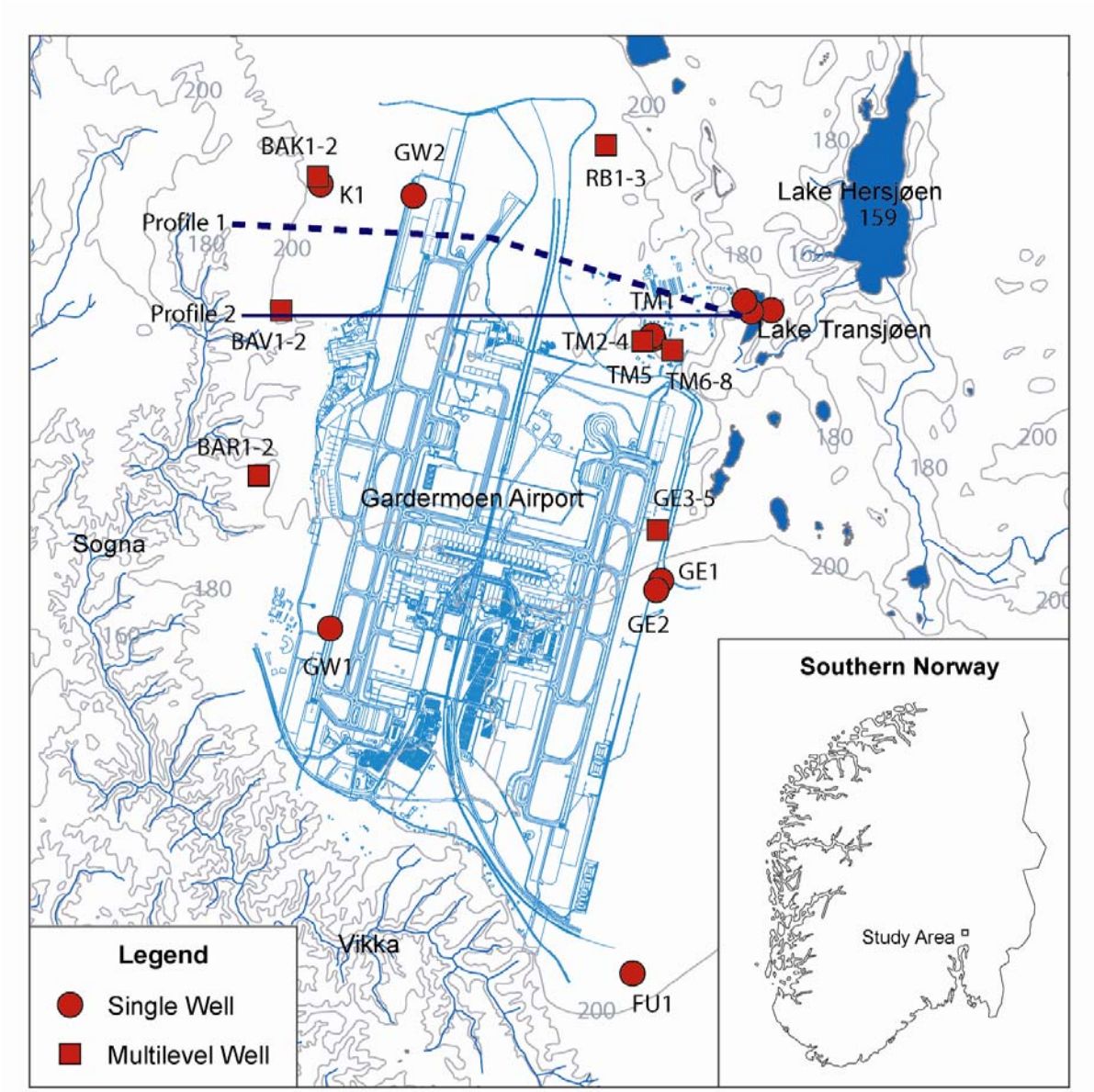
BAK1-2
K1
GW2
RB1-3
Lake Hersjøen
159
Profile 1
Profile 2
BAV1-2
TM1
TM2-4
TM5
TM6-8
Lake Transjøen
BAR1-2
Gardermoen Airport
GE3-5
Sogna
GE1
GE2
GW1
Vikka
FU1
Southern Norway
Study Area
Legend
Single Well
Multilevel Well

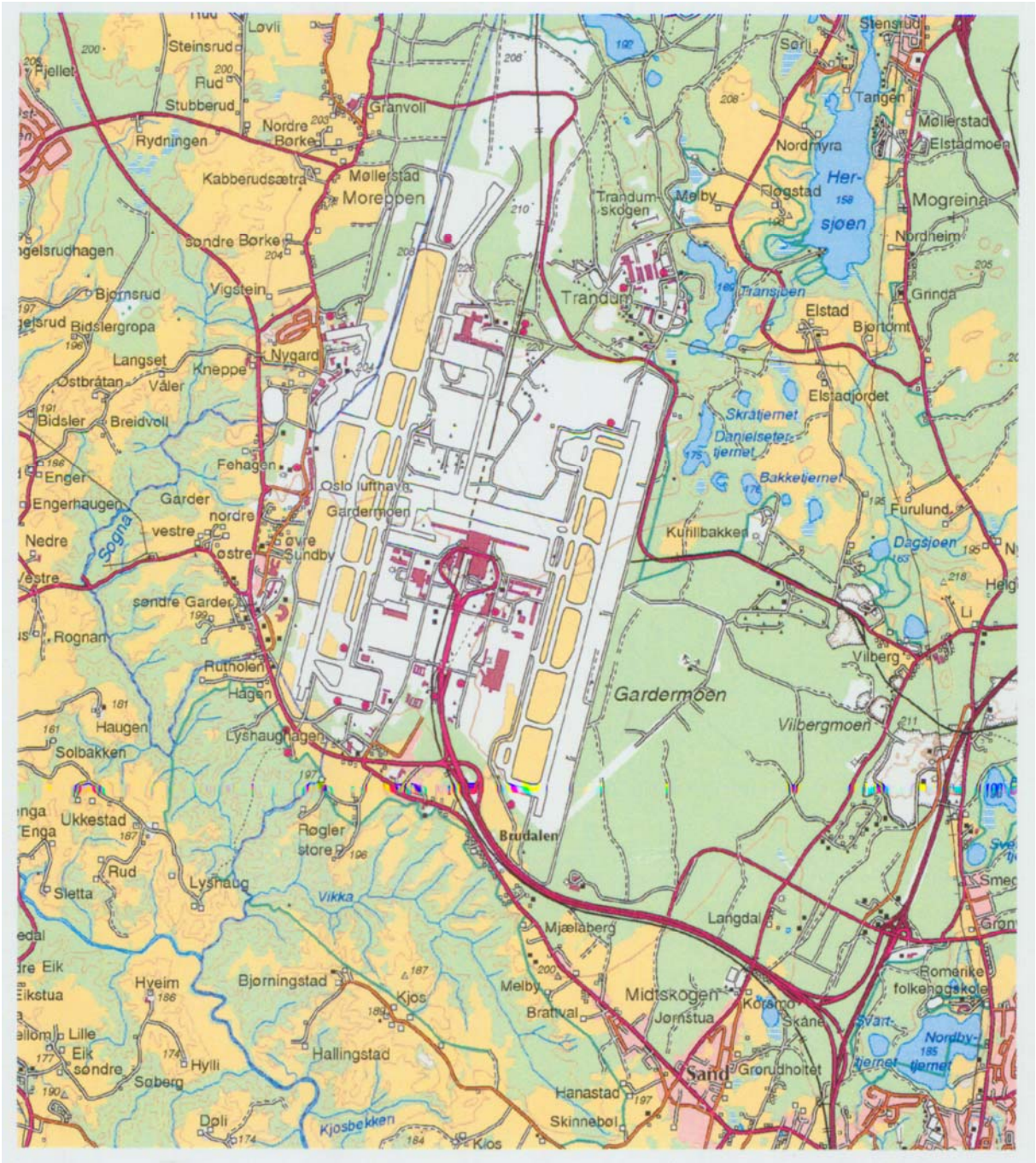
Lovli
Steinsrud
Rud
Stubberud
Granvoll
Nordre Borke
Rydningen
Kabberudsætra
Møllerstad
Moreppen
Søndre Borke
Bjørnsrud
Vigstein
Bidslergropa
Langset
Kneppe
Nygard
Østbråtan
Våler
Bidsler
Breidvoll
Enger
Fehagen
Engerhaugen
Garder
nordre
vestre
østre
Nedre
Sogna
Vestre
Øvre Sundby
søndre Garder
Rognan
Rutholen
Hagen
Haugen
Lyshaughagen
Solbakken
Ukkestad
Enga
Rud
Sletta
Lyshaug
Rogler store
Vikka
Eik
Hyeim
Bjørningstad
Kjos
Lille Eik
søndre
Hylli
Søberg
Hallingstad
Døli
Kjosbekken
Kios
Trandum
Trandumskogen
Melby
Oslo lufthavn
Gardermoen
Brudalen
Mjælåberg
Melby
Bratival
Hanastad
Skinnebol
Sand
Grorudhoitet
Midtskogen
Jornstua
Skåne
Langdal
Gardermoen
Vilbergmoen
Vilberg
Kuhilbakken
Skrattjernet
Danielsetertjernet
Bakketjernet
Elstad
Bjørtomt
Elstadjordet
Trans-sjøen
Grinda
Nordheim
Mogreina
Flogstad
Her-sjøen
Nordmyra
Tangen
Sørl
Stensrud
Møllerstad
Elstadmoen
Furulund
Dagsjøen
Romerike folkehøgskole
Svartjernet
Nordbytjernet

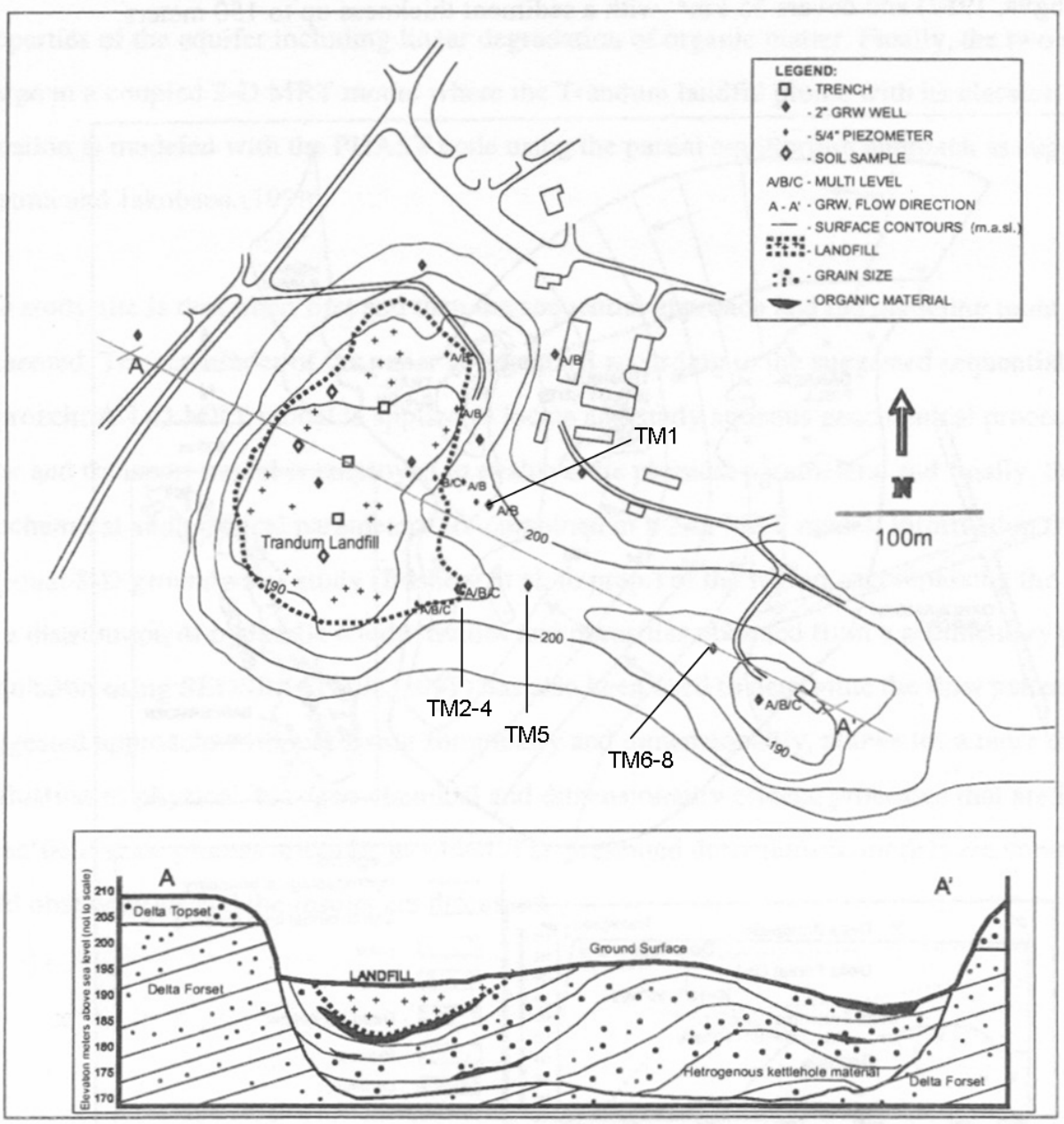
LEGEND:
- TRENCH
- 2" GRW WELL
- 5/4" PIEZOMETER
- SOIL SAMPLE
A/B/C - MULTI LEVEL
A - A' - GRW. FLOW DIRECTION
- SURFACE CONTOURS (m.a.sl.)
- LANDFILL
- GRAIN SIZE
- ORGANIC MATERIAL
A
A'
TM1
TM2-4
TM5
TM6-8
Trandum Landfill
190
200
N
100m
Elevation meters above sea level (not to scale)
210
205
200
195
190
185
180
175
170
Delta Topset
Delta Forset
LANDFILL
Ground Surface
Hetrogenous kettlehole material
Delta Forset

Appendix B: Chemical Data

	Well	Name	Place	Date	Elev.	Coord. N	Coord. E	Screen T.	Screen B.	Screen A.	GW depth	Temp.	pH	E.C.	Remarks
					m.a.s.l.			m	m	m	m	°C		microS/cm	
1	RB1		North of A.	14.05.06	205.00	60 13 24.0	11 06 55.7	35.50	36.50	36.00	18.05	10.2	8.6	172.8	
1	RB2		North of A.	14.05.06	205.00	61 13 24.0	12 06 55.7	27.50	28.50	28.00	18.05	8.8	7.5	157.1	
1	RB3		North of A.	14.05.06	205.00	62 13 24.0	13 06 55.7	18.45	19.45	18.95	15.83	9.2	7.3	202.0	
2	K1		Kabberudsæther Farm	25.05.06	205.00	60 13 15.7	11 04 31.9	14.00	16.00	15.00		6.7	7.1	482.0	GW depth not available
3	FU1		Furusmo	21.02.06	203.00	60 09 55.6	11 06 55.6	31.00	29.00	30.00		4.6	7.5	669.0	GW depth not available
4	TM1	NGU_B3B	Landfill at Trandum	07.12.05	193.87	60 12 35.5	11 07 16.1	21.37	24.87	23.12	12.04	8.8	7.3	578.0	influenced by leachate
5	TM2	NGU_62B	Landfill at Trandum	07.12.05	196.20	60 12 34.3	11 07 13.3	20.20	21.20	20.70	15.85	9.7	6.6	1022.0	influenced by leachate
5	TM3	NGU_62C	Landfill at Trandum	07.12.05	196.20	60 12 34.3	11 07 13.3	23.20	25.20	24.20	15.98	9.8	6.9	698.0	influenced by leachate
5	TM4	NGU_62A	Landfill at Trandum	07.12.05	196.20	60 12 34.3	11 07 13.3	17.20	19.20	18.20	16.00	6.2	6.5	1033.0	influenced by leachate
6	TM5		Landfill at Trandum	07.12.05	194.00	60 12 33.3	11 07 14.8	13.50	14.50	14.00	12.88	9.3	6.3	737.0	influenced by leachate
7	TM6	NGU_61C	Landfill at Trandum	10.05.05	186.50	60 12 32.0	11 07 26.1	16.50	18.50	17.50	9.30	9.7	7.73	675.0	influenced by leachate
7	TM7	NGU_61B	Landfill at Trandum	10.05.05	186.50	60 12 32.0	11 07 26.1	13.50	14.50	14.00	9.30	9.8	6.8	725.0	influenced by leachate
7	TM8	NGU_61A	Landfill at Trandum	10.05.05	186.50	60 12 32.0	11 07 26.1	10.50	12.50	11.50	9.30	9.3	6.5	773.0	influenced by leachate
8	TW1		Lake Transjøen, West	08.05.05	173.70	60 12 51.7	11 07 52.8	16.70	22.70	19.70	2.70	6.2	8.2	332.0	filter not depth specific (6 m)
9	TW2	NGU_043	Lake Transjøen, West	16.05.06	185.80	60 12 52.2	11 07 50.5	14.80	18.80	16.80	12.43	8.8	8.1	384.0	filter not depth specific (4 m)
10	TE1	TØ1	Lake Transjøen, East	08.05.05	177.00	60 12 41.2	11 08 19.0	29.50	49.46	39.48	6.98	7	7.2	388.0	filter not depth specific (20 m)
11	GE1	STA1	Gardermoen A., East	18.12.05	206.39	60 11 33.6	11 07 17.2	29.27	35.27	32.27	23.47	8.2	8.1	193.0	filter not depth specific (6 m)
12	GE2	MOE2-A01	Gardermoen A., East	18.12.05	204.72	60 11 32.3	11 07 15.2	8.30	16.30	12.30	10.83	9.2	7	826.0	filter not depth specific (8 m)
13	GE3	BR16	Gardermoen A., East	18.12.05	204.68	60 11 46.9	11 07 15.6	11.58	17.58	14.58	10.51	7.8	7.2	883.0	filter not depth specific (8 m)
13	GE4	BR16-B	Gardermoen A., East	18.12.05	204.71	60 11 46.9	11 07 15.6	32.11	34.11	33.11	22.61	7.5	7.7	179.6	
13	GE5	BR16-C	Gardermoen A., East	18.12.05	204.62	60 11 46.9	11 07 15.6	41.91	44.91	43.41	22.61	7.9	8.2	166.9	
14	GW1	BR29-B	Gardermoen A., West	26.01.06	201.59	60 11 24.7	11 04 28.7	17.30	20.13	18.72	7.98	7.8	7.9	478.0	
15	GW2	G20	Gardermoen A., West	26.05.06	207.00	60 13 06.9	11 05 19.9	34.00	36.00	35.00	4.22	6.1	7.6	148.9	
16	BAR-1		Horse Ranch	25.05.06	200.00	60 12 05.8	11 03 59.8	13.78	13.78	13.78		6.8	6.6	340.0	BAT well, GW depth not available
16	BAR-2		Horse Ranch	25.05.06	200.00	60 12 05.8	11 03 59.8	25.50	25.50	25.50		6.8	7.3	212.0	BAT well, GW depth not available
17	BAK-1		Kabberudsæther Farm	25.05.06	205.00	60 13 15.7	11 04 31.9	8.98	8.98	8.98		6.8	6.25	512.0	BAT well, GW depth not available
17	BAK-2		Kabberudsæther Farm	25.05.06	205.00	60 13 15.7	11 04 31.9	33.20	33.20	33.20		7.9	6.4	180.5	BAT well, GW depth not available
18	BAV-1		Vigstein Farm	25.05.06	202.50	60 12 55.0	11 04 25.0	19.40	19.40	19.40		8.5	7.2	159.9	BAT well, GW depth not available
18	BAV-2		Vigstein Farm	25.05.06	202.50	60 12 55.0	11 04 25.0	9.41	9.41	9.41		7.8	8.4	188.7	BAT well, GW depth not available

Calsium	Potassium	Magnesium	Sodium	Iron	Manganese	Barium	Strontium	Ammonium
mmol/l	mmol/l	mmol/l	mmol/l	mmol/l	mmol/l	mmol/l	mmol/l	mmol/l
0,4316	0,0373	0,0889	0,7003	0,0990	0,0013	0,0008	0,0006	0,0006
0,6587	0,0164	0,0975	0,1127	0,0107	0,0016	0,0004	0,0007	0,0004
0,9356	0,0202	0,0889	0,1057	0,0034	0,0002	0,0008	0,0009	0,0004
1,9137	0,4066	0,2592	0,2523	0,0376	0,0151	0,0020	0,0031	0,0000
3,0938	0,0445	0,2954	0,5611	0,0005	0,0007	0,0034	0,0042	0,0002
2,9441	0,0483	0,3250	0,2566	0,0066	0,0058	0,0046	0,0041	0,0000
3,4431	0,3606	0,6170	0,9221	0,3528	0,0559	0,0237	0,0054	0,0000
3,5679	0,1637	0,3661	0,5655	0,0039	0,0633	0,0140	0,0045	0,0000
3,5429	0,3171	0,6787	0,8569	0,5587	0,2039	0,0210	0,0057	0,0000
2,8194	0,1714	0,5430	0,7351	0,0029	0,4005	0,0018	0,0027	0,0000
3,5429	0,0384	0,2262	0,4132	0,0011	0,0002	0,0013	0,0030	0,0000
3,7425	0,0419	0,2328	0,4393	0,0009	0,0004	0,0024	0,0032	0,0000
4,0170	0,0754	0,3274	0,3523	0,0004	0,0002	0,0051	0,0038	0,0023
1,5369	0,0522	0,1374	0,2627	0,0039	0,0005	0,0023	0,0022	0,0004
1,9561	0,0289	0,1485	0,2875	0,0007	0,0002	0,0042	0,0024	0,0002
1,7989	0,0404	0,2221	0,2079	0,0116	0,0051	0,0021	0,0027	0,0021
0,7086	0,0312	0,1152	0,1122	0,0005	0,0007	0,0000	0,0005	0,0000
3,7176	0,0345	0,3710	0,1214	0,0005	0,0965	0,0018	0,0031	0,0003
2,1457	0,0506	0,7692	0,2819	0,0005	0,0004	0,0007	0,0031	0,0000
0,7884	0,0299	0,0987	0,1414	0,0005	0,0002	0,0000	0,0007	0,0000
0,7211	0,0353	0,0954	0,1705	0,0007	0,0002	0,0000	0,0005	0,0000
1,1552	0,0417	0,4114	0,1970	0,0005	0,0089	0,0036	0,0038	0,0000
0,6088	0,0355	0,0872	0,1401	0,0025	0,0020	0,0008	0,0010	0,0012
1,4596	0,0307	0,2209	0,2714	0,0034	0,0131	0,0026	0,0031	0,0006
0,9007	0,0355	0,1312	0,1448	0,0018	0,0555	0,0015	0,0010	0,0008
1,4147	0,1816	0,2427	0,1653	0,0770	0,0066	0,0009	0,0000	0,0228
0,4042	0,0903	0,2822	0,4437	0,0021	0,0016	0,0003	0,0016	0,0075
0,6612	0,0271	0,0814	0,1205	0,0016	0,0027	0,0000	0,0010	0,0016
0,7360	0,0192	0,0884	0,1918	0,0016	0,0260	0,0007	0,0017	0,0002

Well	Sulphate	Nitrate	Chloride	Bicarbonate	Nitrite	Fluoride	Bromide	Phosphate
	mmol/l	mmol/l	mmol/l	mmol/l	mmol/l	mmol/l	mmol/l	mmol/l
RB1	0.1530	0.0001	0.0468	1.6800	0.0000	0.0296	0.0000	0.0000
RB2	0.1572	0.0000	0.0434	1.2800	0.0000	0.0263	0.0000	0.0000
RB3	0.0854	0.0110	0.0426	1.8500	0.0000	0.0099	0.0000	0.0000
K1	0.5226	0.0002	0.5472	4.0000	0.0000	0.0224	0.0000	0.0000
FU1	0.2353	0.0014	1.3484	5.1100	0.0000	0.0064	0.0000	0.0000
TM1	0.2711	0.0009	0.1077	6.4750	0.0000	0.0085	0.0000	0.0000
TM2	0.0542	0.0000	0.2781	11.7750	0.0067	0.0061	0.0021	0.0000
TM3	0.1229	0.0108	0.3024	7.7000	0.0031	0.0064	0.0012	0.0000
TM4	0.0664	0.0000	0.3378	12.3500	0.0070	0.0025	0.0012	0.0000
TM5	0.3945	0.0841	0.1523	7.8890	0.0026	0.0058	0.0010	0.0000
TM6	0.2696	0.0306	0.1213	6.6500	0.0000	0.0035	0.0000	0.0000
TM7	0.2748	0.0210	0.1464	7.2800	0.0000	0.0083	0.0000	0.0000
TM8	0.2301	0.0210	0.1693	7.4500	0.0000	0.0081	0.0000	0.0000
TW1	0.1437	0.0066	0.2502	2.9500	0.0000	0.0344	0.0000	0.0000
TW2	0.1145	0.0226	0.0779	3.7000	0.0000	0.0234	0.0000	0.0022
TE1	0.2269	0.0000	0.1805	3.2800	0.0000	0.0138	0.0006	0.0000
GE1	0.1322	0.0000	0.0750	1.5800	0.0000	0.0222	0.0000	0.0009
GE2	0.2020	0.0027	0.0485	8.7000	0.0000	0.0065	0.0000	0.0000
GE3	0.4102	0.0012	0.1518	9.0000	0.0000	0.0103	0.0024	0.0008
GE4	0.1405	0.0000	0.0339	1.5500	0.0000	0.0229	0.0000	0.0052
GE5	0.1301	0.0004	0.0330	1.5400	0.0000	0.0142	0.0000	0.0040
GW1	0.0030	0.0000	0.0767	2.4000	0.0000	0.1205	0.0000	0.0000
GW2	0.1530	0.0000	0.0367	1.1600	0.0000	0.0000	0.0000	0.0000
BAR-1	0.1530	0.0000	0.3188	2.9200	0.0000	0.0087	0.0000	0.0000
BAR-2	0.2332	0.0000	0.0996	1.6000	0.0000	0.0282	0.0000	0.0000
BAK-1	1.3637	0.0000	0.8293	1.3600	0.0000	0.0158	0.0007	0.0000
BAK-2	0.1093	0.0000	0.0347	1.6200	0.0000	0.0000	0.0000	0.0000
BAV-1	0.1884	0.0001	0.0717	1.1300	0.0000	0.0185	0.0000	0.0000
BAV-2	0.1718	0.0009	0.3639	1.0900	0.0017	0.0113	0.0000	0.0000

Well	SUM -	SUM +	E.B.	TDS	EC / 100
	meq/l	meq/l	%	mg/l	
RB1	-2.06	1.98	-0.02	59.69	1.73
RB2	-1.64	1.67	0.01	49.92	1.57
RB3	-2.07	2.19	0.03	53.85	2.02
K1	-5.59	5.12	-0.04	178.19	4.82
FU1	-6.93	7.40	0.03	217.34	6.69
TM1	-7.13	6.89	-0.02	165.39	5.78
TM2	-12.16	10.28	-0.08	230.46	10.22
TM3	-8.26	8.77	0.03	200.19	6.98
TM4	-12.82	11.20	-0.07	255.20	10.33
TM5	-8.91	8.45	-0.03	216.06	7.37
TM6	-7.34	8.00	0.04	191.17	6.75
TM7	-8.00	8.45	0.03	201.12	7.25
TM8	-8.10	9.14	0.06	210.66	7.73
TW1	-3.49	3.68	0.03	97.48	3.32
TW2	-4.03	4.54	0.06	106.37	3.84
TE1	-3.91	4.34	0.05	113.85	3.88
GE1	-1.92	1.79	-0.03	50.95	1.93
GE2	-9.16	8.54	-0.03	189.42	8.26
GE3	-9.97	6.17	-0.24	158.89	8.83
GE4	-1.86	1.95	0.02	54.13	1.80
GE5	-1.83	1.84	0.00	50.94	1.67
GW1	-2.48	3.41	0.16	68.99	4.78
GW2	-1.50	1.58	0.03	47.60	1.49
BAR-1	-3.54	3.71	0.02	99.02	3.40
BAR-2	-2.17	2.36	0.04	73.91	2.12
BAK-1	-4.92	3.85	-0.12	239.44	5.12
BAK-2	-1.87	1.93	0.01	49.05	1.81
BAV-1	-1.58	1.65	0.02	53.65	1.60
BAV-2	-1.80	1.92	0.03	68.33	1.89

Well	Oxygen	Temp.	Full Sat.	Screen A.	Pressure	Sat.
	ml / l	°C	ml/l	m.a.s.l.	mm Hg	%
RB1	0.21	10.20	7.984	169.00	744.06	2.75
RB2	0.04	8.80	8.248	177.00	743.30	0.56
RB3	0.91	9.20	8.172	186.05	742.45	11.44
K1	0.72	6.70	8.663	187.50	742.31	8.47
FU1	2.02	4.60	9.122	173.00	743.68	22.63
TM1	0.04	8.80	8.248	170.75	743.89	0.44
TM2	0.00	9.70	8.077	175.50	743.44	0.00
TM3	0.04	9.80	8.058	172.00	743.77	0.57
TM4	0.00	6.20	8.768	178.00	743.21	0.00
TM5	0.21	9.30	8.153	180.00	743.02	2.58
TM6	2.54	9.70	8.077	169.00	744.06	32.17
TM7	1.24	9.80	8.058	172.50	743.73	15.67
TM8	0.77	9.30	8.153	175.00	743.49	9.66
TW1	2.08	6.20	8.768	154.00	745.47	24.16
TW2	4.85	8.80	8.248	169.00	744.06	60.01
TE1	1.50	7.00	8.600	137.52	747.03	17.80
GE1	0.54	8.20	8.362	174.12	743.57	6.57
GE2	0.51	9.20	8.172	192.42	741.85	6.40
GE3	0.39	7.80	8.440	190.10	742.07	4.78
GE4	0.50	7.50	8.500	171.60	743.81	6.03
GE5	0.42	7.90	8.420	161.21	744.79	5.10
GW1	0.47	7.80	8.440	182.87	742.75	5.76
GW2	0.00	6.10	8.789	172.00	743.77	0.00

Well	Silica
	mmol/l
RB1	0.1332
RB2	0.1584
RB3	0.1919
K1	0.2136
FU1	0.1065
TM1	0.1581
TM2	0.1289
TM3	0.2378
TM4	0.0666
TM5	0.1018
TM6	0.2044
TM7	0.2083
TM8	0.2439
TW1	0.1542
TW2	0.1880
TE1	0.1666
GE1	0.0716
GE2	0.1339
GE3	0.0951
GE4	0.0474
GE5	0.0527
GW1	0.2111
GW2	0.1449
BAR-1	0.1908
BAR-2	0.1606
BAK-1	0.2247
BAK-2	0.1271
BAV-1	0.1624
BAV-2	0.1463

Well	TIC	NPOC	TC	TNb
	mg/l	mg/l	mg/l	mg/l
RB1	8.64	0.50	9.14	0.00
RB2	6.19	0.49	6.68	0.00
RB3	6.56	0.52	7.08	0.00
K1	15.14	0.81	15.96	0.00
FU1	30.27	0.44	30.71	0.14
TM1	29.46	1.32	30.77	0.38
TM2	44.35	5.93	50.28	6.59
TM3	26.91	6.28	33.19	2.89
TM4	33.93	3.58	37.51	0.82
TM5	31.91	3.05	34.96	0.00
TM6	27.41	1.10	28.52	0.25
TM7	22.68	1.15	23.83	0.41
TM8	29.00	1.20	30.20	5.77
TW1	10.47	1.09	11.56	0.00
TW2	12.41	0.55	12.96	0.10
TE1	12.13	0.57	12.70	0.02
GE1	6.66	0.48	7.15	0.00
GE2	40.27	0.80	41.07	0.78
GE3	25.62	0.86	26.48	0.00
GE4	7.18	0.55	7.74	0.00
GE5	7.80	0.48	8.27	0.00
GW1	9.55	2.19	11.74	0.00
GW2	NA	NA	NA	NA
BAR-1	17.32	0.78	18.10	0.00
BAR-2	9.14	0.58	9.72	0.00
BAK-1	6.29	2.52	8.81	0.00
BAK-2	9.47	1.43	10.90	0.00
BAV-1	6.44	0.66	7.10	0.00
BAV-2	6.50	0.47	6.97	0.00

Appendix C: Chromatograms

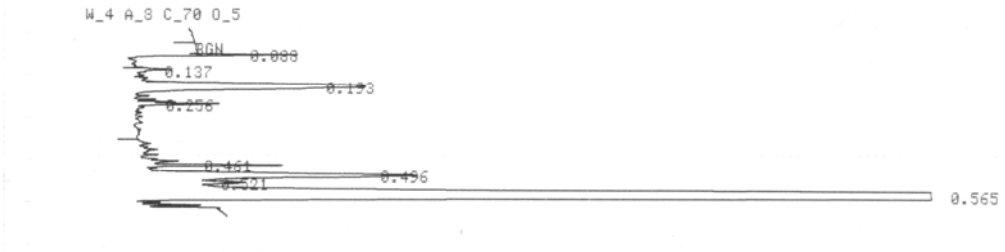

RUN 1.1: TM8

RUN 1.2: TM8

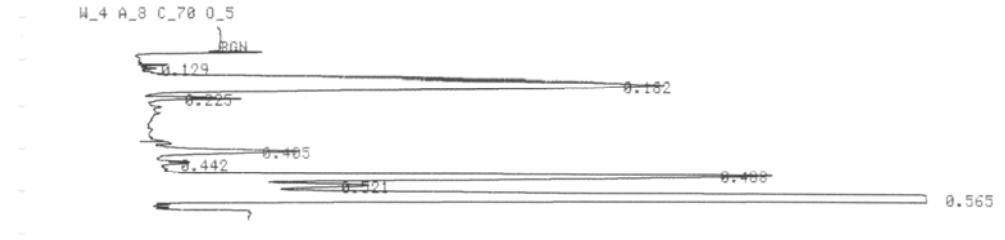

RUN 1.3: K1

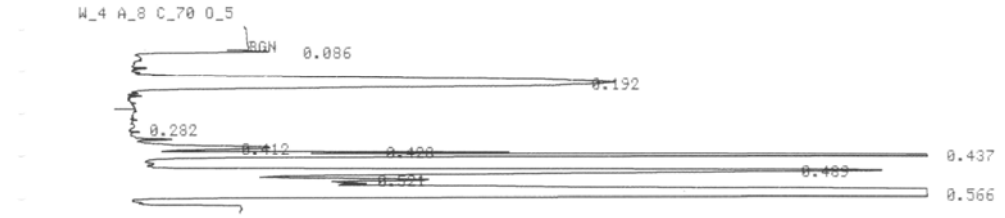

RUN 1.4: K1

RUN 1.5: TM7

RUN 1.6: TM7

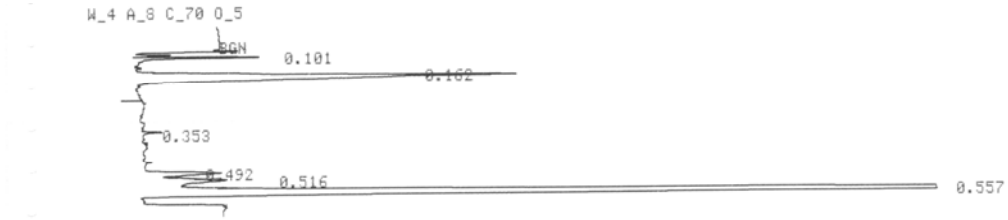

RUN 1.7: RB2

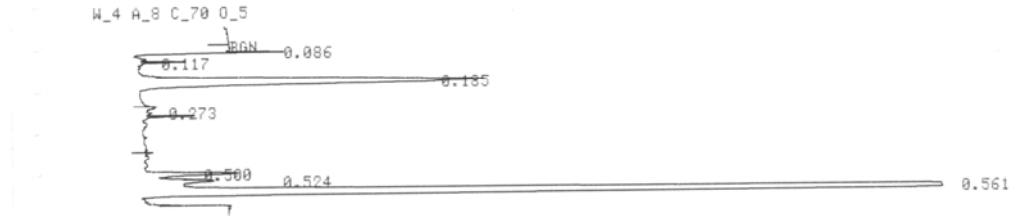

RUN 1.8: RB2

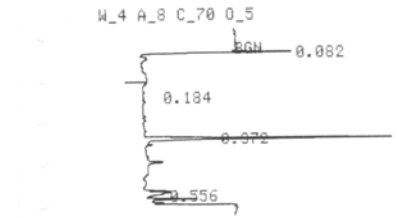

RUN 1.9: BLANC

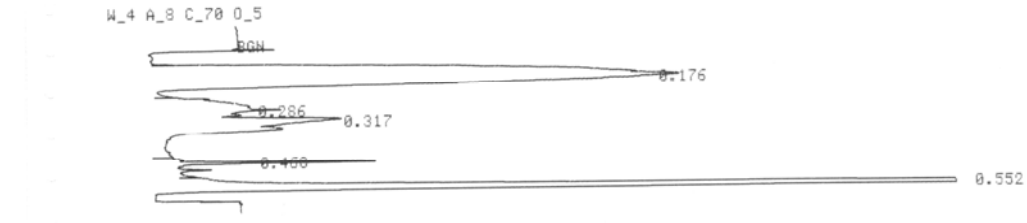

RUN 1.10: Standard NSO

RUN 2.1: TW1

RUN 2.2: TW1

RUN 2.3: TW2

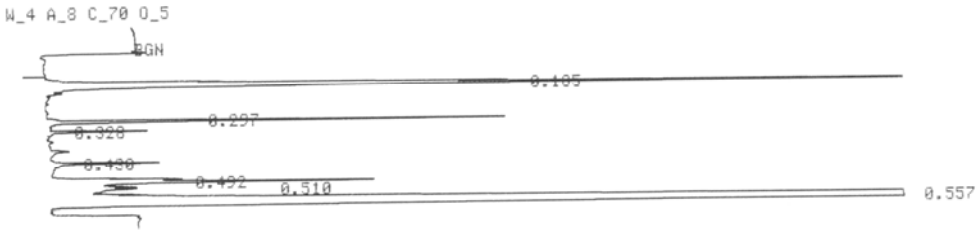

RUN 2.4: TW2

RUN 2.5: TE1

RUN 2.6: TE1

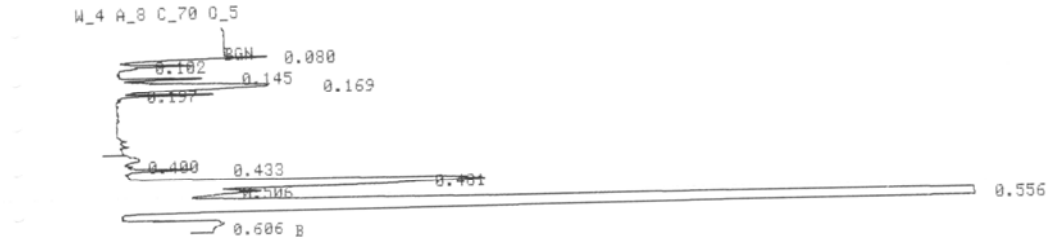

RUN 2.7: TM6

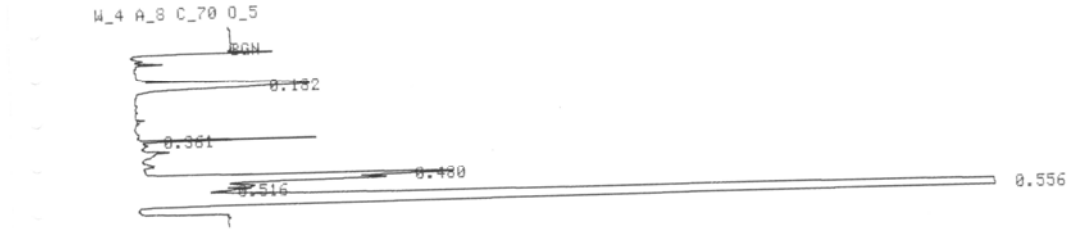

RUN 2.8: TM6

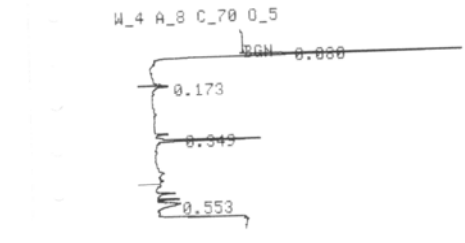

RUN 2.9: BLANC

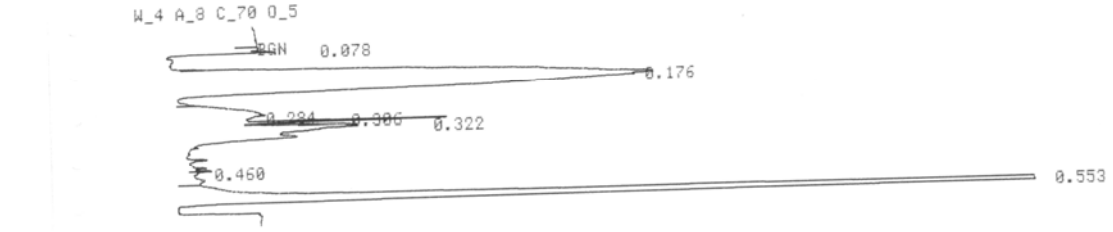

RUN 2.10: Standard NSO

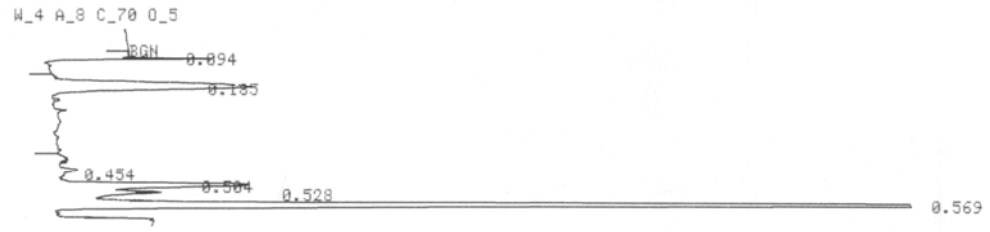

RUN 3.1: RB3

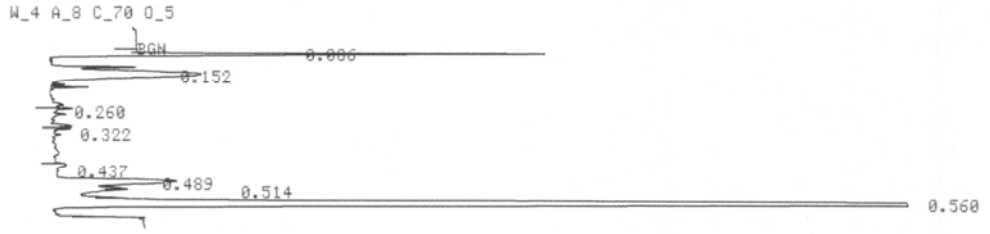

RUN 3.2: RB3

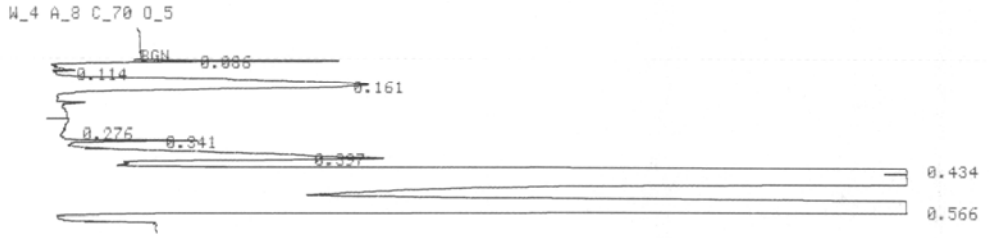

RUN 3.3: RB1

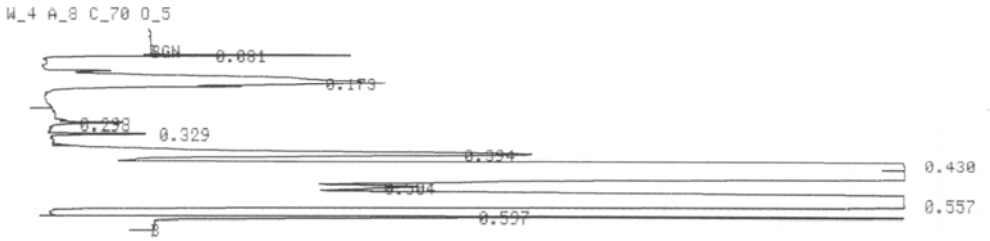

RUN 3.4: RB1

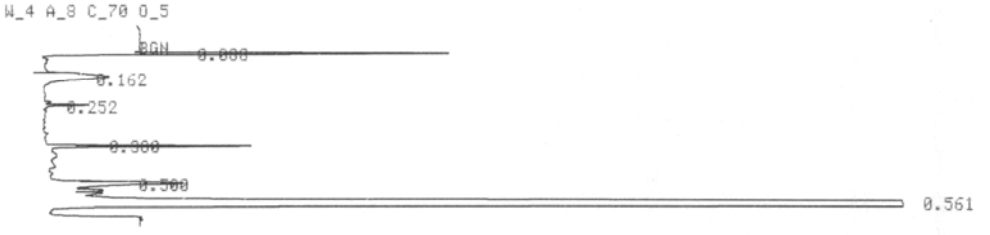

RUN 3.5: GE2

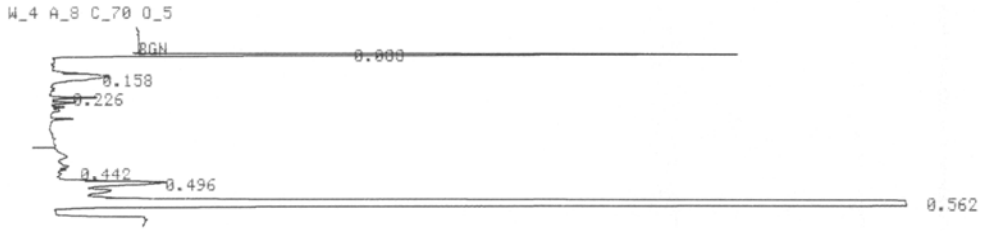

RUN 3.6: GE2

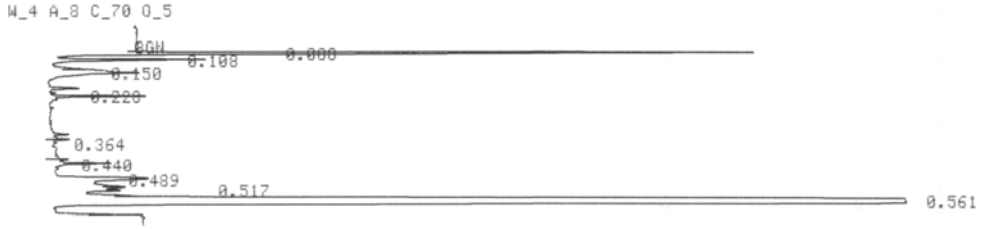

RUN 3.7: TW2

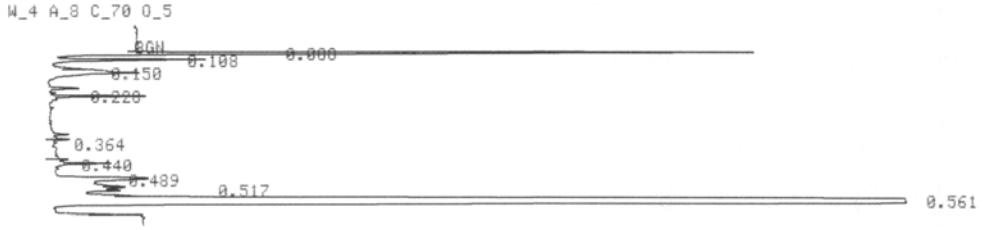

RUN 3.8: TE1

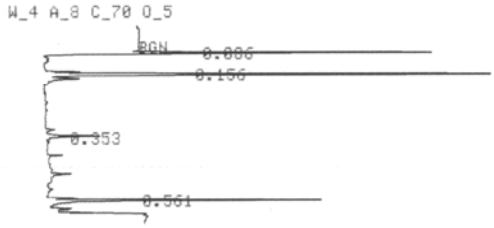

RUN 3.9: BLANC

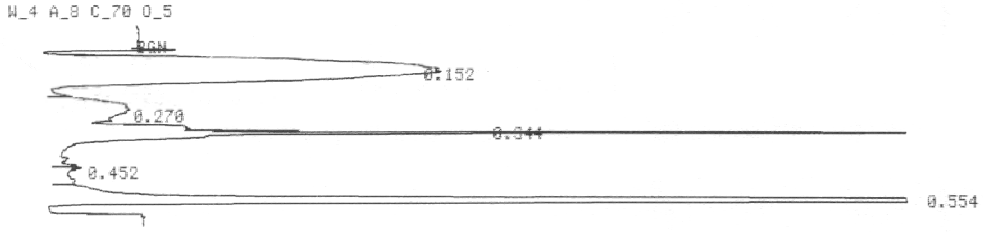

RUN 3.10: Standard NSO

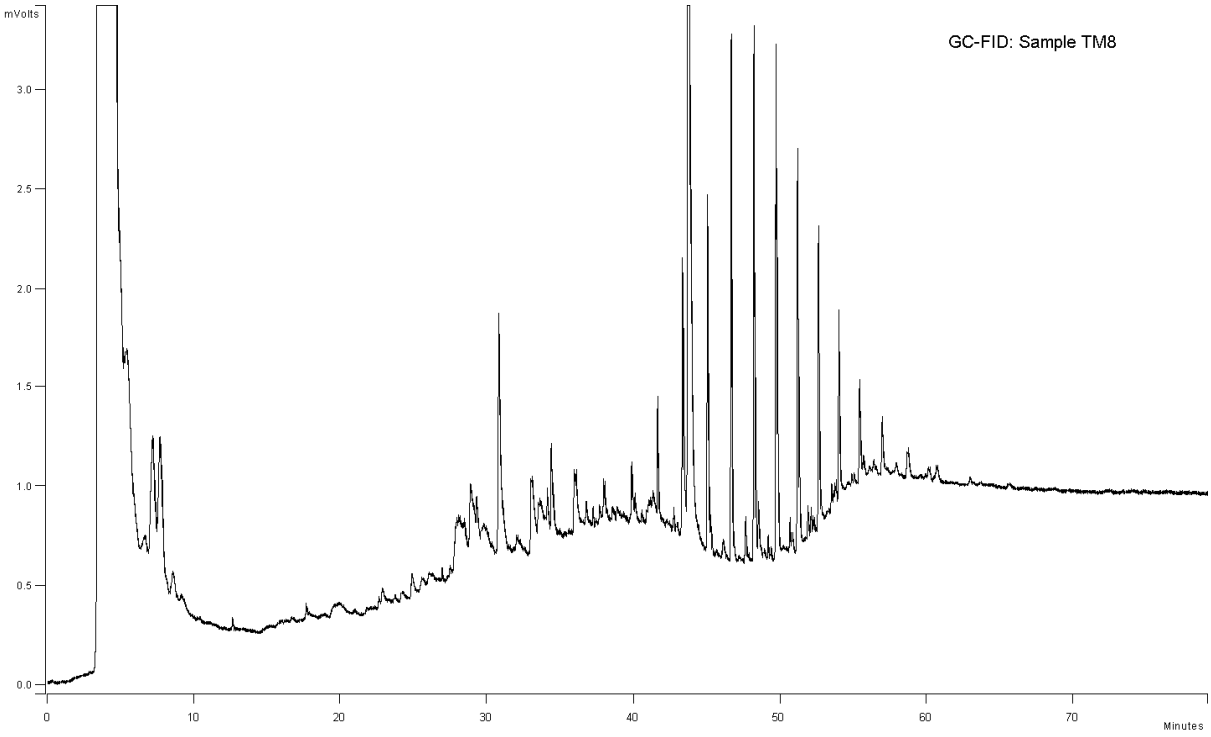
GC-FID: Sample TM8
mVolts
3.0
2.5
2.0
1.5
1.0
0.5
0.0
0
10
20
30
40
50
60
70
Minutes

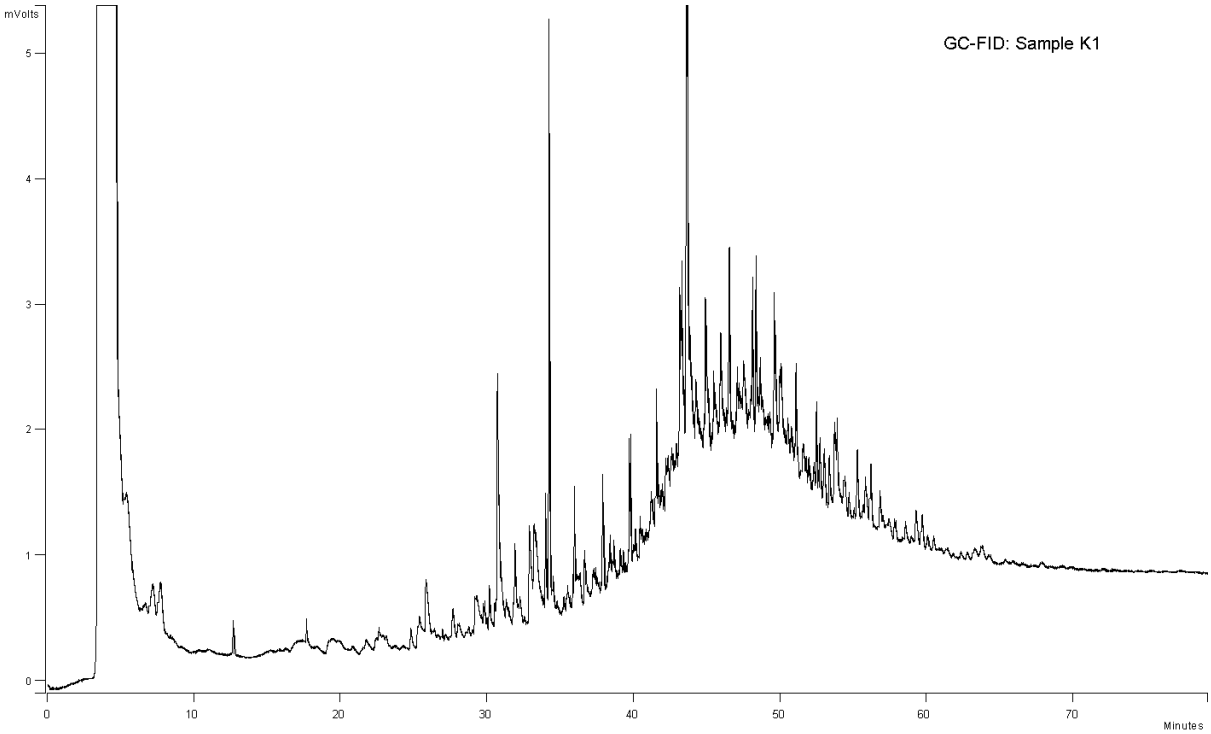
GC-FID: Sample K1
mVolts
5
4
3
2
1
0
0
10
20
30
40
50
60
70
Minutes

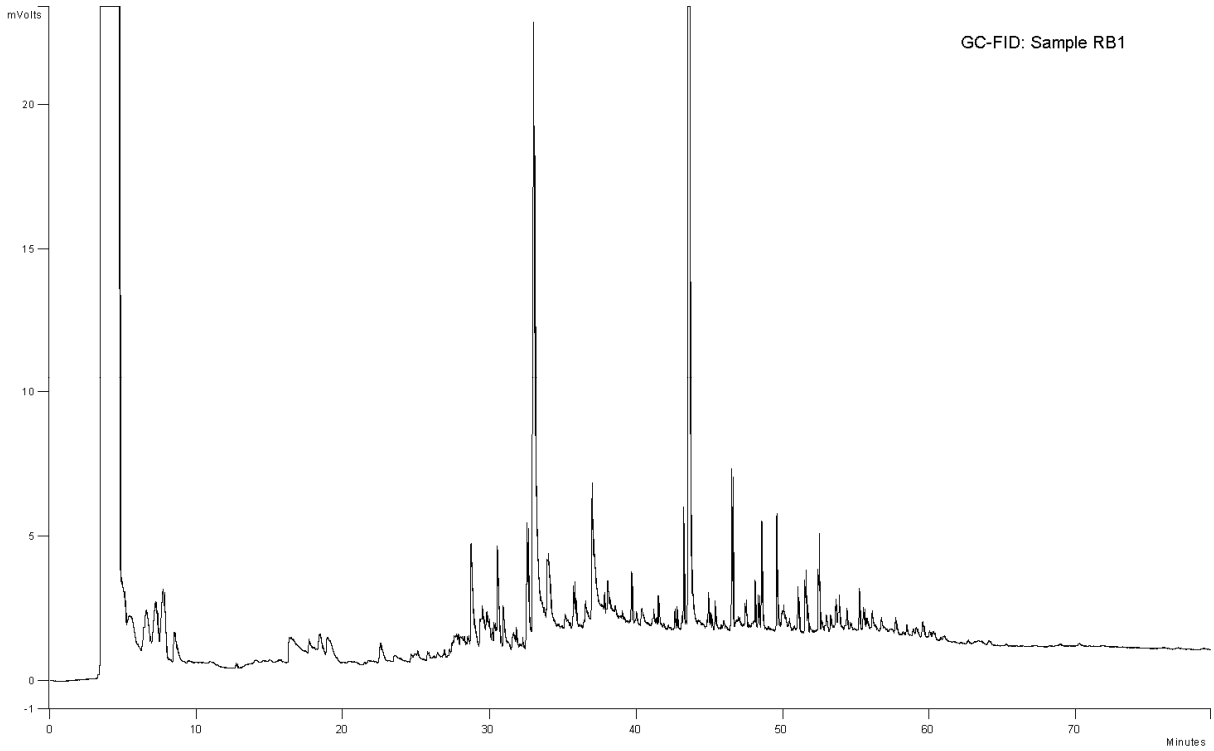
GC-FID: Sample RB1
mVolts
20
15
10
5
0
-1
0
10
20
30
40
50
60
70
Minutes

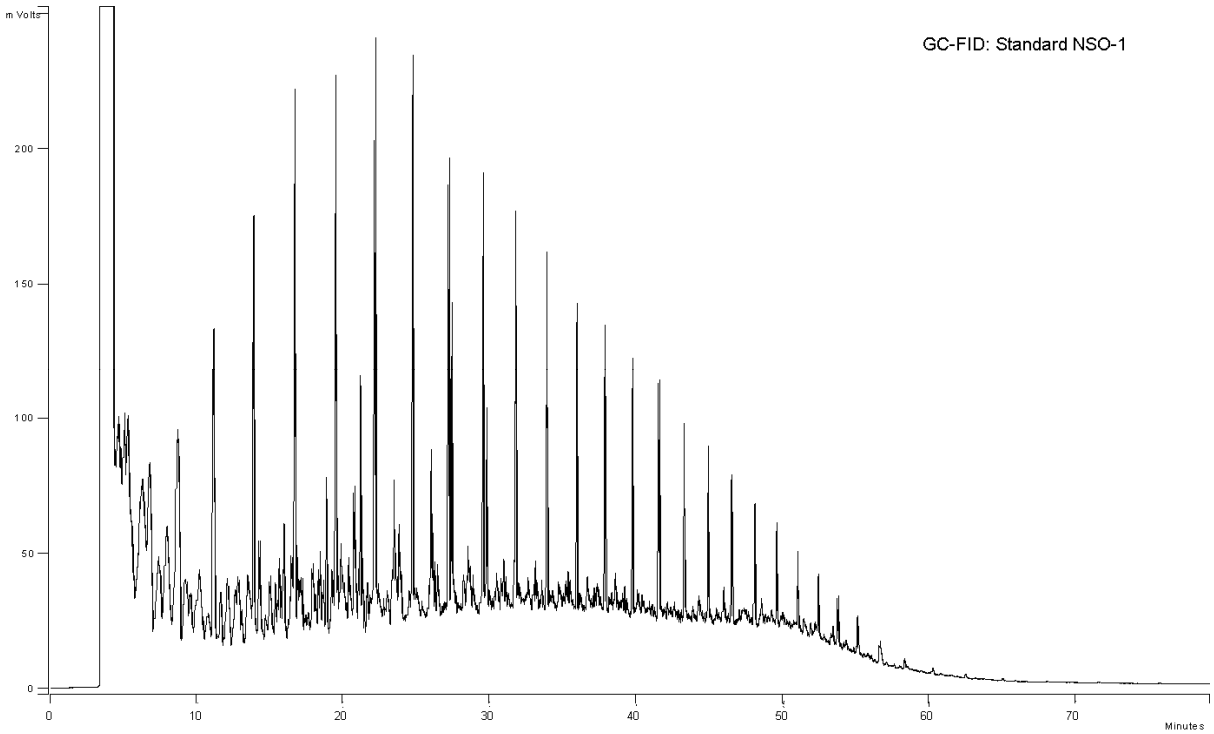
GC-FID: Standard NSO-1
mVolts
200
150
100
50
0
0
10
20
30
40
50
60
70
Minutes

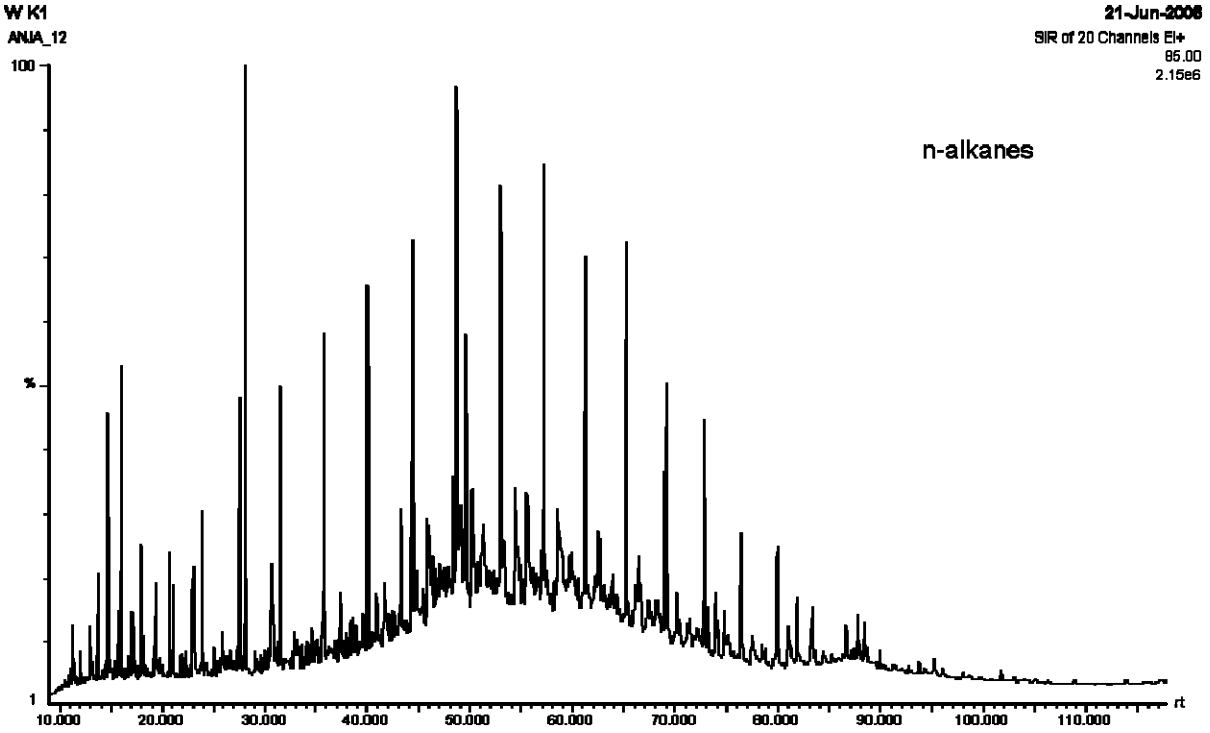
W K1
ANJA_12
21-Jun-2006
SIR of 20 Channels EI+
85.00
2.15e6
n-alkanes
100
%
1
10.000
20.000
30.000
40.000
50.000
60.000
70.000
80.000
90.000
100.000
110.000
rt

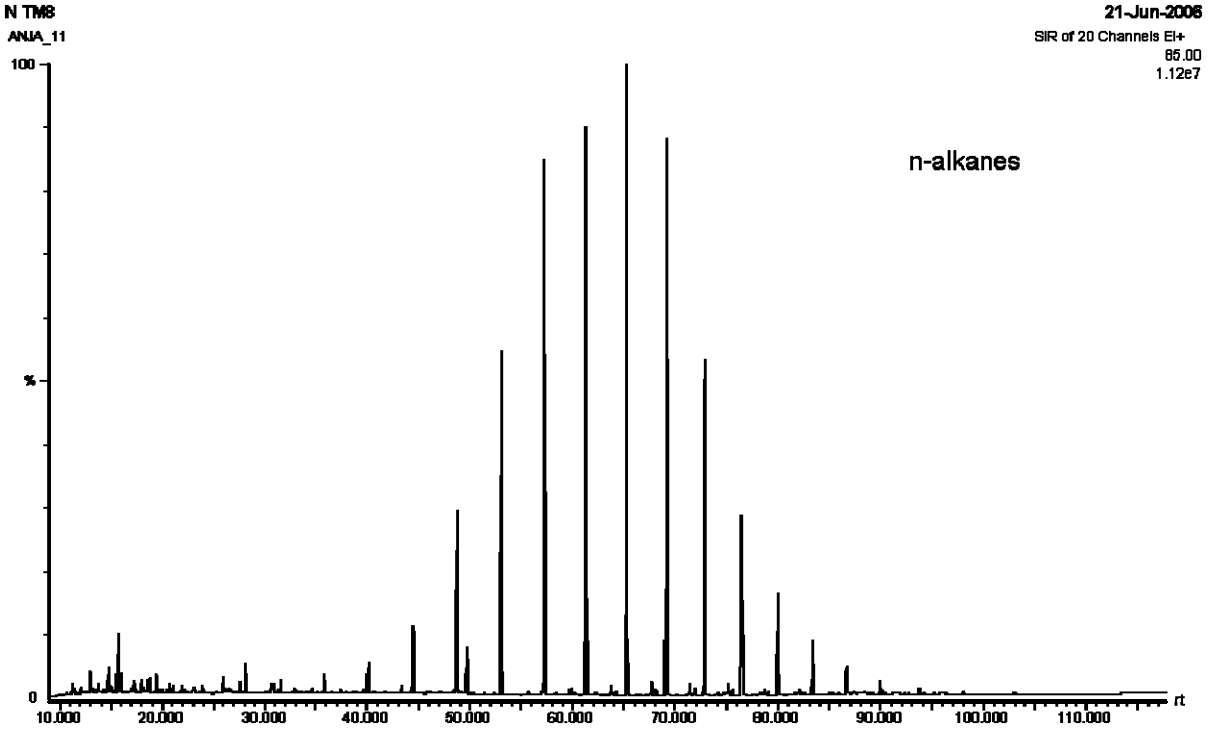
N TMS
ANJA_11
21-Jun-2006
SIR of 20 Channels EI+
85.00
1.12e7
n-alkanes
100
%
0
10.000
20.000
30.000
40.000
50.000
60.000
70.000
80.000
90.000
100.000
110.000
rt

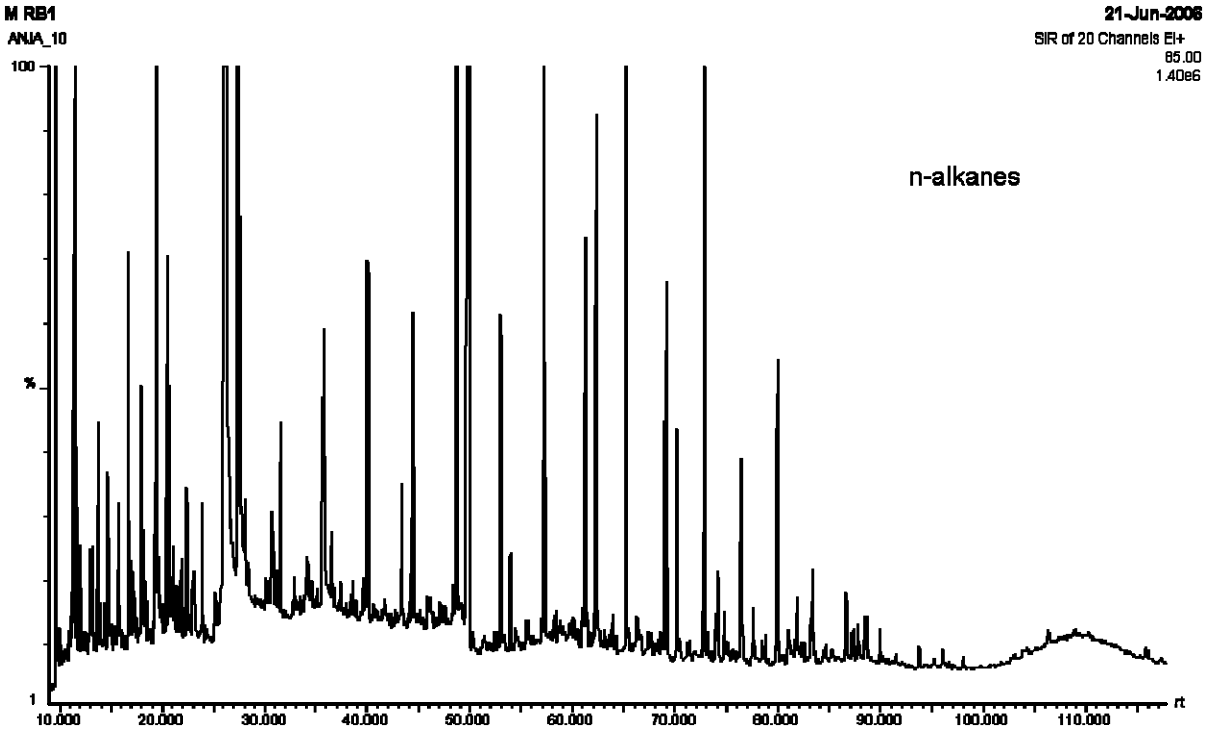
M RB1
ANJA_10
21-Jun-2006
SIR of 20 Channels EI+
85.00
1.40e6
n-alkanes
100
%
1
10.000
20.000
30.000
40.000
50.000
60.000
70.000
80.000
90.000
100.000
110.000
rt

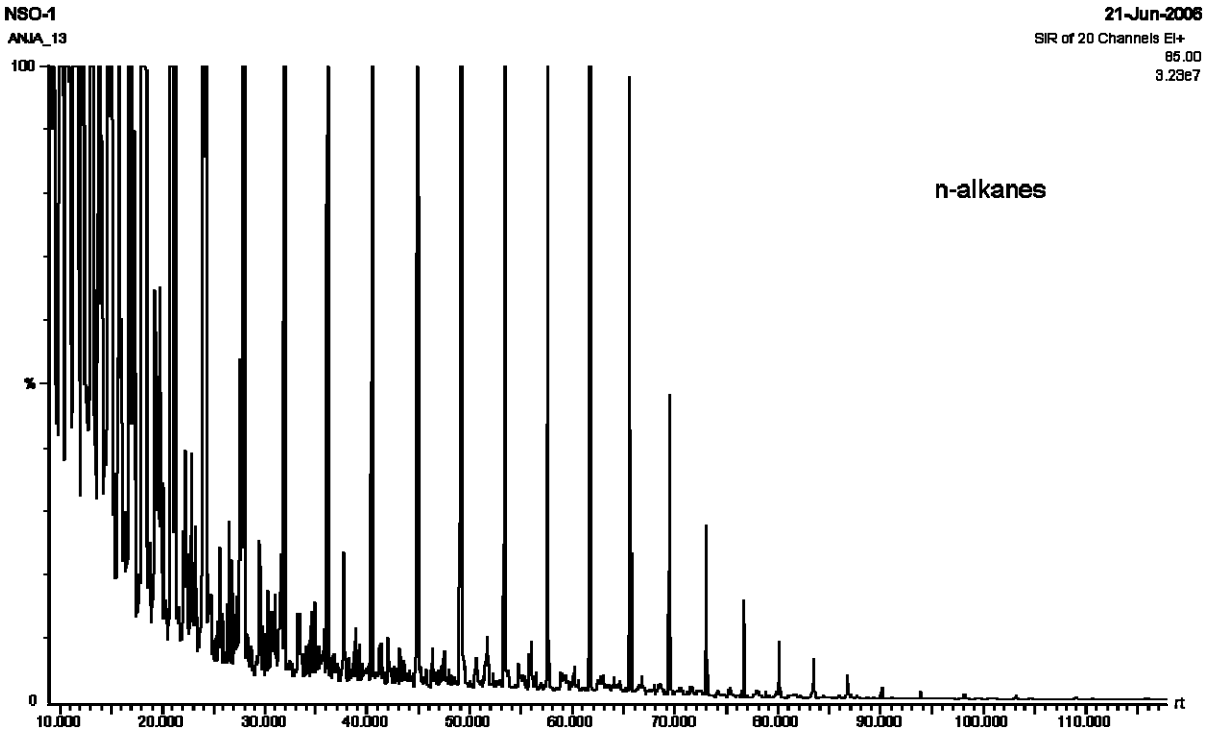
NSO-1
ANJA_13
21-Jun-2006
SIR of 20 Channels EI+
85.00
3.23e7
n-alkanes
100
%
0
10.000
20.000
30.000
40.000
50.000
60.000
70.000
80.000
90.000
100.000
110.000
rt

Appendix D: PHREEQC

```
TITLE Input (rain) to output (Risa)

SOLUTION 1                      #Rainwater
units mmol/kgw
temp 6.0
pH 4.3
Cl 0.016
S(6) 0.025
Na 0.015
K 0.004
Ca 0.005
Mg 0.0
Alkalinity 0.0
Si 0.0
Fe(+2) 0.0
Al 0.0

SOLUTION 2                      #Risa
units mmol/kgw
temp 6
pH 7.71
Cl 0.08
S(6)  0.13
Na 0.14
K 0.03
Ca 0.78
Mg 0.12
Alkalinity 1.60
Si 0.0
Fe(+2) 0.0
Al 0.0

INVERSE_MODELING 1
-solutions 1 2
-uncertainty 0.05               #default uncertainty: 0.05 = 5%
-phases                         #possibly reacting phases
    Calcite         dis
    Chlorite(14A)   dis
    K-feldspar      dis
    K-mica          dis
    Pyrite          dis         #pyrite oxidation
    Halite          dis         #mixing with fossil seawater
    CO2(g)          dis
    O2(g)           dis
    Kaolinite       precip
    Plagioclase     dis
```

```
    Ca-montmorillonite precip
    Fe(OH)3(a)      precip
    chalcedony      precip

-balances
K 0.25 - 0.25                   #increased uncertainty bco low conc.

PHASES
    Calcite
        Ca0.975Mg0.025CO3 = CO3-2 + 0.975Ca+2 + 0.025Mg+2
        log_k -8.48
        delta_h -2.297 kcal
        -analytical_expression -171.9065 -0.077993 2839.319 71.595

    Chlorite(14A)
        Mg2.15Fe2.3Al2.7Si2.75O10(OH)8 + 17H+ = 2.15Mg+2 + 2.3Fe+2 +
2.7Al+3 + 2.75H4SiO4 + 7H2O
        log_k 68.38
        delta_h -151.494 kcal

    Plagioclase
        Na0.7Ca0.3Al1.3Si2.7O8 + 5.2 H+ + 2.8H2O = 0.7Na+ + 0.3Ca+2 +
1.3Al+3 + 2.7H4SiO4
        log_k  0.0
END
```

Well	Screen A.	Mod.	Uncertainty	Calcite	Chlorite	K Feldsp.	K Mica	Pyrite	Halite	CO2	O2	Kaolinite	Plag.	Ca Mont.	Fe(OH)	Chal.
	m			mol/l	mol/l	mol/l	mol/l	mol/l	mol/l	g	g	mol/l	mol/l	mol/l	mol/l	mol/l
RB1	36.00	4		2.80E-04	3.86E-05		3.60E-05	6.19E-05	3.40E-05	1.34E-03	2.29E-04		9.30E-04	-6.10E-04	-5.07E-05	-3.57E-04
RB2	28.00	5		6.25E-04	3.92E-05		1.60E-05	6.69E-05	2.40E-05	7.65E-04	2.71E-04	-1.48E-04	1.09E-04		-1.47E-04	
RB3	18.95	1		8.82E-04	3.16E-05	1.60E-05		3.19E-05	2.40E-05	1.66E-03	1.37E-04	-1.22E-04	1.09E-04		-1.01E-04	
K1	15.00	1	Cl - 50%	2.12E-03	9.63E-05	3.49E-04	8.28E-05	2.48E-04	2.48E-04	2.77E-03	9.76E-04			-3.68E-04	-4.30E-04	
FU1	30.00	2	Cl - 51%	2.51E-03	1.10E-04		3.60E-05	1.08E-04	5.20E-04	3.10E-03	4.66E-04	-2.51E-04	7.46E-05		-3.61E-04	
TW1	19.70	1		1.49E-03	4.78E-05	4.60E-05		5.69E-05	2.30E-04	1.53E-03	2.41E-04	-1.13E-04	3.97E-05		-1.67E-04	
TW2	16.80	4		1.82E-03	4.41E-05		2.60E-05	4.33E-05	6.40E-05	2.155e-3	1.88E-04	-1.06E-04	2.75E-04	-1.47E-04	-1.45E-04	
TE1	39.48	1		1.74E-03	7.84E-05	4.15E-05		1.13E-04	1.64E-04	2.319e-3	4.666e-4	-1.65E-04	5.93E-05		-2.83E-04	
GE1	32.27	4		7.50E-04	4.71E-05		2.60E-05	5.19E-05	6.40E-05	8.06E-04	2.22E-04	-1.34E-04	4.83E-05		-1.60E-04	
GE2	12.30	3		3.98E-03	1.29E-04		2.60E-05	8.69E-05	3.40E-05	6.42E-03	4.00E-04	-2.63E-04	1.01E-04	-1.38E-05	-3.83E-04	
GE3	14.58	3	HCO3, SO4 - 25%	2.72E-03	4.160e-4		4.60E-05	1.69E-04	1.34E-04	5.18E-03	8.73E-04	-5.93E-04	1.87E-04	-1.36E-04	-1.13E-03	
GE4	33.11	5		7.43E-04	3.79E-05		2.60E-05	5.69E-05	1.40E-05	9.03E-04	2.35E-04	-4.20E-05	1.59E-04	-1.30E-04	1.44E-04	
GE5	43.41	5		6.96E-04	3.84E-05		3.60E-05	5.19E-05	1.40E-05	8.56E-04	2.17E-04	-3.34E-05	2.01E-04	-1.75E-04	-1.40E-04	
GW2	35.00	4		5.58E-04	3.54E-05		3.60E-05	6.19E-05	2.40E-05	7.07E-04	2.52E-04	-1.40E-04	1.44E-04	-4.76E-05	-1.43E-04	
BAR-1	13.78	1	Cl - 30%	1.39E-03	8.61E-05	2.86E-05		6.25E-05	2.04E-04	3.78E-03	2.84E-04	-1.90E-04	9.18E-05		-2.61E-04	
BAR-2	25.50	1		8.63E-04	5.04E-05	3.77E-05		1.02E-04	8.40E-05	9.68E-04	4.11E-04	-1.25E-04	5.86E-05		-2.18E-04	
BAK-1	8.98	6	Cl - 90%	1.47E-03	9.45E-05		2.21E-04	6.34E-05	6.14E-05	2.06E-03	2.41E-03	-5.54E-04	1.46E-04		-7.71E-04	
BAK-2	33.20	2	Fe - 30%	3.01E-04	1.20E-04		6.35E-05	4.25E-05	1.40E-05	1.63E-03	2.07E-04	-5.02E-05	5.56E-04	-4.88E-05	-2.31E-04	
BAV-1	19.40	1		6.28E-04	2.99E-05	2.83E-05		8.19E-05	5.40E-05	7.03E-04	3.24E-04	-1.02E-04	7.29E-05		-1.51E-04	
BAV-2	9.41	1	Cl - 51%	6.60E-04	3.27E-05	1.60E-05		8.10E-05	1.42E-04	5.31E-04	3.23E-04	-1.00E-04	7.39E-05		-1.56E-04	
Budget		2		7.74E-04	4.68E-05		2.60E-05	5.19E-05	6.40E-05	9.15E-04	2.215e-4	-5.08E-05	8.714e-5	-9.28E-05	-1.60E-04	

Appendix E: Isotope Data

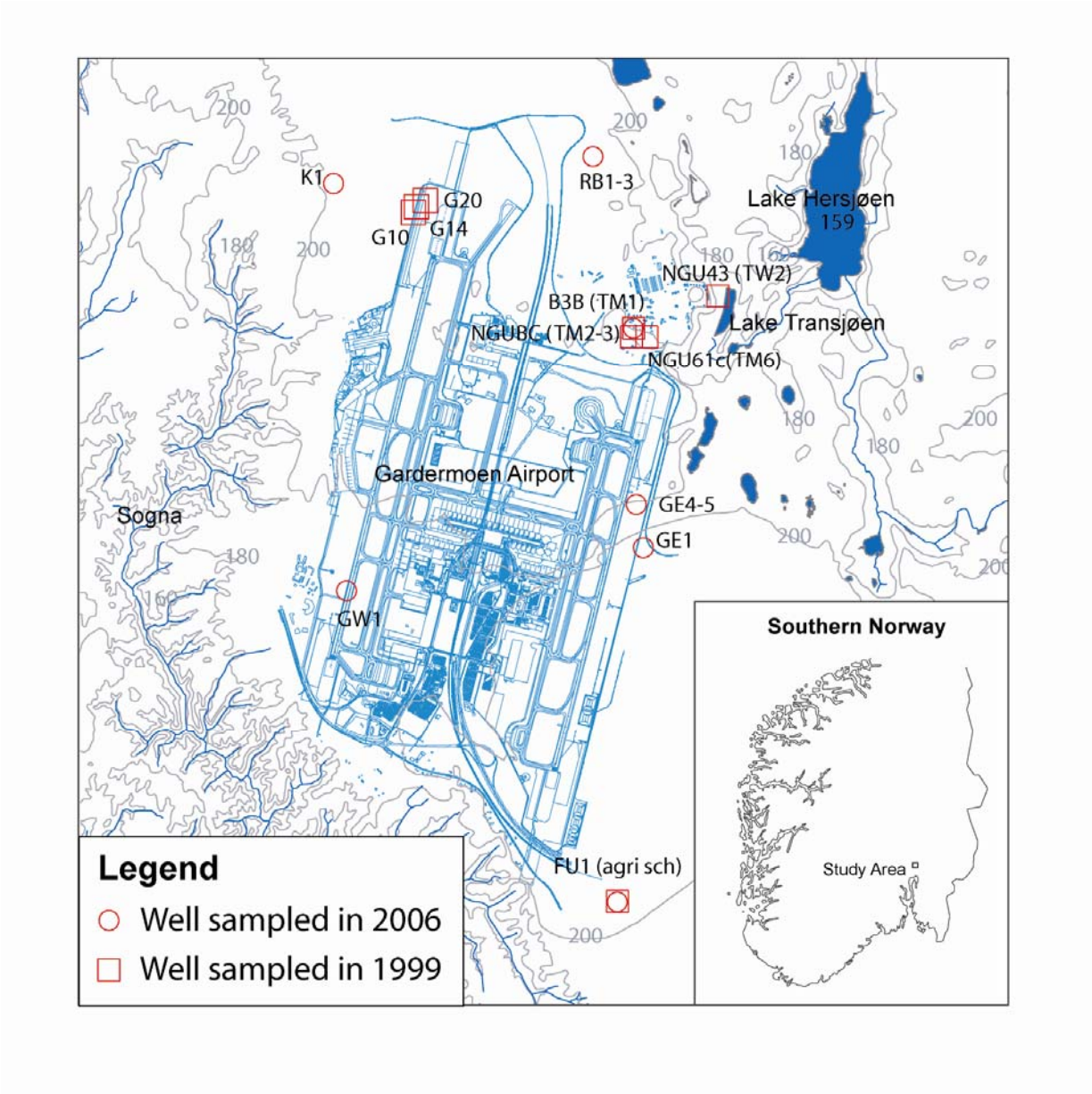
K1
G20
G14
G10
RB1-3
Lake Hersjøen
159
NGU43 (TW2)
B3B (TM1)
NGUBC (TM2-3)
Lake Transjøen
NGU61c(TM6)
Gardermoen Airport
Sogna
GE4-5
GE1
GW1
FU1 (agri sch)
Legend
Well sampled in 2006
Well sampled in 1999
Southern Norway
Study Area
200
180
160

Sample NO	Well Name	Place	Coord. N	Coord. E	Screen T.	Screen B.	Screen A.	GW depth	Temp.	pH	E.C.
					m	m	m	m	celcius		microS/cm
1	agri sch (FU1)	Furusmo	60 09 55.6	11 06 55.6	31.00	29.00	30.00	~8.00	5.3	7.8	211.0
1	duplicate	Furusmo	60 09 55.6	11 06 55.6	31.00	29.00	30.00	~8.00	5.3	7.8	211.0
2	G20 (GW2)	Gardermoen A., West	60 13 06.9	11 05 19.9	34	36	35	4.20	3.70	5.90	54.30
3	NGU62_c (TM2)	Trandum Landfill	60 12 34.3	11 07 13.3	20.20	21.20	20.70	17.00	10.2	6.7	83.2
3	NGU62_b (TM3)	Trandum Landfill	60 12 34.3	11 07 13.3	23.20	25.20	24.20	17.00	NA	NA	NA
4	NGU B3B (TM1)	Trandum Landfill	60 12 35.5	11 07 16.1	21.37	24.87	23.12	14.00	9.1	7.3	611.0
5	NGU61_c (TM6)	Trandum Landfill	60 12 32.0	11 07 26.1	16.50	18.50	17.50	9.50	7.9	7.4	
6	G14	Moreppen	60 13 05.9	11 05 22.1	5.00	6.00	5.50	4.50	7.6	6.2	36.6
7	G10	Moreppen	60 13 03.6	11 05 22.7	5.00	6.00	5.50	4.50	7.7	NA	NA
8	NGU43 (TW2)	Lake Transjøen, West	60 12 52.2	11 07 50.5	14.80	18.80	16.80	13.80	8.2	7.4	93.2
9	NGU21	Trandum Landfill	60 12 39.3	11 07 13.4	27.00	32.50	29.75	26.00	9.4	7.1	421.0

Sample NO	Well name	Place	Date	Sample-No	T	4He	err4He	3He/4He	err3He/4He	3He	err3He
					°C	ccSTP/g	ccSTP/g			ccSTP/g	ccSTP/g
1	agri sch	Furusmo	03.05.1999	251	5.3	8.2851E-08	2.38995E-10	2.09663E-06	5.57553E-09	1.73708E-13	6.81521E-16
1	agri sch	Furusmo	03.05.1999	247	5.3	1.09E-07	4.67431E-10	2.12839E-06	3.55396E-09	2.31996E-13	1.06764E-15
2	G20	Moreppen	04.05.1999	248	3.7	5.2474E-08	1.44211E-10	1.38611E-06	5.20573E-09	7.27349E-14	3.38492E-16
3	NGU62c	Trandum	04.05.1999	72	10.2	5.8713E-08	2.53901E-10	1.35514E-06	4.39766E-09	7.9564E-14	4.30177E-16
3	NGU62b	Trandum	04.05.1999	35		5.7912E-08	2.48317E-10	1.52642E-06	4.7338E-09	8.83988E-14	4.67787E-16
4	NGU B3B	Trandum	04.05.1999	473	9.1	7.4722E-08	7.31292E-10	1.27115E-06	3.71414E-09	9.49827E-14	9.70124E-16
5	NGU61c	Trandum	04.05.1999	97	7.9	7.264E-08	3.11273E-10	1.37157E-06	4.11422E-09	9.96307E-14	5.21141E-16
6	G14	Moreppen	06.05.1999	244	7.6	5.2958E-08	2.27748E-10	1.38302E-06	4.3139E-09	7.32411E-14	3.89105E-16
7	G10	Moreppen	06.05.1999	291	7.7	5.5767E-08	2.39466E-10	1.37497E-06	4.32962E-09	7.66778E-14	4.083E-16
8	NGU43	Trandum	06.05.1999	162	8.2	5.9511E-08	2.56092E-10	1.41397E-06	3.90779E-09	8.41465E-14	4.30351E-16
9	NGU21	Trandum	13.08.1999	285	9.4	5.3326E-08	1.55972E-10	1.40678E-06	4.40773E-09	7.50177E-14	3.21544E-16

Sample NO	Ne	err Ne	20/22Ne	Ne/4He	err Ne/4He	Ar	Err Ar	40Ar/36Ar	Err 40Ar/36Ar	Kr	Err Kr
	ccSTP/g	ccSTP/g				cc/g	cc/g			cc/g	cc/g
1	2.9414E-07	1.9361E-09	9.764671419	3.55018569	0.0255141	0.00047491	2.376E-06	296.6131298	0.4846523	1.09649E-07	1.54072E-09
1	3.5741E-07	3.5312E-09	9.80103891	3.27897862	0.03531598						
2	2.1255E-07	2.2625E-09	9.824147755	4.05060315	0.04452948						
3	2.0464E-07	2.0219E-09	9.775171065	3.48552489	0.03759206						
3	1.9706E-07	1.9469E-09	9.787608887	3.40278765	0.03664726						
4	2.3656E-07	3.1297E-09	9.787608887	3.16586539	0.05209914						
5	2.5477E-07	2.5175E-09	9.785693316	3.50727496	0.0377756						
6	2.2653E-07	2.2389E-09	9.793360102	4.27758094	0.04610672						
7	2.3801E-07	2.3513E-09	9.796238245	4.26790607	0.04597303						
8	2.4006E-07	2.3719E-09	9.771350401	4.03391251	0.04347215						
9	2.3118E-07	1.5206E-09	9.805844283	4.33515669	0.03120763	0.00042893	2.04809E-06	295.8396239	0.40437406	1.04141E-07	1.44075E-09

Sample NO	Xe	Err Xe	Calc. T	err Calc. T	T, Sol.	?Ne	err ?Ne	?4He	err ?4He	4He rad	err 4He rad
	cc/g	cc/g	°C	°C	°C	%	%	%	%	cc/g	cc/g
1	1.6672E-08	2.0802E-10	4.25682	0.312385	4.25682	40.770671	0.92660365	77.57926106	0.512250214	1.16412E-08	6.07068E-10
1					4.25682	71.0526794	1.689980562	133.6266754	1.001870816	1.95534E-08	1.11999E-09
2					3.7	1.09650257	1.076095239	12.1209917	0.308134189	5.00832E-09	6.6786E-10
3					10.2	4.11108595	1.028643416	29.58822062	0.560401069	1.10764E-08	6.35688E-10
3					10.2	0.25449488	0.99045579	27.82203994	0.548075419	1.24612E-08	6.13633E-10
4					9.1	19.0725354	1.575339765	64.11240354	1.606140315	1.82697E-08	1.16126E-09
5					7.9	26.7143794	1.252128139	58.64424996	0.679817603	1.13708E-08	7.89558E-10
6					7.6	12.3279559	1.11020251	15.49150961	0.496680652	-6.23474E-11	6.84334E-10
7					7.7	18.1394481	1.167088652	21.67729301	0.522488308	-5.98047E-10	7.18765E-10
8					8.2	19.7614256	1.183267801	30.15738895	0.560102464	2.37139E-09	7.30031E-10
9	1.5425E-08	1.8964E-10	5.63184	0.265599	5.63184	12.3035115	0.738704372	15.14559365	0.336787327	-2.85702E-10	4.65211E-10

Sample NO	?4He rad	err ?4He rad	3He tri	err 3He tri	3H	err 3H	3H+3He tri	err 3H+3He tri	age	err age
	%	%	TU	TU	TU	TU	TU	TU	y	y
1	24.9513176	1.30116214	30.56701812	0.40964777	18.1439173	0.43047032	48.71093541	0.594235635	17.63852532	0.305399585
1	41.9098529	2.40053713	43.78427221	0.70167296	17.4219181	0.64340521	61.2061903	0.952005891	22.44214341	0.514363423
2	10.7012231	1.42700964	3.251203923	0.38221768	11.7243822	0.34167627	14.97558613	0.512672439	4.371384994	0.469647206
3	24.4474207	1.40306526	5.823436801	0.36245612	24.9469527	0.73958309	30.77038946	0.823624669	3.747167343	0.233033204
3	27.5038011	1.35438635	10.57800146	0.35965044	51.9829409	1.13658315	62.56094235	1.192128219	3.308232979	0.122075329
4	40.1258369	2.55047857	7.063028196	0.62620868	19.1320006	0.80478023	26.19502883	1.019710025	5.611919682	0.472586535
5	24.8338158	1.72438724	6.312547286	0.4485631	14.5008608	0.64834146	20.81340814	0.788387913	6.454618448	0.454780897
6	-0.13596913	1.49241645	0.388508462	0.38615985	13.7412606	0.57383154	14.12976906	0.691666148	0.497967248	0.488551324
7	-1.30487171	1.56826447	-0.087021407	0.40548305	13.7712432	0.60327846	13.68422178	0.726884727	-0.113220204	0.529257443
8	5.18649876	1.59666301	2.457599158	0.41199854	8.4292603	0.4415401	10.88685946	0.603904346	4.569580545	0.708135917
9	-0.61691267	1.00452288	0.783974606	0.27238946	52.2479948	0.86555638	53.03196944	0.907405022	0.2660048	0.091841894

Well	3/4He	20/22Ne	40/36Ar	He	Ne	Ar	Kr	Xe	T	h	p
				cc/g	cc/g	cc/g	cc/g	cc/g	celcius	m	atm
FU1	1.17E-06	9.777	295.7	7.88E-08	2.60E-07	5.02E-04	1.19E-07	1.89E-08	4.6	209	0.975
RB1	2.56E-06	9.777	296.1	7.27E-08	2.56E-07	4.50E-04	1.04E-07	1.59E-08	8.7	205	0.976
RB2	1.52E-06	9.787	296.1	7.00E-08	2.35E-07	4.55E-04	1.06E-07	1.64E-08	8.6	205	0.976
K1	1.20E-06	9.777	296.1	1.24E-07	2.32E-07	4.76E-04	1.16E-07	1.88E-08	6	210	0.975
error (STDEV cals):	1.79 %	0.26 %	0.12 %	1.01E-02	1.15E-02	5.68E-03	1.09E-02	2.05E-02			

Well	T	He	Ne	Ar	Kr	Xe	He	Ne	Ar	Kr	Xe
	K	ccSTP/g	ccSTP/g	ccSTP/g	ccSTP/g	ccSTP/g	%	%	%	%	%
FU1	277.75	4.75E-08	2.12E-07	4.32E-04	1.06E-07	1.59E-08	66.0%	22.5%	16.3%	11.9%	18.5%
RB1	281.85	4.66E-08	2.04E-07	3.91E-04	9.38E-08	1.37E-08	56.0%	25.7%	14.9%	10.7%	16.0%
RB2	281.75	4.66E-08	2.04E-07	3.92E-04	9.41E-08	1.38E-08	50.2%	14.9%	16.1%	13.2%	19.1%
K1	279.15	4.71E-08	2.09E-07	4.17E-04	1.02E-07	1.51E-08	162.5%	10.8%	14.2%	14.3%	24.5%
error (STDEV cals):											

Appendix F: Groundwater Flow Model

Well	z (obs)	z (sim)	GW depth	Residual	Comments
	m.a.s.l.	m.a.s.l.	m.b.s.	m	
RB1 , 2	205,00	201,35	18,05	6.58	lower aquifer
RB3	205,00	201,35	15,83	4.36	
TM1	193,87	206,18	12,04	-13.33	
TM2 , 3 , 4	196,20	207,15	15,98	-8.96	
TM5	194,00	206,40	12,88	-13,90	filter above modelled GW table
TM6 , 7 , 8	186,50	204,97	9,30	-17,60	filter above modelled GW table
TW2	173,70	196,46	2,70	-20.61	filter above modelled GW table
TW3	185,80	198,52	12,43	-12,10	filter above modelled GW table
TE1	177,00	192,10	6,98	-15.58	
GE1	206,39	203,69	23,47	11.34	lower aquifer
GE2	204,72	203,69	10,83	-1.28	
GE3	204,68	203,36	10,51	-2.77	
GE4 , 5	204,71	203,36	22,61	9.33	lower aquifer
BR29B	201,59	201,85	7,98	- 1.77	
G20	207,00	205,70	4,22	- 0.02	

Well	Res. Time y
RB1	26
RB2	20
RB3	14
K1	12
FU1	2,5
TM1	0,375
TM2	-
TM3	0,458
TM4	-
TM5	-
TM6	-
TM7	-
TM8	-
TW1	-
TW2	-
TW3	-
TE1	9
GE1	7
GE2	0,083
GE3	0,083
GE4	-
GE5	-
GW1	2
GW2	66
BAR-1	3
BAR-2	6
BAK-1	8
BAK-2	28
BAV-1	10
BAV-2	5